

Two-Particle Correlations in Heavy-Light Ion Collisions

Dissertation

Presented in Partial Fulfillment of the Requirements for the Degree
Doctor of Philosophy in the Graduate School of The Ohio State
University

By

Douglas Evan Wertepny, B.S.

Graduate Program in Physics

The Ohio State University

2016

Dissertation Committee:

Professor Yuri Kovchegov, Advisor

Professor Ulrich Heinz

Professor Michael Lisa

Professor Ciriya Jayaprakash

© Copyright by
Douglas Evan Wertepny
2016

Abstract

We studied the initial, high-energy scatterings in heavy ion collisions using the saturation/Color Glass Condensate framework, with a focus on two-particle long-range rapidity correlations. These two-particle correlations are modeled as two-gluon correlations, assuming that the kinetic information of the gluons survives the evolution of the system and presents itself in the final state particles. We calculate the two-gluon production cross section using the saturation framework in the heavy-light ion regime, where we consider all-order saturation effects in the heavy nucleus while considering only two-orders in saturation effects in the light ion.

The two-gluon production cross section produces four types of correlations: (i) geometric correlations, (ii) Hanbury Brown and Twiss (HBT) like correlations accompanied by a back-to-back maximum, (iii) near-side correlations, and (iv) away-side azimuthal correlations. All of these correlations are long-range in rapidity. The geometric correlations (i) are due to the fact that nucleons are correlated by simply being confined within the same nucleus and may lead to long-range rapidity correlations for the produced particles without strong azimuthal angle dependence. Long-range rapidity correlations (iii) and (iv) have exactly the same amplitudes along with azimuthal and rapidity shapes: one centered around $\Delta\phi = 0$ and the other one centered around $\Delta\phi = \pi$ (here $\Delta\phi$ is the azimuthal angle between the two produced gluons).

The geometry dependence of the correlation function (not to be confused with the geometric correlations) leads to stronger azimuthal near- and away-side correlations in the tip-on-tip U+U collisions than in the side-on-side U+U collisions, an exactly opposite behavior from the correlations generated by the elliptic flow of the quark-gluon plasma: a study of azimuthal correlations in the U+U collisions may thus help to disentangle the two sources of correlations. Finally we rewrite our result for the two-gluon production cross-section in a k_T -factorized form resulting in a factorized expression involving a convolution of one- and two-gluon Wigner distributions over both the transverse momenta and impact parameters. This differs from the normal k_T -factorized forms used in the literature and may have implications for the nature of k_T -factorization beyond the two-gluon production case.

To my loving family. I couldn't have done this without your support.

Acknowledgments

I would like to thank Professor Yuri Kovchegov for all of the hard work and time he has invested into my physics career. Starting from when I first took your Quantum Field Theory class I have always respected you as a physicist. I was thrilled when you took me on as one of your students and have since learned much from you. Without your guidance I do not know where I would be at this time. I would also like to thank all of the other professors at OSU whom I have learned much from.

I would like to thank all of the support staff in the physics department. You all work behind the scenes to make the entire department function. I would like to give a special thanks to Kris Dunlap for all of the help you have given me over the years. From switching research groups to dealing with other incidents you have been vital in helping me get through it all and for that I thank you.

I would also like to thank my family for all the support they have given me over the years. From the time I was born you have always been supportive of me and have pushed me to work hard. You have always been there to help in good times and bad and I love you all for it. Thanks for being there for me, I could not have done this without you.

This material is based upon work supported by the U.S. Department of Energy, Office of Science, Office of Nuclear Physics under Award Number DE-SC0004286.

Vita

May 2009B.S. in Physics and Music, The University of Dayton, Dayton, Ohio

Publications

Regularization of the Light-Cone Gauge Gluon Propagator Singularities Using Sub-Gauge Condition

G. A. Chirilli, Y. V. Kovchegov, and D. E. Wertepny, JHEP. **1512**, 138, (2015)

Classical Gluon Production Amplitude for Nucleus-Nucleus Collisions: First Saturation Correction in the Projectile

G. A. Chirilli, Y. V. Kovchegov, and D. E. Wertepny, JHEP. **1503**, 015 (2015)

Two-Gluon Correlations in Heavy-Light Ion Collisions: Energy and Geometry Dependence, IR Divergences, and k_T -Factorization

Y. V. Kovchegov and D. E. Wertepny, Nucl. Phys. A **925**, 254-295 (2014)

Fast Neutron Production from Lithium Converters and Laser Driven Protons

M. Storm, S. Jiang, D. E. Wertepny, et. al., Phys. Plasmas **20**, 053106 (2013)

Long-Range Rapidity Correlations in Heavy-Light Ion Collisions

Y. V. Kovchegov and D. E. Wertepny, Nucl. Phys. A **906**, 50-83 (2013)

Pressure broadening and shift of the cesium D1 transition by the noble gases and N₂, H₂, HD, D₂, CH₄, C₂H₆, CF₄ and ³He

G. A. Pitz, D. E. Wertepny, and G. P. Perram, Nucl. Phys. A **80**, 062718 (2009)

Fields of Study

Major Field: Physics

Table of Contents

	Page
Abstract	ii
Dedication	iv
Acknowledgments	v
Vita	vi
List of Figures	ix
List of Tables	xv
1. Introduction	1
1.1 Introduction to QCD	1
1.2 Heavy ion collisions	7
1.3 Saturation physics	10
1.4 Two-particle correlations	16
1.4.1 Experimental set-up	16
1.4.2 Experimental results and relation to the saturation framework	18
1.5 Goals and organization of thesis	22
2. Quantitative details of QCD, the heavy–light ion regime and it’s effect on the correlation function	25
2.1 Details of QCD	26
2.2 Heavy-light ion regime	28
2.3 Definition of the correlation function	37
2.3.1 Definition of the correlator	37
2.3.2 Geometric correlations	38
2.4 Summary	41

3.	Review of single-gluon production	43
3.1	Target nucleus as a shock wave	43
3.2	Single-gluon production cross section	51
3.3	Gluon dipole amplitude	57
3.4	k_T -factorization for single-gluon production	64
3.5	Summary	67
4.	Calculation of the two-gluon correlation function	69
4.1	Two-gluon production cross section	69
4.1.1	Amplitudes of the two-gluon production process	70
4.1.2	Two-gluon production with long-range rapidity correlations: “square” of the single gluon production	75
4.1.3	Two-gluon production with long-range rapidity correlations: “crossed” diagrams	78
4.1.4	Two-gluon production with long-range rapidity correlations: the net result	84
4.2	Long-range rapidity correlations: away-side and near-side; HBT correlations	84
4.3	Summary	102
5.	Geometric effects and k_T -factorization	104
5.1	Geometry-dependent correlations	104
5.2	k_T -factorization	108
5.2.1	One- and two-gluon distribution functions	110
5.2.2	Derivation of the factorized forms	117
5.3	Summary	125
6.	Conclusions	127
	Bibliography	130
	Appendices	
A.	Double-trace operator	139

List of Figures

Figure	Page
1.1 Plot of the running of the strong coupling constant α_s . Taken from [1].	6
1.2 Evolution of the collision of two heavy ions, explained in detail below. Adapted from [2].	8
1.3 Diagrammatic representation of the DIS process, $e + p \rightarrow e + X$. The incoming electron emits a photon (momentum q) which interacts with the incoming proton (momentum p). This process breaks up the proton producing many particles which are represented by X	10
1.4 HERA results showing the parton distributions, multiplied by x_B , at fixed $Q^2 = 10 \text{ GeV}^2$ ($\mu_f^2 = Q^2$) as a function of x_B . The gluon distribution dominates at small- x . Taken from [3].	12
1.5 The evolution of the gluon density is governed by the interplay of two effects, gluon splitting (shown on the left) and gluon recombination (shown on the right). The gluon splitting increases the density while the recombination reduces the density.	14
1.6 Due to the Lorentz contraction of the heavy ion any particle passing through it sees the entire nucleus. Everytime the particle interacts it sees the nuclear profile function which scales as $T(\mathbf{b}) \sim A^{\frac{1}{3}}$. This gives rise an $A^{\frac{1}{3}}$ for every interaction with the heavy ion.	15

- 1.7 Left: The side view of the detector illustrates the two ion beams traveling in opposite directions along the beam axis. At the center they collide and produce particles. The kinetic trajectories of two particles are shown in red (particle 1) and blue (particle 2). By measuring the angle that the trajectory of particle 1 makes with the beam axis, θ_1 , one determines the pseudo rapidity of the particle. By subtracting the pseudo rapidity of the two particles one arrives at $\Delta\eta$, one of the variables of interest. Right: Looking down the beam pipe at the transverse plane, the two particles with transverse momenta \mathbf{k}_1 and \mathbf{k}_2 have an azimuthal angle between them, $\Delta\phi$ 16
- 1.8 Left: Data for two particle correlations in p-Pb collisions at $\sqrt{s_{NN}} = 5.02 \text{ TeV}$. There are two long range in rapidity “ridges” at $\Delta\phi = 0$ and $\Delta\phi = \pi$. The peak at $\Delta\phi = 0$ and $\Delta\eta = 0$ is due to jet fragmentation. Right: Data of the ridge averaged over $0.8 < |\Delta\eta| < 1.8$ on the near-side which removes the central peak and $|\Delta\eta| < 1.8$ on the away-side. Fits containing a $\cos(2\Delta\phi)$ term (dashed black line) and both a $\cos(2\Delta\phi)$ and $\cos(3\Delta\phi)$ (solid red line) term are superimposed. Both graphs are from the ALICE collaboration and were taken from [4]. 19
- 1.9 A diagrammatic representation of the causality argument. The two particles with momenta k_1 (red) and k_2 (blue) have a large difference in rapidity and thus point in different directions inside the light cone. The two particles must originate at the same common causal part, represented by the shaded purple region. 20
- 2.1 Transverse plane geometry of the two-particle production in the collision of a smaller projectile nucleus (A_1) with a larger target nucleus (A_2). The two smaller circles represent two nucleons in the nucleus A_1 (see text for details). 29
- 2.2 A sample Feynman diagram for each of the single-gluon production processes considered. The diagrams show a single gluon being produced by a collision of one- or two-nucleons with the target nucleus (left and right diagram respectively). The dashed line represents the interaction with the target (also known as the shock wave) which takes into account all of the multiple rescatterings with the target nucleons. 30

2.3	A sample Feynman diagram for each of the two-gluon production processes is considered. The diagrams show two gluon being produced by a collision of one- or two-nucleons with the target nucleus (left and right diagram respectively). The dashed line represents the interaction with the target (also known as the shock wave).	31
2.4	A quark or a gluon (black arrow) passes through the target (grey oval) and interacts with the many fields (dashed lines) originating from the color sources (red, green and blue ovals). The kinematics of the interaction are such that it does not change the trajectory of the particle much allowing us to treat the interaction with the target as a shock wave. This is described in more detail in Sec. 3.1.	33
3.1	The Feynman diagram associated with the classical gluon field emitted by a target nucleon, $A_{MV,\mu}^a$. The nucleon is represented by a massless, eikonal valence quark traveling in the x^- direction. Due to the fact that the outgoing and incoming quark lines are on mass-shell the outgoing quark has $b^- = \infty$	44
3.2	Feynman diagram representing a projectile quark interacting with the classical gluon fields emitted from nucleons 1 and 2. The external lines of the projectile quark are dropped in the calculation.	48
3.3	Feynman rules associated with quarks and gluons passing through a shockwave induced by the target nucleus. The shockwave is denoted by a red box.	50
3.4	Single-gluon production amplitudes. The dashed line represents the shock wave due to the interaction with the target.	51
3.5	An eikonal quark originating from the projectile emits a gluon before passing through the shock wave. The shock wave is a red box to emphasize that the shock wave has some finite thickness.	52
3.6	Diagrams contributing to the square of the scattering amplitude for the single gluon production in pA collisions. The cross denotes the measured produced gluon.	55

3.7	Graphical representation of the gluon dipole S-Matrix, $S_G(\mathbf{x}, \mathbf{y})$. The gray ovals represent different target nucleons and the dotted lines are the exchanged gluons. These gluon can either interact with the top or bottom Wilson line.	58
3.8	A finite section of the Wilson line object. The nucleon emits two gluon fields which interact with the two Wilson lines in all possible ways.	59
3.9	Left: Plot of the forward scattering amplitude, $N_G(\mathbf{x}, \mathbf{y})$, of the gluon dipole where $r_\perp = \mathbf{x} - \mathbf{y} $ is the transverse size of the dipole. To plot this we neglected dependence of the function on the nuclear profile function and the log dependence. Right: A pictorial representation of the physical picture. The smaller the dipole the less charge it sees so the nucleus is more transparent. The larger the dipole is the more charge it sees and the more opaque the target becomes. This continues until the dipole sees so much charge that the charges start to screen one another.	63
4.1	B diagrams. These are the diagrams associated with the gluon emission process where two gluons are emitted from different nucleons in the amplitude. The shock wave is represented by a dashed line.	70
4.2	C diagrams. One of the nucleons in the projectile emits both of the observed gluons. Once again the shock wave is represented by a dashed line.	71
4.3	Diagrams C_1 and C_2 . The difference between the two diagrams is the ordering of gluon emissions that happen before the shock wave, represented by a dashed line. The sum of these two diagrams combine into a compact result.	72
4.4	Diagrams contributing to the two-gluon production cross section in the heavy–light ion collision. For clarity the diagrams are shown as a direct product of gluon production processes in collisions of the two interacting nucleons from the projectile nucleus with the target nucleus.	76
4.5	Diagrams contributing to the two-gluon production cross section, with the gluon emitted by each nucleon in the amplitude absorbed by another nucleon in the complex conjugate amplitude. The top cross denotes the gluon with momentum \mathbf{k}_1 , while the bottom one denotes the gluon with momentum \mathbf{k}_2	79

4.6	Another set of diagrams contributing to the two-gluon production cross section, with the gluon emitted by each nucleon in the amplitude absorbed by another nucleon in the complex conjugate amplitude. Again the top cross denotes the gluon with momentum \mathbf{k}_1 , while the bottom one denotes the gluon with momentum \mathbf{k}_2	80
4.7	The flow of the “plus” momentum component through the first diagram in Fig. 4.5.	81
4.8	Examples of diagrams generating contributions to 4.29: the left panel represent the away-side correlations (the first term in 4.29), while the right panel contributes near-side correlations (the second term in 4.29). The t -channel gluon momenta flow toward the triple-gluon vertices to the left of the cut, and away from those vertices to the right of the cut.	89
4.9	An example of a diagram giving a contribution to the first term in the curly brackets of 4.38.	93
4.10	A toy azimuthal two-gluon correlation function motivated by the calculation in this section. Vertical scale is arbitrary.	98
4.11	An example of a lowest-order diagram generating HBT-type correlations.	101
5.1	The layout of two possible geometries for the $U + U$ collisions. The top panel is the tip-on-tip collision, which has the z -axis of the two nuclei anti-parallel to each other and (anti-)parallel to the collision axis. The bottom diagram is the side-on collision, which has the z -axis of the two nuclei parallel to each other and perpendicular to the collision axis. .	107
5.2	The top panel represents the forward amplitude for the scattering of two gluon dipoles on a target nucleus in the quasi-classical approximation: this is an essential contribution to the definition of the two-gluon distribution in 5.7. The bottom panel represents the quadrupole scattering on the target, as in the definition of the two-gluon distribution in 5.9. The vectors \mathbf{x} , \mathbf{y} , \mathbf{z} , and \mathbf{w} label the positions of the gluon Wilson lines. Vertical solid lines denote the initial (left) and final (right) states. The final state of the gluons is labeled to stress that the difference between the two panels is in the color configurations of the final state.	113

- A.1 Diagrams contributing to the correlator in [A.1](#) in the quasi-classical approximation. Vertical dashed lines denote t -channel gluons, while the shaded ovals represent the nucleons in the target nucleus. [139](#)
- A.2 The diagrammatic representation of the matrix element associated with a nucleon interacting with 4 adjoint Wilson lines, $\hat{M}^{a'a,b'b,c'c,d'd}(\mathbf{x}_1, \mathbf{x}_2, \mathbf{x}_3, \mathbf{x}_4)$. The dotted line represents the gluon fields and it interacts in all possible ways with the Wilson lines. . . . [142](#)

List of Tables

Table	Page
1.1 Comparing various properties of QED and QCD. Adapted from [5].	4

Chapter 1: Introduction

This dissertation is based on and borrows heavily from the work done by the author in [6, 7].

1.1 Introduction to QCD

This section closely follows the pedagogical outline found in [5].

Quantum Chromodynamics (QCD) is the quantum theory that governs the behavior of the strong force [8–13]. Before getting into the details of QCD it is helpful to examine the theory of Quantum Electrodynamics (QED), the quantum mechanical extension of classical electrodynamics (for more on classical electrodynamics see [14]). Despite the fact that the physics of QCD is very different from the physics of QED there are many similarities between the two theories.

QED is an abelian U(1) gauge theory and consists of two types of fundamental particles, photons and charged leptons. The charged leptons are massive spin- $\frac{1}{2}$ particles (fermions). There are three types of charged leptons: electrons (e^-), muons (μ^-) and tau leptons (τ^-), each of which has a corresponding antiparticle (e^+ , μ^+ , τ^+) that has the same mass and spin but opposite charge. Each of these are part of a different family and the mass of each particle is larger than the preceding one, τ being the heaviest ($1.78 \frac{GeV}{c^2}$ [1]) and e being the lightest ($0.511 \frac{MeV}{c^2}$ [1]). These

particles each have electric charge $-e$ (the antiparticles have charge $+e$) and couple to electromagnetic fields which, when quantized, are photons (γ).

Photons are spin-1 massless particles (bosons) and are vector fields notated by A_μ . These are the gauge fields of QED and also known as the carriers of the electromagnetic force. It is important to note that photons do not carry charge which means that photons cannot directly interact with each other, they can only interact through an intermediating particle, charged leptons in this case. The coupling constant associated with QED is $\alpha_{EM} = \frac{e^2}{4\pi\hbar c}$ and is fairly weak, on the order of $\mathcal{O}(10^{-2})$. It should be noted that α_{EM} , due to the quantum mechanical nature of the theory, changes as a function of energy or momentum scale. This property is known as the running of the coupling. In QED the running isn't very strong: α_{EM} increases with energy and, in experimentally relevant situations, it always remains small.

QCD follows a similar pattern with a few important distinctions. It is a non-abelian SU(3) gauge theory that contains of two types of fundamental particles, quarks and gluons. There are 6 different types of quarks (known as flavors), each of which are massive spin- $\frac{1}{2}$ particles (fermions). There are 3 families each consisting of two different quarks (each of which have their own anti-particles); up and down (u, d), charm and strange (c, s), and top and bottom (t, b). Each family is heavier than the preceding family with t being the heaviest ($170 \frac{GeV}{c^2}$ from direct measurements [1]) and u being the lightest ($2.3 \frac{MeV}{c^2}$ [1]). Quarks carry color charge, which has charge constant g , and couple to the color fields known as gluons. What makes color charge different from electric charge is that there are three different types of color charge (also known simply as colors) red, blue and green (r, g, b) each of which has a corresponding anti-charge ($\bar{r}, \bar{g}, \bar{b}$). This is in contrast to QED which has only a single

type, the electric charge. Quarks carry electric charge as well but this is unimportant for the current discussion, due to the fact that here we are focusing on the differences between QED and QCD.

Gluons are spin-1 massless particles (bosons) and make up the gauge field of the theory. They are vector fields notated by A_μ^a , where a refers to the color charge of the gluon. Gluons, unlike quarks, have 8 possible color charges. These can be thought of as a linear superposition of the color and anti-color charges quarks carry (for example a gluon can have the following combination: $\frac{r\bar{b}+b\bar{r}}{\sqrt{2}}$). One can also think of the different color charges the quarks and gluons carry as the fundamental and the adjoint representations of SU(3) color group respectively. Since gluons carry charge they can directly interact with one another. This makes the physical implications of QCD drastically different than QED. One important consequence of this is the strong coupling constant, defined as $\alpha_s = \frac{g^2}{4\pi\hbar c}$, runs significantly as a function of energy and momentum (and therefore distance scales) and decreases with energy. Depending on the energy scale the coupling constant can be on the order of anywhere from $\mathcal{O}(1)$ to $\mathcal{O}(10^{-1})$. A summary of the similarities and differences between QED and QCD is shown in Table 1.1.

Since the coupling constant in QED is always small at all experimentally probed energies, $\alpha_{EM} \sim \mathcal{O}(10^{-2})$, it is relatively simple to work with quantitatively. The coupling constant, α_{EM} , is small enough that it is possible to do calculations by perturbatively expanding around a free-field theory where photons and charged leptons decouple. The potential between two stationary oppositely charged leptons (take an electron and positron) to lowest order in α_{EM} is the well known attractive Coulomb potential, $\propto -\frac{1}{r}$, where r is the distance between the two particles. With higher order

	QED	QCD
Gauge Group	Abelian U(1)	Non-Abelian SU(3)
Charged Fermions	Charged Leptons e, μ, τ	Quarks u, d, c, s, t, b
Gauge Bosons	Photons, γ A_μ	Gluons, g A_μ^a
Type of Charge	Electric e	Color r, b, g
Coupling Constant	$\alpha_{EM} = \frac{e^2}{4\pi\hbar c}$ $\mathcal{O}(10^{-2})$	$\alpha_s = \frac{g^2}{4\pi\hbar c}$ $\mathcal{O}(1) \text{ to } \mathcal{O}(10^{-1})$

Table 1.1: Comparing various properties of QED and QCD. Adapted from [5].

corrections in α_{EM} (known as quantum corrections), one eventually starts to see a screening behavior due to electron and positron pairs (heavier charged lepton pairs also contribute) popping in and out of the vacuum at small distances. These quantum corrections do not strongly affect the behavior at large distances. Due to this $\frac{1}{r}$ behavior at large distances, if one pulls the particles far enough apart the potential approaches zero and allows for the existence of free particles.

In QCD the situation is a bit more complicated. The coupling constant α_s varies considerably as a function of the distance between the particles. It turns out at small distances (large energies) the strong coupling constant is small, $\alpha_s \sim \mathcal{O}(10^{-1})$, which allows for a perturbative approach to calculations, similar to QED. In this regime the potential between two oppositely charged quarks, say for example r and \bar{r} , follows the same behavior as in QED, $\propto -\frac{1}{r}$ [5]. This means at large energies (short distances) the quarks are bound together only by the Coulomb-like potential, and, therefore, can

be treated as weakly interacting particles. This phenomenon is known as asymptotic freedom.

At larger distances (lower energies) the strong coupling constant becomes large, $\alpha_s \sim \mathcal{O}(1)$. Perturbative calculations are impossible since α_s is no longer a valid expansion parameter. In this regime in order to get quantitative results, one has to use other techniques, the most common being Lattice calculations. Numerical calculations have shown that at large distances the potential between two quarks increases linearly with distance, $V(r) = \kappa r$ where $\kappa \sim 1 \frac{\text{GeV}}{\text{fm}}$ and is known as the string tension [1]. This property, known as confinement, prevents the existence of free quarks due to the fact that when two quarks are pulled far enough apart the potential energy becomes so great that it creates a new pair of quarks. The running of the strong coupling constant gives rise to an intrinsic energy scale associated with QCD, known as $\Lambda_{QCD} \approx 250 \text{ MeV}$ [15], which can roughly be thought of as the energy scale at which process switch from the perturbative to the non-perturbative regime. A plot of the running of the strong coupling constant is shown in Fig. 1.1.

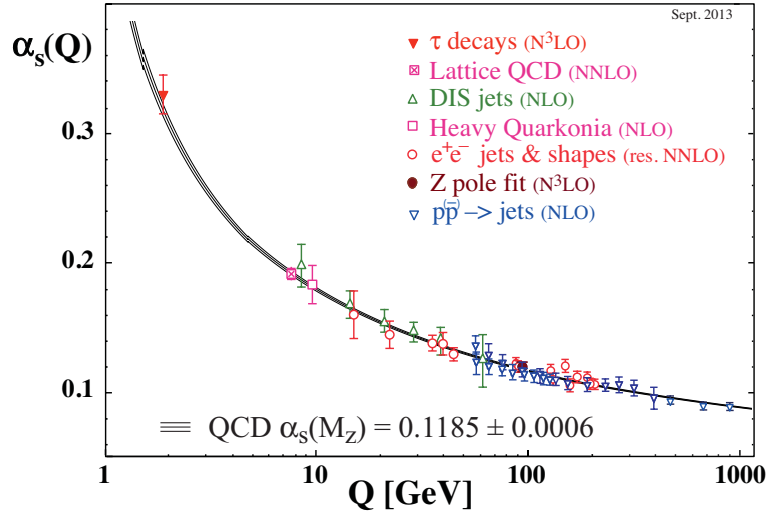


Figure 1.1: Plot of the running of the strong coupling constant α_s . Taken from [1].

The lack of free quarks in nature means that we only see bound quarks. These bound states come in two main types, mesons consisting of a quark and an anti-quark (e.g. mesons) and baryons consisting of three quarks or three anti-quarks (e.g. protons). The different bound states have different masses which, due to the non-perturbative nature of QCD in this regime, are hard to calculate from first principles. In fact, calculating the mass spectrum of this zoo of particles from first principles is one of the outstanding problems of QCD.

There are many other aspects of QCD which are currently unknown despite the fact that the Lagrangian governing the theory has been known for decades (for many examples see [16]). One such uncertain regime is the limit of high temperature. What makes this regime interesting is, that not only are the quarks and gluons unbound, there are a large number of them in a compact volume. The large density of color charges combined with the small coupling creates a situation where there is color

screening, meaning that particles far away from each other no longer experience a force between them. This is known as a quark-gluon plasma (QGP) and its properties have important implications for the nature of QCD.

One of the places QGP is thought to exist are heavy ion collisions. In heavy-ion collisions, two ions hit each other at such high energies that a high temperature QCD medium is created which allows for a QGP to exist at its core. By analyzing these interactions we can learn more about how QCD behaves in a medium at finite temperature. Another interesting regime that heavy ion collisions probe is the high energy regime. At the very beginning of the interaction we have a high-energy scattering problem between the constituents of the ions, adding another fascinating dynamic to the phenomenon.

1.2 Heavy ion collisions

One of the main complications of using heavy-ion collisions to study the QGP is the incredibly complex nature of these systems. There are a wide variety of processes that occur in a single event, each of which probes a different regime of QCD and involves different physics, requiring different computational techniques to understand. Here we divide up the system into 5 distinct phases; initial interactions, pre-equilibrium, hydrodynamics, hadron gas and kinetic freeze-out. A general overview is presented below and shown diagrammatically in Fig. 1.2.

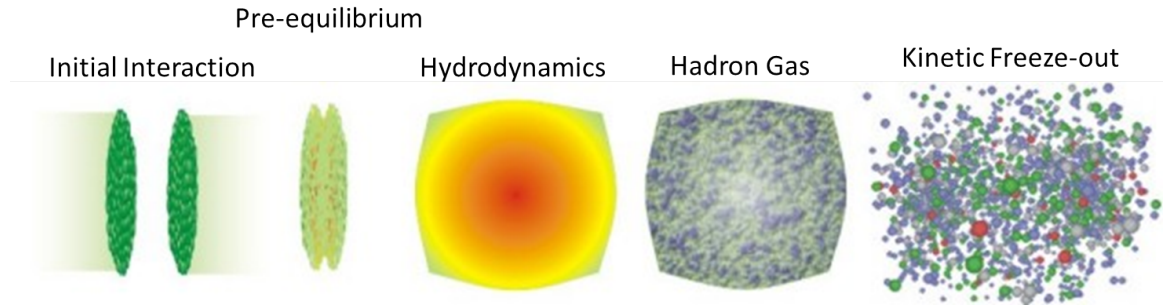


Figure 1.2: Evolution of the collision of two heavy ions, explained in detail below. Adapted from [2].

I: Initial interactions

We have two heavy ions, each of which has an initial distribution of quarks and gluons. These two ions collide with each other at high energies, they are heavily Lorentz contracted, and their intrinsic dynamics is time dilated. Lorentz contraction results in the ions appearing as two flat pancakes. Time dialation slows down the internal fluctuations of the quarks and gluons inside, causing the distribution to appear frozen in place. The end result is that we have a high-energy scattering problem between two fixed distributions of quarks and gluons which can be described within the saturation/Color Glass Condensate (CGC) formalism, outlined in Sec. 1.3. In this formalism, the gluon fields end up driving the evolution of the system.

II: Pre-equilibrium

After the initial interaction, the system continues to evolve as what is known as a “Glasma,” a distribution of gluons in the CGC formalism. During this phase the system begins to approach a local equilibrium distribution. This happens through a process known as thermalization which is currently a subject of great interest among theorists as there is currently no universally accepted explanation for how it occurs.

At some point, these fields are close enough to thermal equilibrium that they can be described by dissipative fluid dynamics.

III: Hydrodynamics

The onset of the applicability of fluid dynamics, due to the fact that it requires the system to be in approximate thermal equilibrium, combined with the large density of quarks and gluons at a high temperature means the system is now a QGP. The system, at this point, is modeled with various hydrodynamical codes, a review of which is found in [17]. This hydrodynamical evolution of the system causes the fluid to expand and cool down.

IV: Hadron gas and V: Kinetic freeze-out

Eventually, the system will cool down enough so that individual quarks and gluons are no longer free and form bound states (hadrons). This process is known as hadronization. From there on these hadrons continue to interact with each other in what is known as a hadron gas until kinetic freeze-out, the point where the hadrons no longer interact, and thus free stream into the detector.

While the hydrodynamic flow (and thermalization to some extent) actually involves the QGP, knowing the physics of all of these different processes is vital in order to understand the data. Without an accurate description of the physics of all of these regions, it is impossible to accurately reconstruct the collisions from the data. Understanding the initial interactions is vital for understanding how heavy-ion collisions work, especially since it is from these initial conditions that the rest of the system evolves. To model these initial interactions we use, as previously mentioned, the saturation framework.

1.3 Saturation physics

The brief review of saturation physics presented here is based on the review presented in [18]. For more detailed reviews see [19–23].

As we know, the way QCD behaves varies depending on the distance scale. We normally think of a proton as purely consisting of its three valence quarks (uud). However, it turns out that this picture is too simple. As on probes smaller distance scales, the particles making up the nucleon become increasingly more complicated. One starts to see that the proton is composed of, in addition to valence quarks, quark and anti-quark pairs, known as sea quarks, as well as gluons, all of which are commonly referred to as partons. This phenomenon is important when considering high energy interactions in QCD, which probe such short distance scales. Here we focus on one particular process, deep-inelastic scattering (DIS).

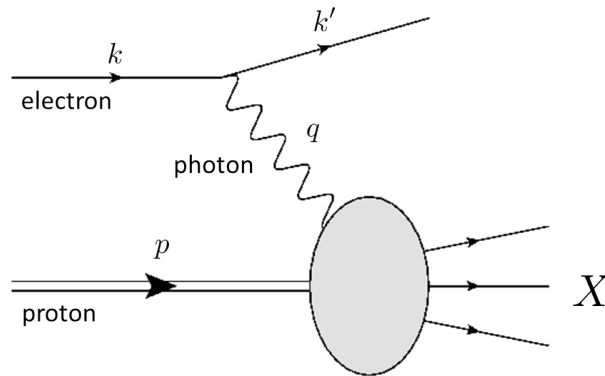


Figure 1.3: Diagrammatic representation of the DIS process, $e + p \rightarrow e + X$. The incoming electron emits a photon (momentum q) which interacts with the incoming proton (momentum p). This process breaks up the proton producing many particles which are represented by X .

In DIS, an electron with momentum k scatters off a proton with momentum p . The scattering process is mediated by a single virtual photon with momentum q , which is emitted by the electron and interacts with the proton. The interaction with the proton breaks it up producing a multitude of particles which we denote as X , the exact composition of which is not important for the physics at hand. A diagram of this process is shown in Fig. 1.3.

Depending on the kinematics of the collision, the way the photon observes the target proton changes. The composition of the proton is described by a parton distribution functions, which describes the number density of a given parton inside the proton. It turns out, these can be described with only a few variables associated with the kinematics of the collisions. First off we have the virtuality of the photon $Q^2 = -q^2$. Secondly we have what is known as Bjorken- x , $x_B = \frac{Q^2}{2p \cdot q}$ (this is often denoted in the literature as just x), which, as we can see, is related to Q^2 and the center of mass energy squared of the collision between the photon and the proton ($s = (p + q)^2 \approx 2p \cdot q - Q^2$ if we neglect the mass of the proton).

The parton distribution function, given by $f(x, Q^2)$, gives the number density of partons at a particular x_B and Q^2 . The parton distribution can be found experimentally.

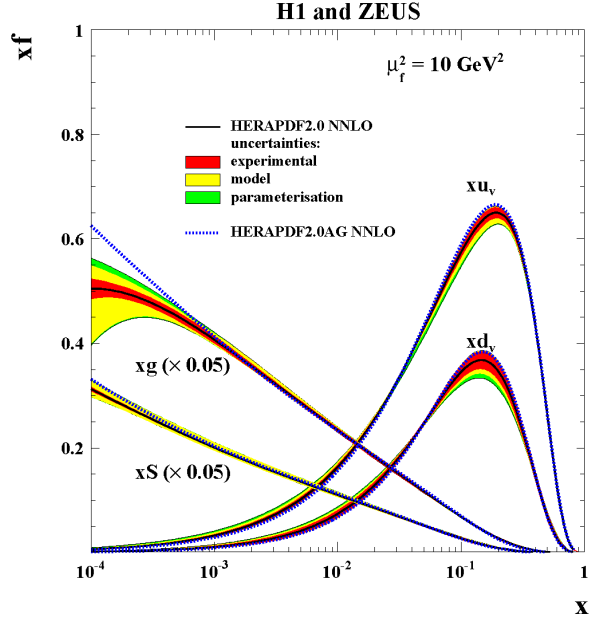


Figure 1.4: HERA results showing the parton distributions, multiplied by x_B , at fixed $Q^2 = 10 \text{ GeV}^2$ ($\mu_f^2 = Q^2$) as a function of x_B . The gluon distribution dominates at small- x . Taken from [3].

An experimental determination of the parton distributions for a proton using data from the HERA experiment is shown in Fig. 1.4. Here Q^2 is fixed at 10 GeV^2 while x_B (notated by x in the figure) varies. Each type of parton distribution is notated differently: $g(x, Q^2)$ for gluons, $S(x, Q^2)$ for the sea quarks, $u_v(x, Q^2)$ for the valence up quarks and $d_v(x, Q^2)$ for the valence down quarks. In the plot all of them are multiplied by x_B while the gluon and sea quark distribution are further multiplied by 0.05 so that they fit on the same plot.

As one can see in the small- x regime, $x_B \ll 1$, the gluon probability density is large and thus interactions with gluons dominate scattering processes. This dense distribution of gluons in the small- x regime is known as the color-glass condensate (CGC). To describe the change in the gluon distribution at a given Q^2 and initial

value x_B one uses various evolution equations, either evolving in x_B while keeping Q^2 fixed or vice-versa.

The most fundamental evolution equation for evolution in x_B at fixed Q^2 is the Balisky-Fadin-Kuraev-Lipatov (BFKL) equation [24,25]. This equation has the physical interpretation that as x_B decreases in value the probability that a gluon in the parton distribution splits into two gluons increases. It is a linear equation because this splitting process only requires one gluon. This equation results in the gluon density having power-law dependence on x_B .

This is not the whole story, when the density of gluons becomes large enough another effect becomes important, gluon recombination, when two gluons merge into a single gluon. In order to take this into account we need to use equations that consider this non-linear effect. The equations that do this are the Balitsky-Kovchegov (BK) [26–29] and Jalilian-Marian-Iancu-McLerran-Weigert-Leonidov-Kovner (JIMWLK) [30–33] evolution equations. The small-x evolution of the gluon density is governed by these two effects, gluon splitting which increases the density and gluon recombination which reduces the density. These effects are shown in Fig 1.6. The point at which gluon recombination becomes important gives rise to what is known as the saturation scale, Q_s .



Figure 1.5: The evolution of the gluon density is governed by the interplay of two effects, gluon splitting (shown on the left) and gluon recombination (shown on the right). The gluon splitting increases the density while the recombination reduces the density.

Saturation is not just limited to protons but it happens with heavy ions as well although the situation is slightly different. Heavy ions, being bound states of protons and neutrons, have a large number of nucleons in them. The large number of nucleons in the heavy ion gives rise to an enhancement to the number of gluons in the heavy ion. Due to the high occupation number of the gluons the physics is classical. Modeling heavy ions in this way, with classical gluon fields, is known as the McLerran-Venugopalan (MV) model [34–36].

To leading order in A , the atomic number of nucleus, the nucleons are independent of each other. In other words the distributions of nucleons in this limit is purely a number density function, $\rho(\vec{r})$, where the probability of finding a nucleon in a given location is independent of the others.

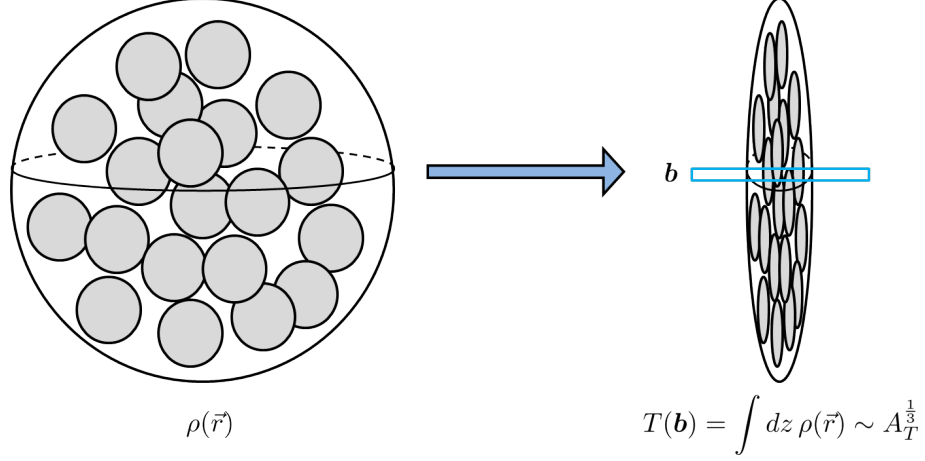


Figure 1.6: Due to the Lorentz contraction of the heavy ion any particle passing through it sees the entire nucleus. Everytime the particle interacts it sees the nuclear profile function which scales as $T(\mathbf{b}) \sim A^{\frac{1}{3}}$. This gives rise an $A^{\frac{1}{3}}$ for every interaction with the heavy ion.

Heavy ion collisions are initially high energy scattering events, meaning that the ions are heavily Lorentz contracted. When a particle passes through a heavy ion it roughly sees a flat pancake, so when an incoming particle interacts with nucleons in the heavy ion it probes the entire nuclear profile function (the nuclear profile function is defined as $T(\mathbf{b}) = \int dz \rho(\vec{r})$). Since the radius of a nucleus scales as $R \sim A^{\frac{1}{3}}$ the nuclear profile function scales as $T(\mathbf{b}) \sim A^{\frac{1}{3}}$ and leads to the $\sim A^{\frac{1}{3}}$ enhancement of the gluon density in the heavy ion. The saturation scale also gets enhanced, $Q_s^2 \sim A^{\frac{1}{3}}$, such that saturation effects are stronger in heavy ions than in a proton. For instance for a gold ion at the relativistic heavy ion collider (RHIC) at $\sqrt{s_{NN}} = 200 \text{ GeV}$ the saturation scale is $Q_s^2 \approx 2 \text{ GeV}^2$ while for a proton at the same energy it is $Q_s^2 \approx .3 \text{ GeV}^2$. This results in a large occupation number of gluons, justifying the

classical description of the MV model. Thus we can model the initial high energy scatterings of heavy ion collisions using the saturation framework.

1.4 Two-particle correlations

In this work we will be focusing on describing the initial conditions of heavy-ion collisions within the saturation framework. In particular, we will be looking at the effects of the initial conditions on two-particle correlations. Before doing this, it is helpful to look at the general kinematics of the experimental set-up to get an idea of exactly what the experimental data are telling us.

1.4.1 Experimental set-up

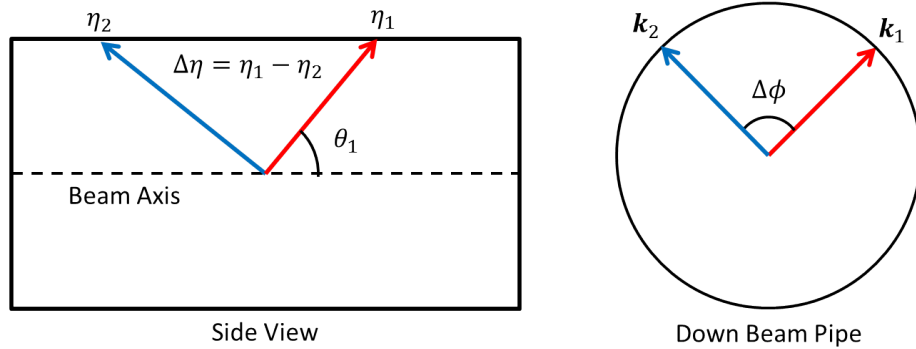


Figure 1.7: Left: The side view of the detector illustrates the two ion beams traveling in opposite directions along the beam axis. At the center they collide and produce particles. The kinetic trajectories of two particles are shown in red (particle 1) and blue (particle 2). By measuring the angle that the trajectory of particle 1 makes with the beam axis, θ_1 , one determines the pseudo rapidity of the particle. By subtracting the pseudo rapidity of the two particles one arrives at $\Delta\eta$, one of the variables of interest. Right: Looking down the beam pipe at the transverse plane, the two particles with transverse momenta \mathbf{k}_1 and \mathbf{k}_2 have an azimuthal angle between them, $\Delta\phi$.

Fig. 1.7 shows the basic set up: we have the two ions traveling along the beam axis, \hat{z} , also called the longitudinal direction which we notate as x_3 , in opposite directions. Perpendicular to the beam axis we have the transverse coordinates. It is convenient from an experimental point of view to introduce a new variable, pseudo rapidity, represented by η . For a particle with 3-momentum \vec{k} it is defined as,

$$\eta = \frac{1}{2} \ln \left(\frac{|\vec{k}| + k_3}{|\vec{k}| - k_3} \right).$$

It can be related to the angle between the particle's trajectory and the beam pipe axis, θ by

$$\eta_1 = -\ln \left(\tan \frac{\theta_1}{2} \right).$$

The experiments can easily find the pseudo rapidity of the particle. Often the results are reported in terms of pseudo rapidity.

While experimental data may be reported in terms of pseudo rapidity the more useful quantity from a theoretical stand point is known as rapidity. Rapidity, represented by y , is defined as

$$y = \frac{1}{2} \ln \left(\frac{E + k_3}{E - k_3} \right).$$

In the limit we are dealing with the particles have a much higher energy than their rest mass. So we can neglect the mass term when calculating the energy of the problem, $E = \sqrt{m^2 + |\vec{k}|^2} \approx |\vec{k}|$. The pseudo rapidity in the limit becomes equal to the rapidity,

$$\eta \approx \frac{1}{2} \ln \left(\frac{E + k_3}{E - k_3} \right) = y.$$

Thus when doing theoretical calculations we will consider the rapidity, y , and not the pseudo rapidity, η .

1.4.2 Experimental results and relation to the saturation framework

We are focusing on long-range rapidity correlations between pairs of hadrons that are produced at small azimuthal angles with respect to each other. These correlations were discovered in heavy ion (AA) [37–40], proton–proton (pp) [41], and proton–nucleus (pA) collisions [42]. Due to the particular shape of the corresponding correlation function, with a narrow correlation in the azimuthal angle $\Delta\phi$ and a wide correlation in pseudo-rapidity separation $\Delta\eta$, these correlations are often referred to as the “ridge”.

Fig. 1.8 shows more recent experimental results from the ALICE collaboration for p–Pb collisions, [4]. We can see that there are two “ridges” in the results, one on the near-side ($\Delta\phi = 0$) and one on the away-side ($\Delta\phi = \pi$). These “ridges” are mostly symmetric except for a small deficit on the away-side, leading to a correlation dominated by even harmonics.

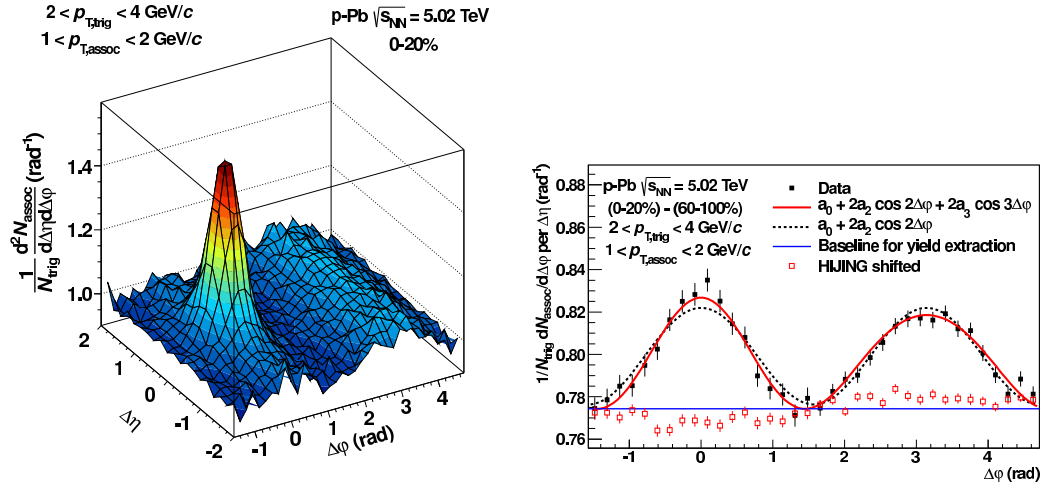


Figure 1.8: Left: Data for two particle correlations in p–Pb collisions at $\sqrt{s_{NN}} = 5.02 \text{ TeV}$. There are two long range in rapidity “ridges” at at both $\Delta\phi = 0$ and $\Delta\phi = \pi$. The peak at $\Delta\phi = 0$ and $\Delta\eta = 0$ is due to jet fragmentation. Right: Data of the ridge averaged over $0.8 < |\Delta\eta| < 1.8$ on the near-side which removes the central peak and $|\Delta\eta| < 1.8$ on the away-side. Fits containing a $\cos(2\Delta\phi)$ term (dashed black line) and both a $\cos(2\Delta\phi)$ and $\cos(3\Delta\phi)$ (solid red line) term are superimposed. Both graphs are from the ALICE collaboration and were taken from [4].

Since these correlated involve particles that are far apart in rapidity they must originate from the early-time dynamics. The logic goes as follows: But since they are far apart in rapidity they are pointing in different directions inside the light cone, one close to x^+ axis the other close to the x^- axis. Due to causality, any correlation between these two particles must originate in the intersection of their past light-cones, known as their common causal past. This would place the origin towards the beginning of the interaction, in the initial state [43, 44]. This is shown in figure 1.9. Despite knowing that these correlations originate from the initial interactions, the detailed dynamical origin of these correlations is not completely clear.

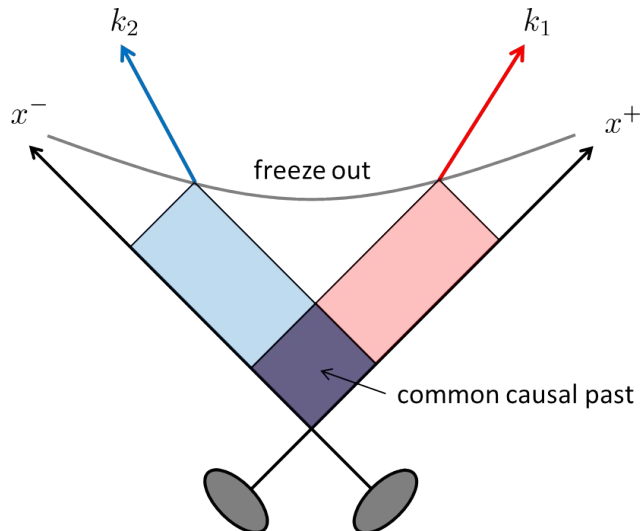


Figure 1.9: A diagrammatic representation of the causality argument. The two particles with momenta k_1 (red) and k_2 (blue) have a large difference in rapidity and thus point in different directions inside the light cone. The two particles must originate at the same common causal part, represented by the shaded purple region.

It has been proposed in the literature [43–51] that these “ridge” correlations may arise in the classical gluon field dynamics of the parton saturation physics/CGC. Indeed classical gluon fields, which in the MV model dominate gluon production in heavy ion collisions, do lead to a rapidity-independent distribution of the produced gluons [52–55] over rapidity intervals of up to $\Delta y \lesssim 1/\alpha_s$, which is the upper limit of their validity (with α_s the strong coupling constant). Correlations between such classical fields, introduced in the process of averaging over their color sources, do have a long range in rapidity [43, 44, 56]. Moreover, it was observed in [43, 47–49] that the diagrams giving rise to such rapidity correlations also lead to a narrow correlation in the azimuthal direction, in qualitative agreement with the shape of the “ridge” correlation.

A potential complication with the CGC explanation of the “ridge” is the fact that rapidity-dependent corrections of classical gluon fields do become important once rapidity is on the order of $\Delta y \sim 1/\alpha_s$. These corrections come in through the non-linear BK and JIMWLK evolution equations. Rapidity-dependent corrections are very important for describing the hadron multiplicity distribution in rapidity, dN/dy , within the CGC framework [57]. As dN/dy does depend on rapidity rather strongly in RHIC heavy ion data, and also strongly (albeit less so) in the LHC data, it is very hard to describe this observable without the rapidity-dependent nonlinear evolution. It is possible that similar rapidity-dependent corrections may significantly affect (and potentially destroy) the long-range structure of the rapidity correlations present in classical gluon fields of the MV model. Note that progress on this issue has been made in [47], indicating that inclusion of small- x evolution still leaves the “ridge” reasonably flat in rapidity until $\Delta y \sim 1/\alpha_s$.

To elucidate the above questions and concerns, and to improve the precision of the CGC predictions for the “ridge”-like correlations, it is important to be able to calculate the two-particle correlation in the CGC framework beyond the lowest order. While some works do consider the role of small- x evolution and multiple rescatterings in the correlation function [47, 49, 58–60], most of the phenomenological approaches [47, 48, 61–63] simply include the saturation effects into the lowest-order calculation by evolving the unintegrated gluon distributions with the running-coupling BK (rcBK) nonlinear evolution [64–66]. This is not correct due to the fact that these methods do not consider all orders of saturation effects in the ions and it isn’t exactly clear that the unintegrated gluon distributions can be used in this case (in fact we show that these distribution do not work, Sec. 5.2).

One has to keep in mind that in heavy ion collisions the early-stage azimuthal correlation may be washed out by the final state interactions leading to thermalization of the produced medium and its hydrodynamic evolution. (Note though, that the rapidity correlation is not likely to be strongly affected by such late-time dynamics.) It was argued, however, that the effect of the elliptic flow in the hydrodynamic evolution of the quark-gluon plasma (QGP) would be to (re-)introduce the azimuthal correlations [44].

1.5 Goals and organization of thesis

The aim of this work is to begin to analytically include saturation effects into the two-gluon correlation function in nucleus–nucleus collisions. Indeed full analytic inclusion of saturation effects originating in both nuclei would be a very hard problem: even the single gluon production in the quasi-classical MV limit of AA collisions can be dealt with only numerically at present [54, 55, 67, 68]. To make the problem more tractable we assume that one of the colliding nuclei is much larger than the other one, such that saturation effects are important only in interactions with the larger nucleus. This is known as the heavy-light ion regime.

Before going into the calculation itself, there are a few topics that need to be addressed. In Ch. 2 we will cover some of these topics in detail. In Sec. 2.1 we review more in depth the QCD Lagrangian and discuss some aspects of gauge fixing. Sec. 2.2 is reserved to describe and justify the heavy-light ion regime used in this work and to show exactly how this affects the two-gluon correlation function.

In Ch. 3 we review the known result for single-gluon production in pA collisions within the saturation framework in the classical MV limit. Doing this in detail serves

as a pedagogical way of seeing how exactly this framework is used in practice and its overall implications. At the same time many of the results derived here can be easily extended to more complicated situations, allowing us to derive the two-gluon correlations more efficiently. The major topics covered are shock wave generation in the target nucleus (Sec. 3.1), with the analysis of the resulting shock wave presented in (Sec. 3.3), the pA single-gluon production cross section (Sec. 3.2) and its k_T -factorized form (Sec. 3.4).

In Ch. 4, using the same formalism described in the previous chapter (Ch. 3), we calculate the two-gluon production cross section in the heavy-light ion regime. There are three types of contributions. The first type is known as the “square” terms (diagrams), Sec. 4.1.2, while the remaining two are called the “crossed” terms (diagrams), Sec. 4.1.3. With a close analysis of the resulting correlation function in Sec. 4.2, we see three distinct types of long-range rapidity correlations: one which is peaked in azimuthal angle on the near-side ($\Delta\phi = 0$), an equal-and-opposite correlation on the away-side ($\Delta\phi = \pi$), and a correlation that seems to be similar to a Hanbury Brown and Twiss (HBT) correlation which are peaked when the transverse momenta of the particles are the same and when they are equal and opposite ($\mathbf{k}_1 = \mathbf{k}_2$ and $\mathbf{k}_1 = -\mathbf{k}_2$). All of the two-gluon correlations produced in this heavy-light ion regime are symmetric in azimuthal angle ($\Delta\phi$).

In Ch. 5 we cover two more implications of the two-gluon production cross section and correlation function derived in Ch. 4. Sec. 5.1 shows that in collisions of asymmetric ions (examples being uranium and gold) the effects of saturation give rise to correlations that behave differently than those originating from hydrodynamical flow. We focus on uranium–uranium (U+U) collisions and show that there is

an enhancement of two-particle correlations in tip-on-tip collisions when compared with side-on-side collisions, which is opposite of that predicted by hydrodynamics. In Sec. 5.2 we derive the k_T -factorized form of the two-gluon production cross section in the heavy-light ion limit. The end result is that, unlike the pA case, the cross section cannot be written in terms of the usual unintegrated gluon distributions. Instead we must introduce gluon distributions which are in fact Wigner distributions, depending on both transverse momentum and transverse position. Finally in Ch. 6 we conclude with a brief overview of the major results presented herein.

Chapter 2: Quantitative details of QCD, the heavy–light ion regime and it’s effect on the correlation function

As a brief aside, we list the conventions used for the remainder of this dissertation. From now on, this work uses natural units, where $\hbar = 1$ and $c = 1$ unless specified otherwise. Einstein notation, where the sum over repeated indices is implied, is used for both vector and color indices. Feynman slash notation is used, meaning $\not{k} = \gamma^\mu k_\mu$ where k_μ is some 4-vector and γ^μ are the Dirac matrices. We work with light-cone coordinates which are $x^\mu = (x^+, x^-, \mathbf{x})$ where $x^+ = \frac{x^0 + x^3}{\sqrt{2}}$, $x^- = \frac{x^0 - x^3}{\sqrt{2}}$, $\mathbf{x} = (x^1, x^2)$ is the transverse vector and we define $x_\perp = |\mathbf{x}|$ (some works in the literature do not have the factor of $\frac{1}{\sqrt{2}}$ in the definition of x^+ and x^- , this is a choice of convention). Our convention results in, for the dot product of two 4 vectors, $x \cdot y = x^+ y^- + x^- y^+ - \mathbf{x} \cdot \mathbf{y}$.

Before we begin with the rest of the calculation we need to go over a few more topics. First, we need to cover some quantitative details about QCD which we skipped over in Sec. 1.1. Second, we go over, in detail, what we mean by the heavy-light ion regime and how this affects our approach to the two-particle correlation function calculation. Last, we look at the quantitative definition of the two-particle correlation function and already, just by using the heavy-light ion regime, notice that we have non-trivial correlations that depend purely on the geometry of the colliding ions.

2.1 Details of QCD

As discussed previously in Sec. 1.1, QCD is a non-Abelian $SU(N_c)$ gauge theory. Here N_c is the number of fundamental color charges and, in the case of QCD, is 3. It is more convenient to keep track of the number of colors in terms of N_c as opposed to setting this to 3 since later on in this work we will be using 't Hooft's large- N_c limit.

The Lagrangian which governs QCD is [8]

$$\mathcal{L}_{QCD} = \sum_{\text{flavors } f} \bar{q}_f (i \not{D}_\mu - m_f) q_f - \frac{1}{4} F_{\mu\nu}^a F^{a\mu\nu} \quad (2.1)$$

where

$$D_\mu = \partial_\mu - i t^a A_\mu^a \quad (2.2)$$

$$F_{\mu\nu}^a = \partial_\mu A_\nu^a - \partial_\nu A_\mu^a + g f^{abc} A_\mu^b A_\nu^c \quad (2.3)$$

are known as the covariant derivative and the gluon field strength tensor respectively.

Here q_f and \bar{q}_f are the quark and anti-quark spinor fields, respectively, with flavor f and mass m_f . A_μ^a is the gauge vector field (in the case of QCD this is the gluon) with color index a , which runs from 1 to $N_c^2 - 1$. t^a are the fundamental generators of the $SU(N_c)$ group. These consist of $N_c^2 - 1$ different N_c by N_c matrices. The normalization used for these generators is such that

$$[t^a, t^b] = i f^{abc} t^c \quad \text{tr}[t^a t^b] = \frac{\delta^{ab}}{2}.$$

where f^{abc} are the structure constants. There are also the adjoint generators defined as $(T^a)^{bc} = -i f^{abc}$ which are often used in the literature.

One of the primary features of a gauge theory is that it is invariant under a local gauge transformation. This means that the Lagrangian and the observables of the

theory are invariant under the transformation. For $SU(N_c)$ theories the quark and gluon fields transform as

$$\begin{aligned}
q(x) &\rightarrow S(x)q(x) \\
\bar{q}(x) &\rightarrow \bar{q}(x)S^{-1}(x) \\
A_\mu(x) &\rightarrow S(x)A_\mu(x)S^{-1}(x) - \frac{i}{g}[\partial_\mu S(x)]S^{-1}(x)
\end{aligned} \tag{2.4}$$

where

$$S(x) = e^{i\alpha^a(x)t^a} \tag{2.5}$$

Here $\alpha^a(x)$ is a real function with color index a .

As mentioned earlier, we are working in the limit where $\alpha_s \ll 1$. This allows us to use perturbation theory to do the calculations, where we expand around the free-theory. This is done by quantizing the theory using the usual path-integral formulation of quantum field theory. For the gauge fields (gluons in the case of QCD) we use the usual De Witt–Faddeev–Popov method [69]. To do this we break the gauge invariance of the system by setting the gauge condition, determining the form of the gluon propagator and the ghost fields. In this work we are using the light-cone gauge where $A^+ = 0$. Normally this method introduces ghosts into the calculations but this is not so in the light-cone gauge as they do not contribute to physical observables [70]. From here the Feynman rules are derived, which are used for the perturbative calculations. For more details on this topic see [15, 71, 72].

The Feynman rules we use are the usual rules presented in [72] except, since those were derived in the Feynman gauge, we use a different gluon propagator and do not consider ghosts. In the light-cone gauge, for a gluon with momentum k and indices

μ, ν , the gluon propagator is

$$\frac{-i}{k^2 + i\epsilon} \left(g_{\mu\nu} - \frac{\eta_\mu k_\nu + \eta_\nu k_\mu}{k^+} \right), \quad (2.6)$$

where η_μ is defined such that $\eta \cdot k = k^+$ for any 4-vector. The second term in the bracket has a singularity when $k^+ = 0$ and is known as the light-cone pole. In general this pole has to be regulated which introduces new subtleties into the calculation (see [70]). However it turns out that in the calculations presented here we never have to worry about this pole so these subtleties are neglected. For an on-shell gluon with momentum k and polarization λ we have

$$\epsilon_\lambda^\mu = \left(0, \frac{\epsilon_\lambda \cdot \mathbf{k}}{k^+}, \epsilon_\lambda \right). \quad (2.7)$$

where

$$\sum_\lambda \epsilon_{\lambda,i}^* \epsilon_{\lambda,j} = \delta_{ij}. \quad (2.8)$$

With this we have enough information to start to understand how the rest of the calculation works.

2.2 Heavy-light ion regime

In the saturation framework, Sec. 1.3, we view each ion as a large bag full of nucleons, where each of the nucleons is classical color sources which produces the gluon fields. In order to calculate the full heavy-heavy collision case one would need to consider all of the nucleons of both the target and projectile simultaneously. This is an incredibly hard problem and we currently do not have the ability to do this. However, one can consider the heavy-light ion case, where we consider all of the nucleons in the target but only a finite number of nucleons in the projectile.

Due to the high-energy nature of these collisions we can consider the dynamics of the source nucleons separately from the dynamics of the gluon production itself. We can calculate the cross sections associated with the processes of interest, single- and two-gluon production, by convoluting the square of the wave functions associated with the nucleon distribution with the cross sections of the gluon production due to the collisions of these individual nucleons.

Denote the 1- and 2-nucleon wave functions of the projectile nucleus A_1 by $\Psi_I(\mathbf{b})$ and $\Psi_{II}(\mathbf{b}_1, \mathbf{b}_2)$: they are normalized such that

$$\int d^2b |\Psi_I(\mathbf{b})|^2 = A_1, \quad \int d^2b_1 d^2b_2 |\Psi_{II}(\mathbf{b}_1, \mathbf{b}_2)|^2 = A_1 (A_1 - 1) \approx A_1^2. \quad (2.9)$$

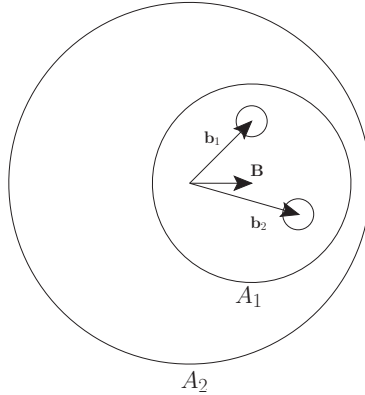


Figure 2.1: Transverse plane geometry of the two-particle production in the collision of a smaller projectile nucleus (A_1) with a larger target nucleus (A_2). The two smaller circles represent two nucleons in the nucleus A_1 (see text for details).

With the help of these wave functions, contributions to the single-gluon production cross section from the one- and two-nucleon(s) in the projectile case can be written as

$$\frac{d\sigma_I}{d^2kdy} = \int d^2B d^2b |\Psi_I(\mathbf{B} - \mathbf{b})|^2 \left\langle \frac{d\sigma^{pA_2}}{d^2kdyd^2b} \right\rangle \quad (2.10a)$$

$$\frac{d\sigma_{II}}{d^2kdy} = \int d^2B d^2b_1 d^2b_2 |\Psi_{II}(\mathbf{B} - \mathbf{b}_1, \mathbf{B} - \mathbf{b}_2)|^2 \left\langle \frac{d\sigma^{pp+A_2}}{d^2kdy d^2b_1 d^2b_2} \right\rangle \quad (2.10b)$$

and contributions to the two-gluon production cross section from the one- and two-nucleon(s) in the projectile case can be written as

$$\frac{d\sigma_I}{d^2k_1dy_1 d^2k_2dy_2} = \int d^2B d^2b |\Psi_I(\mathbf{B} - \mathbf{b})|^2 \left\langle \frac{d\sigma^{pA_2}}{d^2k_1dy_1 d^2k_2dy_2 d^2b} \right\rangle \quad (2.11a)$$

$$\begin{aligned} \frac{d\sigma_{II}}{d^2k_1dy_1 d^2k_2dy_2} &= \int d^2B d^2b_1 d^2b_2 |\Psi_{II}(\mathbf{B} - \mathbf{b}_1, \mathbf{B} - \mathbf{b}_2)|^2 \\ &\times \left\langle \frac{d\sigma^{pp+A_2}}{d^2k_1dy_1 d^2b_1 d^2k_2dy_2 d^2b_2} \right\rangle \end{aligned} \quad (2.11b)$$

where \mathbf{B} is the impact parameter between the two nuclei and \mathbf{b} , \mathbf{b}_1 , \mathbf{b}_2 the transverse positions of the nucleons in the projectile nucleus, all measured with respect to the center of the second (target) nucleus, as shown in Fig. 2.1 for two nucleons in the projectile. (Transverse vector \mathbf{b} labels the position of the incoming nucleon in the single nucleon case, while \mathbf{b}_1 and \mathbf{b}_2 label positions of projectile nucleons for the two nucleon case as shown in Fig. 2.1.)

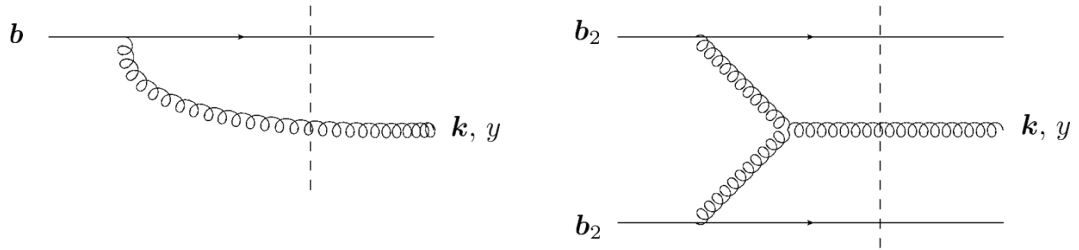


Figure 2.2: A sample Feynman diagram for each of the single-gluon production processes considered. The diagrams show a single gluon being produced by a collision of one- or two-nucleons with the target nucleus (left and right diagram respectively). The dashed line represents the interaction with the target (also known as the shock wave) which takes into account all of the multiple rescatterings with the target nucleons.

In Eq. 2.10,

$$\frac{d\sigma^{pA_2}}{d^2kdyd^2b} \quad \text{and} \quad \frac{d\sigma^{pp+A_2}}{d^2kdyd^2b_1d^2b_2}$$

are the cross sections for single-gluon production (with fixed transverse momentum \mathbf{k} and rapidity y) in: the collision of a single nucleon (p with fixed transverse position \mathbf{b}) with the target nucleus, and the collision of two nucleons (pp with fixed transverse positions \mathbf{b}_1 and \mathbf{b}_2) with the target nucleus, respectively. A diagrammatic example of each process is shown in Fig. 2.2.

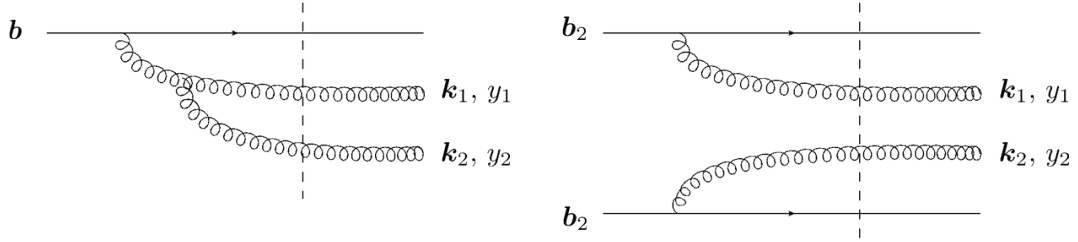


Figure 2.3: A sample Feynman diagram for each of the two-gluon production processes is considered. The diagrams show two gluon being produced by a collision of one- or two-nucleons with the target nucleus (left and right diagram respectively). The dashed line represents the interaction with the target (also known as the shock wave).

In Eq. 2.11,

$$\frac{d\sigma^{pA_2}}{d^2k_1dy_1d^2k_2dy_2d^2b} \quad \text{and} \quad \frac{d\sigma^{pp+A_2}}{d^2k_1dy_1d^2b_1d^2k_2dy_2d^2b_2}$$

are the cross sections for two-gluon production (with fixed transverse momenta \mathbf{k}_1 , \mathbf{k}_2 and rapidities y_1 , y_2) in: the collision of a single nucleon (p with fixed transverse position \mathbf{b}) with the target nucleus, and in the collision of two nucleons (pp with fixed transverse positions \mathbf{b}_1 and \mathbf{b}_2), with the target nucleus, respectively. A diagrammatic example of each process is shown in Fig. 2.3, where the interaction with the target

nucleon is represented by a dashed line. It should be noted that sometimes we use a red box to notate the interaction to emphasize the finite thickness of the target; details of this are presented in Ch. 3. The angle brackets $\langle \dots \rangle$ in 2.11 and 2.10 denote averaging in the target nucleus wave function along with summation over all the nucleons in the target nucleus [30–36, 73].

The idea behind the shock wave representation of the interactions with the target nucleus is as follows: Since the interaction is at high energies the target is Lorentz contracted and can be thought of approximately as a flat pancake (grouped around $x^+ = 0$). The target can be thought of as a source of color fields. The incoming quark or gluon interacts with the many color fields, referred to as the multiple rescatterings. Due to the computation details of the calculation, explained in Sec. 3.1, multiple re-scatterings do not change trajectory of the particle much, allowing us to treat the interaction with the target as a shock wave. Fig. 2.4 shows a pictorial representation of this.

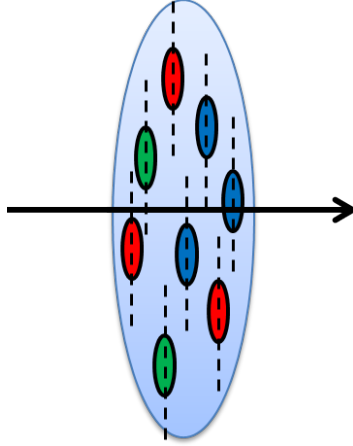


Figure 2.4: A quark or a gluon (black arrow) passes through the target (grey oval) and interacts with the many fields (dashed lines) originating from the color sources (red, green and blue ovals). The kinematics of the interaction are such that it does not change the trajectory of the particle much allowing us to treat the interaction with the target as a shock wave. This is described in more detail in Sec. 3.1.

Here we model the nucleus as a bag of independent nucleons, which is a correct description at the leading order in the atomic number A [34–36, 73–75]. In such case the single-nucleon light-cone wave function squared is simply equal to the nuclear profile function in the projectile nucleus,¹

$$|\Psi_I(\mathbf{b})|^2 = T_1(\mathbf{b}). \quad (2.12)$$

The nuclear profile function for a nucleus with the nucleon number density $\rho(\mathbf{b}, z)$ is defined by the integral over the longitudinal coordinate z ,

$$T(\mathbf{b}) = \int_{-\infty}^{\infty} dz \rho(\mathbf{b}, z). \quad (2.13)$$

¹We do not show the spin and isospin indices explicitly in the wave functions: in our notation the wave function squared is implicitly averaged over all nucleon polarizations, since both colliding nuclei are unpolarized.

This means $T(\mathbf{b}) \sim A^{\frac{1}{3}}$. For a spherical nucleus of radius R and constant density ρ , $T(\mathbf{b}) = 2\rho\sqrt{R^2 - b^2}$.

For a sufficiently large projectile nucleus, $A_1 \gg 1$, one can assume that the two-nucleon wave function can be factorized,

$$\Psi_{II}(\mathbf{b}_1, \mathbf{b}_2) = \Psi_I(\mathbf{b}_1) \Psi_I(\mathbf{b}_2), \quad (2.14)$$

such that, with the help of 2.12 we can write

$$|\Psi_{II}(\mathbf{b}_1, \mathbf{b}_2)|^2 = T_1(\mathbf{b}_1) T_1(\mathbf{b}_2). \quad (2.15)$$

The nuclear profile function $T(\mathbf{b})$ is closely related what is known as the saturation scale Q_s^2 (this quantity ends up having important physical significance as will be seen later). Every nucleon involved in the interaction introduces a power of Q_s^2 into the final result (shown in Ch. 3). This is why we refer to considering more nucleons in the process as saturation corrections. At the classical level, the saturation scale for a nucleon at transverse position \mathbf{b} originating from nucleus i is $Q_{s,i}^2(\mathbf{b}) = 4\pi\alpha_s^2 T_i(\mathbf{b})$ (it should be noted that when the saturation scale is in the classical limit it is often notated as Q_{s0}^2 , but in our case, since we are dealing purely at the classical level and have two different saturation scales to worry about, the notation presented here seemed appropriate). The α_s^2 in the saturation scale comes from the fact that every interaction with a nucleon involves at least two gluons.

Perturbative dynamics that we employ happens over short transverse distances and, at the leading order, involves a single quark inside nucleon while being insensitive to the non-perturbatively long distances of the order of Λ_{QCD}^{-1} . We assume that the quark involved in the interaction is a valence quark, following the original MV model [34–36]. This assumption can easily be generalized to a more realistic case if we

use the sum of sea and valence quark distributions instead of a simple valance quark distribution implicitly assumed in our calculations.

Since $Q_{s,i}^2 \sim \alpha_s^2 A_i^{\frac{1}{3}}$, every nucleon introduces a power of $\alpha_s^2 A_i^{\frac{1}{3}}$ ($i = 1$ or 2 for the projectile and target respectively). Using the heavy-light ion regime ($1 \ll A_1 \ll A_2$, $\alpha_s^2 A_1^{\frac{1}{3}} \ll 1$ and $\alpha_s^2 A_2^{\frac{1}{3}} \sim 1$) we can find which of the processes shown in Figs. 2.2 and 2.3 dominate. Since target nucleon corrections are order of $\mathcal{O}(1)$ we do not include these explicitly while examining the power counting.

Here we are examining the overall power counting of the single-gluon production processes, Eqs. 2.10. Since both of these processes are producing a single classical gluon we gain a factor of $\frac{1}{\alpha_s}$ for both. For the single- and two-nucleon processes with one and two projectile saturation scale corrections in the projectile bringing in $\alpha_s^2 A_1^{\frac{1}{3}}$ and $(\alpha_s^2 A_1^{\frac{1}{3}})^2$ respectively, the resulting power counting is,

$$\frac{d\sigma_I}{d^2k dy} \sim \frac{1}{\alpha_s} \left(\alpha_s^2 A_1^{\frac{1}{3}} \right) \quad \text{and} \quad \frac{d\sigma_{II}}{d^2k dy} \sim \frac{1}{\alpha_s} \left(\alpha_s^2 A_1^{\frac{1}{3}} \right)^2. \quad (2.16)$$

Since the two-nucleon process is suppressed by the saturation scale, $\alpha_s^2 A_1^{\frac{1}{3}} \ll 1$, the single-nucleon process dominates single-gluon production in heavy-light ion collisions. The single-gluon production cross section is, to leading order, described by 2.10a where we drop the subscript I .

The power counting for the two-gluon production processes, Eqs 2.11, follows a similar procedure. For the single-nucleon process we have one order in projectile saturation scale, $\alpha_s^2 A_1^{\frac{1}{3}}$, but instead of gaining a factor of $\frac{1}{\alpha_s}$ for each produced gluon, due to the extra gluon emission from the nucleon, the correction is order 1. For the two-nucleon process there are two orders of projectile saturation scale, $\left(\alpha_s^2 A_1^{\frac{1}{3}} \right)^2$, and each gluon gives a factor of $\frac{1}{\alpha_s}$. This gives rise to the following power counting,

$$\frac{d\sigma_I}{d^2k_1 dy_1 d^2k_2 dy_2} \sim \left(\alpha_s^2 A_1^{\frac{1}{3}}\right) \quad \text{and} \quad \frac{d\sigma_{II}}{d^2k_1 dy_1 d^2k_2 dy_2} \sim \frac{1}{\alpha_s^2} \left(\alpha_s^2 A_1^{\frac{1}{3}}\right)^2 = \alpha_s^2 \left(A_1^{\frac{1}{3}}\right)^2 \quad (2.17)$$

From the above expression we see that the two-nucleon process has an enhancement of $A_1^{\frac{1}{3}}$ when compared with the single-nucleon process. The two-gluon production cross section is thus dominated by 2.11b where we drop the subscript II .

Taking the dominant terms for both the single- and two-gluon production cross section and replacing the wave functions squared with the nuclear profile function according to 2.12 and 2.15 we arrive at the corresponding expression for the single- and two-gluon production cross sections respectively. 2.11a giving

$$\frac{d\sigma}{d^2k dy} = \int d^2B d^2b T_1(\mathbf{B} - \mathbf{b}) \left\langle \frac{d\sigma^{pA_2}}{d^2k dy d^2b} \right\rangle, \quad (2.18a)$$

$$\begin{aligned} \frac{d\sigma}{d^2k_1 dy_1 d^2k_2 dy_2} &= \int d^2B d^2b_1 d^2b_2 T_1(\mathbf{B} - \mathbf{b}_1) T_1(\mathbf{B} - \mathbf{b}_2) \\ &\times \left\langle \frac{d\sigma^{pp+A_2}}{d^2k_1 dy_1 d^2b_1 d^2k_2 dy_2 d^2b_2} \right\rangle, \end{aligned} \quad (2.18b)$$

where only the nuclear profile function T_1 depends on the impact parameter \mathbf{B} . It is useful to note that we can perform the integral over \mathbf{B} in 2.18a and obtain

$$\frac{d\sigma}{d^2k dy} = A_1 \int d^2b \left\langle \frac{d\sigma^{pA_2}}{d^2k dy d^2b} \right\rangle. \quad (2.19)$$

While for pedagogical purposes we use the form in 2.18a for much of the single-gluon production cross section derivation in Ch. 3, it is more convenient to use 2.19 when calculating the correlation function as will be seen in the next section (Sec. 2.3).

Armed with a knowledge of the general power counting associated with the heavy-light ion regime, thus the dominant contributions, we proceed to examine how these results affect the two-gluon correlation function of interest.

2.3 Definition of the correlation function

2.3.1 Definition of the correlator

Following a standard approach used in experimental analyses of particle correlations [41, 76] the correlation function can be defined as

$$C(\mathbf{k}_1, y_1, \mathbf{k}_2, y_2) = \mathcal{N} \frac{\frac{dN_{12}}{d^2k_1 dy_1 d^2k_2 dy_2}}{\frac{dN}{d^2k_1 dy_1} \frac{dN}{d^2k_2 dy_2}} - 1 \quad (2.20)$$

where

$$\frac{dN}{d^2k_1 dy_1} = \frac{1}{\sigma_{inel}} \frac{d\sigma}{d^2k_1 dy_1} \quad (2.21)$$

and

$$\frac{dN_{12}}{d^2k_1 dy_1 d^2k_2 dy_2} = \frac{1}{\sigma_{inel}} \frac{d\sigma}{d^2k_1 dy_1 d^2k_2 dy_2} \quad (2.22)$$

are the single- and double-particle multiplicity distributions with σ_{inel} the net inelastic nucleus–nucleus scattering cross section. The normalization factor \mathcal{N} in 2.20 is fixed by requiring that the number of particle pairs measured in the same (“real”) event N_{12} is equal to the number of (“mixed”) pairs with particles coming from different events $(N)^2$. Here we are interested in $\Delta\eta$ - $\Delta\phi$ correlations. For such a correlation, with the magnitudes of the transverse momenta k_{1T} and k_{2T} constrained to some chosen data bins, the normalization factor is fixed by

$$\mathcal{N} \int d\phi_1 dy_1 d\phi_2 dy_2 \frac{dN_{12}}{d^2k_1 dy_1 d^2k_2 dy_2} = \int d\phi_1 dy_1 \frac{dN}{d^2k_1 dy_1} \int d\phi_2 dy_2 \frac{dN}{d^2k_2 dy_2}. \quad (2.23)$$

(We assume for simplicity that the number of produced particles is very large, $N \gg 1$, such that $N - 1 \approx N$ and σ_{inel} is the same in both Eqs. 2.21 and 2.22 since the production cross section of producing exactly one particle is negligible.)

Combining Eqs. 2.20, 2.21, 2.22, and 2.23 we rewrite the correlation function in terms of cross sections as

$$C(\mathbf{k}_1, y_1, \mathbf{k}_2, y_2) = \frac{\left[\int d\phi_1 dy_1 \frac{d\sigma}{d^2k_1 dy_1} \int d\phi_2 dy_2 \frac{d\sigma}{d^2k_2 dy_2} \right]}{\left[\int d\phi_1 dy_1 d\phi_2 dy_2 \frac{d\sigma}{d^2k_1 dy_1 d^2k_2 dy_2} \right]} \frac{\frac{d\sigma}{d^2k_1 dy_1 d^2k_2 dy_2}}{\frac{d\sigma}{d^2k_1 dy_1} \frac{d\sigma}{d^2k_2 dy_2}} - 1. \quad (2.24)$$

Using the forms of the cross sections derived earlier, 2.19 and 2.18b, yields

$$\begin{aligned} C(\mathbf{k}_1, y_1, \mathbf{k}_2, y_2) = & \frac{\left[\int d^2b_1 d\phi_1 dy_1 \left\langle \frac{d\sigma^{pA_2}}{d^2k_1 dy_1 d^2b_1} \right\rangle \right] \left[\int d^2b_2 d\phi_2 dy_2 \left\langle \frac{d\sigma^{pA_2}}{d^2k_2 dy_2 d^2b_2} \right\rangle \right]}{\left[\int d^2B d^2b_1 d^2b_2 d\phi_1 dy_1 d\phi_2 dy_2 T_1(\mathbf{B} - \mathbf{b}_1) T_1(\mathbf{B} - \mathbf{b}_2) \left\langle \frac{d\sigma^{pp+A_2}}{d^2k_1 dy_1 d^2b_1 d^2k_2 dy_2 d^2b_2} \right\rangle \right]} \\ & \times \frac{\int d^2B d^2b_1 d^2b_2 T_1(\mathbf{B} - \mathbf{b}_1) T_1(\mathbf{B} - \mathbf{b}_2) \left\langle \frac{d\sigma^{pp+A_2}}{d^2k_1 dy_1 d^2b_1 d^2k_2 dy_2 d^2b_2} \right\rangle}{\int d^2b_1 \left\langle \frac{d\sigma^{pA_2}}{d^2k_1 dy_1 d^2b_1} \right\rangle \int d^2b_2 \left\langle \frac{d\sigma^{pA_2}}{d^2k_2 dy_2 d^2b_2} \right\rangle} - 1. \end{aligned} \quad (2.25)$$

To complete the calculation one needs the single- and double-gluon production cross sections which, when used in 2.25, would give us the correlation function. Before we proceed to construct them, let us study a simple example elucidating the nature of one of the correlation types contained in correlator 2.25, which we call “geometric” correlations.

2.3.2 Geometric correlations

Let us consider the simplest possible example of particle (gluon) production mechanism where the interaction of the two nucleons in the first nucleus with the second nucleus in 2.18b factorizes,

$$\left\langle \frac{d\sigma^{pp+A_2}}{d^2k_1 dy_1 d^2b_1 d^2k_2 dy_2 d^2b_2} \right\rangle \propto \left\langle \frac{d\sigma^{pA_2}}{d^2k_1 dy_1 d^2b_1} \right\rangle \left\langle \frac{d\sigma^{pA_2}}{d^2k_2 dy_2 d^2b_2} \right\rangle. \quad (2.26)$$

This contribution comes from the disconnected Feynman diagrams and is usually identified as the uncorrelated part of the two-gluon production cross section. However,

it is clear that substituting 2.26 into 2.25 does not reduce the correlation function to zero: instead one gets

$$\begin{aligned}
C(\mathbf{k}_1, y_1, \mathbf{k}_2, y_2) = & \frac{\left[\int d^2b_1 d\phi_1 dy_1 \left\langle \frac{d\sigma^{pA_2}}{d^2k_1 dy_1 d^2b_1} \right\rangle \right] \left[\int d^2b_2 d\phi_2 dy_2 \left\langle \frac{d\sigma^{pA_2}}{d^2k_2 dy_2 d^2b_2} \right\rangle \right]}{\left[\int d^2B d^2b_1 d^2b_2 d\phi_1 dy_1 d\phi_2 dy_2 T_1(\mathbf{B} - \mathbf{b}_1) T_1(\mathbf{B} - \mathbf{b}_2) \left\langle \frac{d\sigma^{pA_2}}{d^2k_1 dy_1 d^2b_1} \right\rangle \left\langle \frac{d\sigma^{pA_2}}{d^2k_2 dy_2 d^2b_2} \right\rangle \right]} \\
& \times \frac{\int d^2B d^2b_1 d^2b_2 T_1(\mathbf{B} - \mathbf{b}_1) T_1(\mathbf{B} - \mathbf{b}_2) \left\langle \frac{d\sigma^{pA_2}}{d^2k_1 dy_1 d^2b_1} \right\rangle \left\langle \frac{d\sigma^{pA_2}}{d^2k_2 dy_2 d^2b_2} \right\rangle}{\int d^2b_1 \left\langle \frac{d\sigma^{pA_2}}{d^2k_1 dy_1 d^2b_1} \right\rangle \int d^2b_2 \left\langle \frac{d\sigma^{pA_2}}{d^2k_2 dy_2 d^2b_2} \right\rangle} - 1, \quad (2.27)
\end{aligned}$$

which, in general, could be non-zero. Notice that the overall proportionality constant from 2.26 canceled.

Certainly if the \mathbf{b} -dependence factorizes from the rapidity and azimuthal dependence in the single-gluon production cross section in the pA case

$$\left\langle \frac{d\sigma^{pA_2}}{d^2k dy d^2b} \right\rangle, \quad (2.28)$$

then the correlation function 2.27 is zero: however, such factorization is not always the case. For gluon production in the saturation framework, the cross section is a complicated function of $k_T/Q_s(\mathbf{b}, y)$, which means it is not in a factorized form and thus the correlator 2.27 is not zero. Note that in the MV model (which does not contain the small- x evolution), gluon production is rapidity-independent, and, if one neglects the dependence of the gluon production cross section on the angle between \mathbf{k} and \mathbf{b} , the correlator 2.27 becomes zero. (Dependence of gluon production cross section on the collision geometry in the MV approximation is not very strong, peaking at non-perturbatively low momenta [77].)

For the general case in 2.27 we observe a possible non-trivial correlation in the two-gluon production described by *disconnected* Feynman diagrams. If the gluon production cross section 2.28 is a slowly varying (but not constant) function of rapidity,

as is the case in the saturation/CGC framework near mid-rapidity, this correlation would be long-range in rapidity. The origin of this correlation is somewhat peculiar: even though the two-nucleon wave function in 2.15 is factorized and, hence, represents uncorrelated nucleons, these two nucleons are correlated by the simple fact of being parts of the same bound state, the projectile nucleus. In other words, the probability of finding two nucleons at the impact parameters \mathbf{b}_1 and \mathbf{b}_2 is proportional to

$$\sim \int d^2B T_1(\mathbf{B} - \mathbf{b}_1) T_1(\mathbf{B} - \mathbf{b}_2) \quad (2.29)$$

and is not a product of two independent probabilities after all impact parameters \mathbf{B} of the incoming nucleus are integrated over: this is a correlation. Note also that the presence of real wave-function correlations, that is, non-factorizable corrections to the right-hand-side of 2.15, would also lead to some nontrivial two-particle correlations in 2.27.

If we define the correlation function at the fixed nuclear impact parameter \mathbf{B} by not integrating over \mathbf{B} in 2.10a and 2.11b and using the result in 2.24, we get

$$\begin{aligned} C(\mathbf{k}_1, y_1, \mathbf{k}_2, y_2; \mathbf{B}) = & \\ & \frac{\left[\int d^2b_1 d\phi_1 dy_1 |\Psi_I(\mathbf{B} - \mathbf{b}_1)|^2 \left\langle \frac{d\sigma^{pA_2}}{d^2k_1 dy_1 d^2b_1} \right\rangle \right] \left[\int d^2b_2 d\phi_2 dy_2 |\Psi_I(\mathbf{B} - \mathbf{b}_2)|^2 \left\langle \frac{d\sigma^{pA_2}}{d^2k_2 dy_2 d^2b_2} \right\rangle \right]}{\left[\int d^2b_1 d^2b_2 d\phi_1 dy_1 d\phi_2 dy_2 |\Psi_{II}(\mathbf{B} - \mathbf{b}_1, \mathbf{B} - \mathbf{b}_2)|^2 \left\langle \frac{d\sigma^{pp+A_2}}{d^2k_1 dy_1 d^2b_1 d^2k_2 dy_2 d^2b_2} \right\rangle \right]} \\ & \times \frac{\int d^2b_1 d^2b_2 |\Psi_{II}(\mathbf{B} - \mathbf{b}_1, \mathbf{B} - \mathbf{b}_2)|^2 \left\langle \frac{d\sigma^{pp+A_2}}{d^2k_1 dy_1 d^2b_1 d^2k_2 dy_2 d^2b_2} \right\rangle}{\int d^2b_1 |\Psi_I(\mathbf{B} - \mathbf{b}_1)|^2 \left\langle \frac{d\sigma^{pA_2}}{d^2k_1 dy_1 d^2b_1} \right\rangle \int d^2b_2 |\Psi_I(\mathbf{B} - \mathbf{b}_2)|^2 \left\langle \frac{d\sigma^{pA_2}}{d^2k_2 dy_2 d^2b_2} \right\rangle} - 1, \end{aligned} \quad (2.30)$$

One can see that this fixed-impact parameter correlation function in 2.30 is zero, $C(\mathbf{B}) = 0$, for the factorized wave function from 2.15 and for disconnected-diagram interactions from 2.26. Thus di-gluon correlations due to our “geometric” correlation mechanism seem to also disappear when the impact parameter is fixed exactly.

However, such precise determination of the impact parameter is typically not done in an experimental analysis, one fixes the collision centrality $|\mathbf{B}|$ in a certain interval, but usually does not fix the direction of \mathbf{B} . The integration over any range of the impact parameter $|\mathbf{B}|$ (or the integration over the angles of \mathbf{B} keeping $|\mathbf{B}|$ constant) is likely to introduce these geometric correlations, as follows from 2.25. Note that the presence of non-trivial wave function correlations, i.e., correlations beyond the factorization approximation in 2.15, may also lead to correlations which may survive in 2.30 even for a fixed impact parameter \mathbf{B} and uncorrelated interactions 2.26.

Despite its simplicity, the non-vanishing correlation in 2.27 is one of the main results of this work. In the saturation/CGC framework it may lead to long-range rapidity correlations similar to the observed “ridge” correlation. Indeed azimuthal correlations are missing in 2.27: such correlations may be formed in heavy ion collisions due to radial flow, as was argued in [44]. Indeed a lot more work is needed to compare this result with experiment.

2.4 Summary

In this section we covered a few topics that were needed before we go into detailed derivations of gluon production in heavy-light ion collisions. First we reviewed some basics of QCD in order to understand some of the mathematics behind it. Secondly we described in detail what the heavy-light ion regime implies in the calculation at hand. This regime determined the types of cross sections that dominate the two-gluon correlation functions. Even without knowing the explicit form of these cross sections we noticed a type of correlations which we called “geometric” correlations. These

correlations depend only on the initial geometry of the collision and are completely independent of the dynamics of the interaction itself.

Chapter 3: Review of single-gluon production

In this chapter we review the calculation for the single inclusive gluon production cross section taking into account a single nucleon in the target. We use this as a pedagogical way to explain, in detail, how saturation formalism is used in practice. This serves a number of purposes. Not only do we need the analytic form of the cross section itself, but the various equations derived here are useful when looking at more complicated situations. By going through the derivation carefully we can highlight the various approximations and techniques used throughout. These approximations are often stated in the literature but not clearly justified so it is helpful to go through these in a rigorous manner, not only to justify them but to show exactly how these approximations can break down in more complicated situations. Various techniques used throughout the derivation can also be extended into other situations, so we will demonstrate them here for later use.

3.1 Target nucleus as a shock wave

Due to the power counting associated with the target nucleus, $\alpha_s^2 A_2^{\frac{1}{3}} \sim 1$, we consider all of the nucleons in the target when calculating the cross section. This seems like a daunting task at first but using the eikonal approximation and the light-cone gauge, $A^+ = 0$, this becomes feasible. Under these conditions, each individual

nucleon can be viewed as emitting gluon fields which are not only localized at a specific light-cone time x^+ but to eikonal accuracy do not change the light-cone energy k^+ of either quarks or gluons originating from the projectile. To examine how this comes about we calculate the gluon field emitted by a single nucleon from the target.

We model the nucleon as a massless eikonal quark, which implies the following: First, it is massless and has a large P^- momentum (P^+ for projectile quarks) which dominates over all other momentum scales in the problem except the momenta of the other color source quarks (either projectile or target) in the problem. We also only keep the leading-order terms in P^- . Second, we view the quark as a classical source which feels no back reaction. In other words, it has infinite P^- momentum such that when it emits a gluon with momentum k^- it still has momentum P^- even if we integrated over all values of k^- , which means $P^- - k^- \approx P^-$. This may seem like a poor approximation, however it is the same approximation as the one used when solving Maxwell's equations for a given electric current.

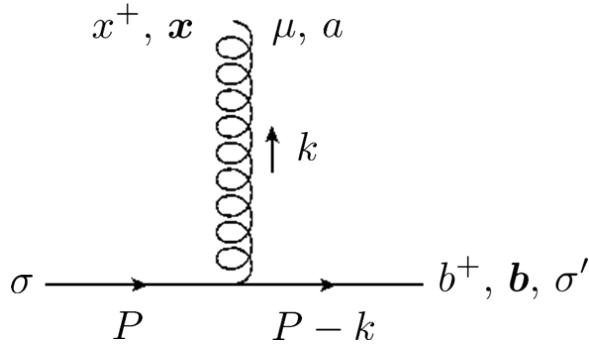


Figure 3.1: The Feynman diagram associated with the classical gluon field emitted by a target nucleon, $A_{MV,\mu}^a$. The nucleon is represented by a massless, eikonal valence quark traveling in the x^- direction. Due to the fact that the outgoing and incoming quark lines are on mass-shell the outgoing quark has $b^- = \infty$.

To find the produced classical gluon field, notated $A_{MV,\mu}^a$, we evaluate the Feynman diagram shown in Fig. 3.1. The massless eikonal quark travels in the x^- direction with initial momentum $P = (0, P^-, \mathbf{0})$ and emits a single off-shell gluon with momentum k . The outgoing quark has momentum $(-k^+, P^- - k^-, -\mathbf{k})$ and is on-shell, resulting in a delta function that sets the momentum squared to zero, $\delta((P - k)^2)$. The spins of the incoming and outgoing quarks, σ and σ' respectively, are averaged over. The outgoing gluon has vector index μ and color index a . Here we are not keeping track of the quark color indices explicitly.

It ends up being more convenient to have the final result in coordinate space so we include the Fourier transform over k^- and \mathbf{k} , resulting in an expression which depends on the coordinates $(x^+ - b^+)$ and $(\mathbf{x} - \mathbf{b})$. From the Feynman diagram we arrive at the following expression:

$$A_{MV,\mu}^a = \frac{1}{2} \sum_{\sigma,\sigma'} \int \frac{d^4k}{(2\pi)^4} e^{-ik^+x^- - ik^-(x^+ - b^+) + i\mathbf{k}\cdot(\mathbf{x} - \mathbf{b})} \bar{u}'_{\sigma'}(P - k) i g t^a \gamma^\nu u_\sigma(P) \times \frac{-i}{k^2 + i\epsilon} \left(g_{\mu\nu} - \frac{1}{k^+} (\eta_\mu k_\nu + \eta_\nu k_\mu) \right) 2\pi \delta((P - k)^2). \quad (3.1)$$

To further evaluate this equation a few steps are required.

First, we need to evaluate the spinors associated with the quark line which is done by splitting it up into parts. By using the Dirac equation we can evaluate the contraction of $\bar{u}'_{\sigma'}(P - k) \gamma^\nu u_\sigma(P)$ with $(\eta_\mu k_\nu + \eta_\nu k_\mu)$. Looking at the k_ν term we see that by adding and subtracting P_ν ,

$$\bar{u}'_{\sigma'}(P - k) \not{k} u_\sigma(P) = \bar{u}'_{\sigma'}(P - k) (\not{P} - (\not{P} - \not{k})) u_\sigma(P) = 0, \quad (3.2)$$

this contribution is exactly zero. Examining the η_ν term and noticing that $\gamma^+ \propto \not{P}$ we see this contribution vanishes as well,

$$\eta_\nu \gamma^\nu u_\sigma(P) = \gamma^+ u_\sigma(P) \propto \not{P} u_\sigma(P) = 0. \quad (3.3)$$

Analyzing the contraction of $\bar{u}'_\sigma(P-k)\gamma^\nu u_\sigma(P)$ with the remaining $g_{\mu\nu}$ term using the spinor identities in [23, 78] (where we switch from the γ^+ basis to the γ^- basis), we arrive at

$$g_{\mu\nu}\bar{u}'_\sigma(P-k)\gamma^\nu u_\sigma(P) \approx g_{\mu-}\bar{u}'_\sigma(P-k)\gamma^- u_\sigma(P) = \eta_\mu 2P^- \delta_{\sigma'\sigma} \quad (3.4)$$

where we have used the eikonal limit to neglect terms subleading in P^- . The delta function can be similarly analyzed and, once again taking the eikonal limit by neglecting $\frac{k_\perp^2}{2P^-}$, we arrive at

$$\delta((P-k)^2) \approx \frac{1}{2P^-} \delta(k^+) \quad (3.5)$$

Using these results equation 3.1 becomes

$$A_{MV,\mu}^a = -g t^a \eta_\mu \frac{1}{2} \sum_{\sigma,\sigma'} \delta_{\sigma'\sigma} \int \frac{d^4 k}{(2\pi)^3} e^{-ik^+ x^- - ik^-(x^+ - b^+) + ik \cdot (\mathbf{x} - \mathbf{b})} \frac{-1}{k_\perp^2 + i\epsilon} \delta(k^+). \quad (3.6)$$

From here, summing and averaging over the spins and integrating over k^+ gives

$$A_{MV,\mu}^a = -g t^a \eta_\mu \int \frac{dk^-}{2\pi} \frac{d^2 k}{(2\pi)^2} e^{-ik^-(x^+ - b^+) + ik \cdot (\mathbf{x} - \mathbf{b})} \frac{1}{k_\perp^2}. \quad (3.7)$$

At this point we need to evaluate the remaining Fourier transforms. The k^- integral gives rise to a delta function (with the usual normalization factor of 2π) while the transverse momentum integral gives rise to a logarithmic term (see Appendix A in [23]) resulting in the final expression

$$A_{MV,\mu}^a = -\eta_\mu \frac{g}{2\pi} t^a \delta(x^+ - b^+) \ln \frac{1}{|\mathbf{x} - \mathbf{b}| \Lambda}, \quad (3.8)$$

where Λ is some IR cutoff which is on the order of Λ_{QCD} .

This result has a few interesting properties. First, the vector field only consists of a single component η^μ . Second, the field is instantaneous: It is located at a single

light-cone time, b^+ . It also has no k^+ momentum, meaning it does not change the plus momentum of any particle it interacts with. All of these properties end up being useful when trying to sum over an arbitrary number of scatterings. At this point it is helpful to define the following field:

$$A_{MV,i}^{a,-}(x^+, \mathbf{x}) = -\frac{g}{2\pi} t_i^a \delta(x^+ - b_i^+) \ln \frac{1}{|\mathbf{x} - \mathbf{b}_i| \Lambda}. \quad (3.9)$$

This is the classical gluon field produced by nucleon i , which lies at coordinates b_i^+ and \mathbf{b}_i . As we will see, this notation is useful when considering many scatterings.

With an expression for the classical gluon field emitted by a single nucleon in the target in hand, we can now see what happens when a quark interacts with many of these fields. To start, consider the case of a quark interacting with two different nucleons, one with coordinates b_1^+ and \mathbf{b}_1 where the exchanged gluon has color a , the other with coordinates b_2^+ and \mathbf{b}_2 where the exchanged gluon has color b , shown in Fig. 3.2. The quark interacts with the field of nucleon 1 at position x^+, \mathbf{x} and with the field of nucleon 2 at position y^+, \mathbf{y} . The interaction with these fields does not change the plus momentum of the quark, hence $q_i^+ = q^+ = q_f^+$. The knowledge of these positions implies that the remaining momenta are not conserved at the vertices.

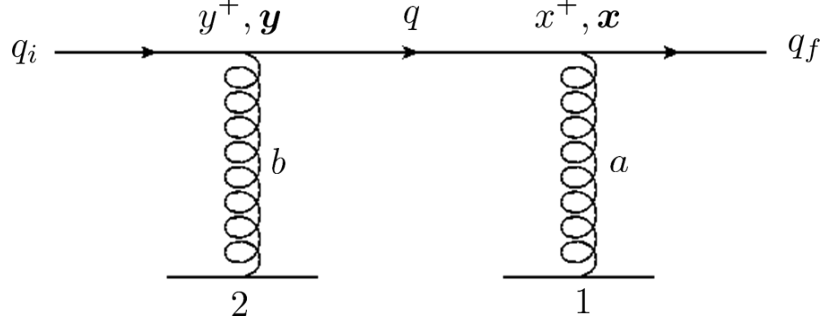


Figure 3.2: Feynman diagram representing a projectile quark interacting with the classical gluon fields emitted from nucleons 1 and 2. The external lines of the projectile quark are dropped in the calculation.

Since all but the plus momenta are not conserved at the vertices we can analyze the Feynman diagram in Fig. 3.2 while ignoring the external quark propagators. We only keep track of the vertices, the quark propagator with momentum q and the fields due to the two nucleons. The expression for this truncated diagram is

$$\begin{aligned}
V_2 = & \int \frac{dq^-}{2\pi} \frac{d^2q}{(2\pi)^2} e^{iq^-(x^+-y^+)-iq\cdot(x-y)} i g t^a \gamma^+ \frac{i \not{q}}{q^2 + i\epsilon} i g t^b \gamma^+ \\
& \times A_{MV,1}^{a,-}(x^+, \mathbf{x}) A_{MV,2}^{b,-}(y^+, \mathbf{y}), \tag{3.10}
\end{aligned}$$

which we temporarily call V_2 for notational purposes. Focusing on only a part of the expression and using $\gamma^+ \not{q} \gamma^+ = 2q^+$, we evaluate the q^- and \mathbf{q} integrals:

$$\begin{aligned}
& \int \frac{dq^-}{2\pi} \frac{d^2q}{(2\pi)^2} e^{-iq^-(x^+-y^+)+iq\cdot(x-y)} \gamma^+ \frac{i \not{q}}{q^2 + i\epsilon} \gamma^+ \\
& = \int \frac{dq^-}{2\pi} \frac{d^2q}{(2\pi)^2} e^{-iq^-(x^+-y^+)+iq\cdot(x-y)} \gamma^+ \gamma^- \gamma^+ \frac{iq^+}{q^2 + i\epsilon} \\
& = \gamma^+ \int \frac{dq^-}{2\pi} \frac{d^2q}{(2\pi)^2} e^{-iq^-(x^+-y^+)+iq\cdot(x-y)} \frac{i}{q^- - \frac{\mathbf{q}^2}{2q^+} + i\epsilon} \\
& = \gamma^+ \Theta(x^+ - y^+) \int \frac{d^2q}{(2\pi)^2} e^{-i\frac{q^2}{2q^+}(x^+-y^+)+iq\cdot(x-y)}. \tag{3.11}
\end{aligned}$$

At this point, we use the approximation that the separation between the nucleons in the shock wave in the plus direction, $x^+ - y^+$, is small and the plus momentum of the quark is large, q^+ , such that $\frac{q^2}{2q^+}(x^+ - y^+) \approx 0$. Since it requires a large q^+ momentum it is also considered an eikonal approximation. It should be noted that this approximation gives the condition that $q_{\perp}^2 \ll \frac{2q^+}{x^+ - y^+}$, but since $\frac{2q^+}{x^+ - y^+}$ is large we make the approximation that we can integrate \mathbf{q} over all values. Thus, the \mathbf{q} integral results in a 2-dimensional delta function of the transverse coordinates. The entire expression can then be written as

$$V_2 = i g t^a A_{MV,1}^{a,-}(x^+, \mathbf{x}) i g t^b A_{MV,2}^{b,-}(y^+, \mathbf{x}) \Theta(x^+ - y^+) \delta^2(\mathbf{x} - \mathbf{y}). \quad (3.12)$$

This means that a quark scattering off the classical fields produced by the nucleons results in a time ordered scattering (in the x^+ direction) where the transverse position of the quark remains fixed along with its q^+ momentum. This can be generalized for any number of nucleons and results in a path-ordered exponential, a Wilson line, that runs from the point of last scattering, x^+ , to the point of first scattering, y^+ (this is a well known result [20, 26]). The result for both quarks, $V_{\mathbf{x}}[x^+, y^+]$ (known as the fundamental representation), and gluons (known as the adjoint representation), $U_{\mathbf{x}}^{ab}[x^+, y^+]$, are shown below.

$$V_{\mathbf{z}}[x^+, y^+] = \text{P exp} \left\{ i g \int_{y^+}^{x^+} dz^+ A^-(z^+, \mathbf{z}) \right\} \quad (3.13)$$

$$U_{\mathbf{z}}[x^+, y^+] = \text{P exp} \left\{ i g \int_{y^+}^{x^+} dz^+ \mathcal{A}^-(z^+, \mathbf{z}) \right\}, \quad (3.14)$$

Here, $A^-(x^+, \mathbf{x})$ and $\mathcal{A}^-(x^+, \mathbf{x})$ are the total color fields produced by the target in the fundamental and adjoint representations, respectively. In the classical limit, the

limit derived above and notated by a MV subscript, these are just the sum of all the fields produced by the nucleons,

$$A_{MV}^-(x^+, \mathbf{x}) = \sum_{i=1}^N t^a A_{MV,i}^{a,-}(x^+, \mathbf{x}) \quad (3.15)$$

$$\mathcal{A}_{MV}^-(x^+, \mathbf{x}) = \sum_{i=1}^N T^a A_{MV,i}^{a,-}(x^+, \mathbf{x}), \quad (3.16)$$

where $A_{MV,i}^{a,-}(x^+, \mathbf{x})$ was defined in 3.9.

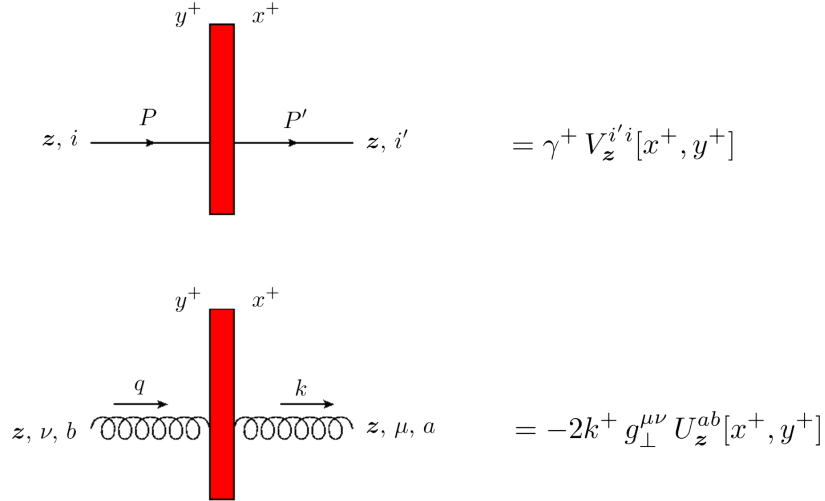


Figure 3.3: Feynman rules associated with quarks and gluons passing through a shockwave induced by the target nucleus. The shockwave is denoted by a red box.

The Feynman rules associated with these shockwave interactions are shown in Fig. 3.3. The shockwaves do not change the transverse position of the particles nor do they change the plus momentum of the particles ($P'^+ = P^+$ and $k^+ = q^+$). The other momenta of the particles, the minus and transverse, are not conserved. The color indices of the Wilson lines represent the initial and final colors introduced by the scatterings, $(t^a t^b \dots t^c)^{i'i}$ for quarks and $(T^c T^d \dots T^e)^{ab}$ for gluons. We notated

the plus position of the final, x^+ , and initial, y^+ , scatterings. At the end of the day, with the approximations used, the Wilson lines are independent of these terms but, at this point in our discussion, we do not know if the finite size of the shock wave could have any repercussions later on in the calculation.

Now with a clear understanding of how the quarks and gluons, originating from the projectile, interact with the gluon fields produced by the target we now approach the pA single gluon production case.

3.2 Single-gluon production cross section

To calculate the single-gluon production cross section for the pA case we first need to calculate the amplitude of the process, which has two contributing diagrams. One diagram has the projectile nucleon (modeled as a valence quark) emitting the produced gluon before the interaction such that both the valance quark and the gluon interact with the target (modeled as a shock wave). The other has the gluon emitted after the interaction, only the quark ends up interacting with the target. Both are shown in Fig. 3.4.

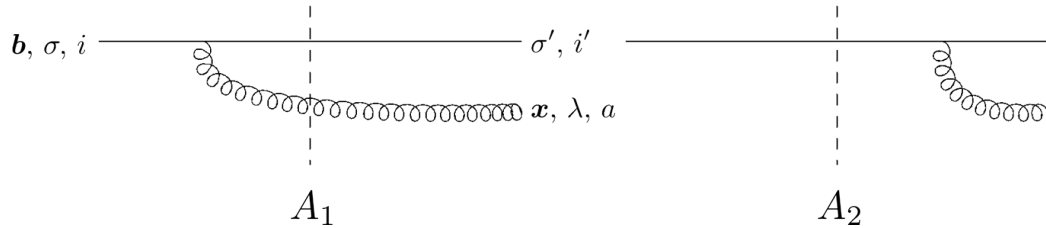


Figure 3.4: Single-gluon production amplitudes. The dashed line represents the shock wave due to the interaction with the target.

As a pedagogical exercise, which gives more insight into later calculations, we explicitly calculate diagram A_1 , shown in Fig. 3.4 and in more detail in Fig. 3.5. We use the usual Feynman rules for QCD in the light-cone gauge while adding in the additional rules associated with the shock wave interactions derived in the previous section, shown in Fig. 3.3.

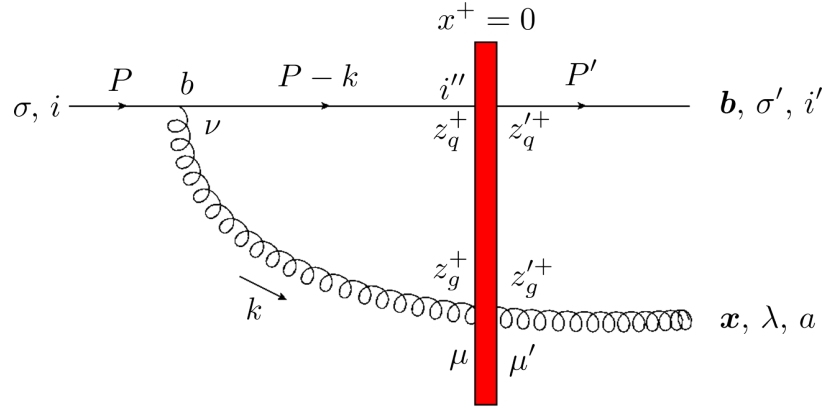


Figure 3.5: An eikonal quark originating from the projectile emits a gluon before passing through the shock wave. The shock wave is a red box to emphasize that the shock wave has some finite thickness.

The eikonal quark originating from the projectile travels in the x^+ direction with momentum $P = (P^+, 0, \mathbf{0})$, spin σ , color i and at transverse position \mathbf{b} . It emits an off shell gluon, with momentum k , and both the quark and emitted gluon pass through the shock wave, which changes neither their transverse coordinates nor their plus momenta, P^+ and k^+ respectively, due to the eikonal approximation. The final state quark has spin σ' , color i' and the same plus momentum P^+ . Similar to the calculation done in the previous section, the outgoing quark being on shell gives rise to a factor of $\frac{1}{2P^+}$. The final state gluon has transverse coordinate \mathbf{x} , color a ,

polarization vector λ and a plus momentum of k^+ . Also as before we want to know the amplitude in terms of the transverse coordinates \mathbf{b} and \mathbf{x} . This requires us to Fourier transform k^- and \mathbf{k} . Including all of these considerations for diagram A_1 we arrive at the expression

$$\begin{aligned}
A_1 = & \int \frac{dk^-}{2\pi} \frac{d^2k}{(2\pi)^2} e^{-ik^-(z_g^+ - z_q^+) + i\mathbf{k} \cdot (\mathbf{x} - \mathbf{b})} \frac{1}{2P^+} \bar{u}_{\sigma'}(P') \gamma^+ V_{\mathbf{b}}^{i'i''}[z_q^+, z_q^+] \frac{i(\not{P} - \not{k})}{(P - k)^2 + i\epsilon} \\
& \times ig \gamma^\nu (t^b)^{i''i} u_\sigma(P) \frac{-i}{k^2 + i\epsilon} \left(g_{\mu\nu} - \frac{\eta_\mu k_\nu + \eta_\nu k_\mu}{k^+} \right) \left(-2k^+ g_\perp^{\mu'\mu} U_{\mathbf{x}}^{ab}[z_g^+, z_g^+] \right) \epsilon_{\lambda, \mu'}^*.
\end{aligned} \tag{3.17}$$

First we analyze the quark line associated with the projectile quark, evaluating both the color structure and the spinors in the eikonal limit. We use the same spinor identities used in the calculation of the classical gluon field presented in the previous section (except this time in the same γ^+ basis presented in the sources [23, 78]) to evaluate the quark line spinors:

$$\begin{aligned}
& \frac{1}{2P^+} \bar{u}_{\sigma'}(P') \gamma^+ V_{\mathbf{b}}^{i'i''}[z_q^+, z_q^+] \frac{i(\not{P} - \not{k})}{(P - k)^2 + i\epsilon} i\gamma^\nu (t^b)^{i''i} u_\sigma(P) \\
& \approx \frac{1}{2P^+} \bar{u}_{\sigma'}(P') \gamma^+ V_{\mathbf{b}}^{i'i''}[z_q^+, z_q^+] \frac{iP^+ \gamma^-}{-P^+ k^- + i\epsilon} i\gamma^\nu (t^b)^{i''i} u_\sigma(P) \\
& = \frac{1}{2P^+} \frac{1}{k^- - i\epsilon} (V_{\mathbf{b}}[z_q^+, z_q^+] t^b)^{i'i} \bar{u}_{\sigma'}(P') \gamma^+ \gamma^- \gamma^\nu u_\sigma(P) \\
& \approx \frac{1}{k^- - i\epsilon} (V_{\mathbf{b}}[z_q^+, z_q^+] t^b)^{i'i} \delta_{\sigma'\sigma} g^{-\nu}.
\end{aligned} \tag{3.18}$$

Plugging this result into 3.17 we arrive at

$$\begin{aligned}
A_1 = & 2g \delta_{\sigma'\sigma} \int \frac{dk^-}{2\pi} \frac{d^2k}{(2\pi)^2} e^{-ik^-(z_g^+ - z_q^+) + i\mathbf{k} \cdot (\mathbf{x} - \mathbf{b})} \frac{i}{k^- - i\epsilon} \frac{\boldsymbol{\epsilon}_\lambda^* \cdot \mathbf{k}}{2k^+ k^- - k_\perp^2 + i\epsilon} \\
& \times U_{\mathbf{x}}^{ab}[z_g^+, z_g^+] (V_{\mathbf{b}}[z_q^+, z_q^+] t^b)^{i'i}.
\end{aligned} \tag{3.19}$$

At this point we first perform the Fourier transform over k^- ,

$$\begin{aligned}
& \int \frac{dk^-}{2\pi} e^{-ik^-(z_g^+ - z_q^+)} \frac{i}{k^- - i\epsilon} \frac{1}{2k^+k^- - k_\perp^2 + i\epsilon} \\
&= \Theta(z_g^+ - z_q^+) \frac{1}{k_\perp^2} e^{-i\frac{k_\perp^2}{2k^+}(z_g^+ - z_q^+)} + \Theta(z_q^+ - z_g^+) \frac{1}{k_\perp^2} \\
&\approx \frac{1}{k_\perp^2}.
\end{aligned} \tag{3.20}$$

Here we used the approximation that, since the width of the shock wave created by the target is small, $\frac{k_\perp^2}{2k^+}(z_g^+ - z_q^+) \approx 0$. It should be noted that this is the exact same approximation used in deriving 3.12 in the previous section. Since the exponential term is suppressed, we often approximate the Fourier transform as just an integral over k^- by setting the coordinates associated with the shock to be the same and at zero, $z_g^+ = z_q^+ = z_g'^+ = z_q'^+ = 0$, since the target nucleus is centered around $x^+ = 0$. This causes us to arrive at

$$A_1 = 2g \delta_{\sigma'\sigma} \int \frac{d^2k}{(2\pi)^2} e^{i\mathbf{k}\cdot(\mathbf{x}-\mathbf{b})} \frac{\boldsymbol{\epsilon}_\lambda^* \cdot \mathbf{k}}{k_\perp^2} U_{\mathbf{x}}^{ab} (V_{\mathbf{b}} t^b)^{i'i}. \tag{3.21}$$

where you will notice we have neglected the x^+ dependence of the end points of the Wilson lines. This is due to the fact that, with the approximations we are using, we can set the end points of the Wilson lines to to $x^+ = \pm\infty$ without loss of generality. This will be further be expanded upon in the next section.

Finally, performing the Fourier transform over \mathbf{k} , we arrive at

$$A_1 = \frac{ig}{\pi} \delta_{\sigma'\sigma} \frac{\boldsymbol{\epsilon}_\lambda^* \cdot (\mathbf{x} - \mathbf{b})}{|\mathbf{x} - \mathbf{b}|^2} U_{\mathbf{x}}^{ab} (V_{\mathbf{b}} t^b)^{i'i}. \tag{3.22}$$

This same process can be repeated for diagram A_2 giving

$$A_2 = -\frac{ig}{\pi} \delta_{\sigma'\sigma} \frac{\boldsymbol{\epsilon}_\lambda^* \cdot (\mathbf{x} - \mathbf{b})}{|\mathbf{x} - \mathbf{b}|^2} (t^a V_{\mathbf{b}})^{i'i}. \tag{3.23}$$

The total amplitude for the single inclusive gluon production cross section is the sum of these two diagrams, $A_1 + A_2$. By using the Wilson line identity $(t^a V_{\mathbf{b}})^{i'i} =$

$(V_{\mathbf{b}t^b})^{i'i} U_{\mathbf{b}}^{ab}$, the amplitude can be written in the compact form of

$$A_{\sigma'\sigma,\lambda}^{a,i'i}(\mathbf{x}, \mathbf{b}) = \frac{ig}{\pi} \delta_{\sigma'\sigma} \frac{\boldsymbol{\epsilon}_\lambda^* \cdot (\mathbf{x} - \mathbf{b})}{|\mathbf{x} - \mathbf{b}|^2} [U_{\mathbf{x}} - U_{\mathbf{b}}]^{ab} (V_{\mathbf{b}t^b})^{i'i}. \quad (3.24)$$

It turns out this same amplitude also appears in the 2-gluon production case so 3.24 will be used later, hence why we include all of the indices in the definition.

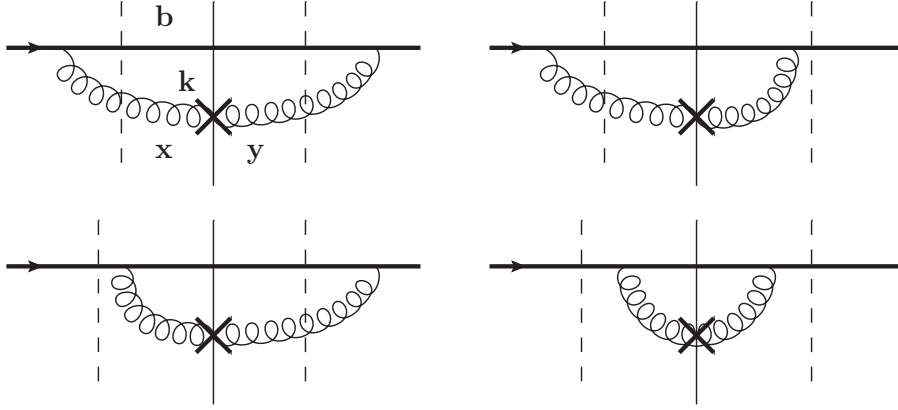


Figure 3.6: Diagrams contributing to the square of the scattering amplitude for the single gluon production in pA collisions. The cross denotes the measured produced gluon.

To find the cross section, we square the total amplitude while having the gluon's transverse position different on each side of the cut, \mathbf{x} and \mathbf{y} . This is shown in Fig. 3.6. To get the cross section in momentum space requires a Fourier transform over each transverse position. We sum and average over the colors and spins of the quark while only summing over the polarization and color of the produced gluon. Averaging over all possible charge configuration of the target, represented by $\langle \dots \rangle$, results in the following expression:

$$\begin{aligned} \left\langle \frac{d\sigma^{pA_2}}{d^2k dy d^2b} \right\rangle &= \frac{1}{2(2\pi)^3} \int d^2x d^2y e^{-i\mathbf{k}\cdot(\mathbf{x}-\mathbf{y})} \\ &\times \frac{1}{2N_c} \sum_{\sigma',\sigma} \sum_{\lambda} \left\langle \left(A_{\sigma'\sigma,\lambda}^{a,i'i}(\mathbf{y},\mathbf{b}) \right)^\dagger A_{\sigma'\sigma,\lambda}^{a,i'i}(\mathbf{x},\mathbf{b}) \right\rangle. \end{aligned} \quad (3.25)$$

Evaluating the integrand

$$\begin{aligned} &\frac{1}{2N_c} \sum_{\sigma',\sigma} \sum_{\lambda} \left(A_{\sigma'\sigma,\lambda}^{a,i'i}(\mathbf{y},\mathbf{b}) \right)^\dagger A_{\sigma'\sigma,\lambda}^{a,i'i}(\mathbf{x},\mathbf{b}) \\ &= \frac{g^2}{2N_c\pi^2} \sum_{\sigma',\sigma} \delta_{\sigma'\sigma} \delta_{\sigma'\sigma} \sum_{\lambda} \frac{\boldsymbol{\epsilon}_\lambda^* \cdot (\mathbf{x} - \mathbf{b})}{|\mathbf{x} - \mathbf{b}|^2} \frac{\boldsymbol{\epsilon}_\lambda \cdot (\mathbf{y} - \mathbf{b})}{|\mathbf{y} - \mathbf{b}|^2} \\ &\quad \times \text{tr}[t^c V_b^\dagger V_b t^b] \left[(U_{\mathbf{y}}^\dagger - U_{\mathbf{b}}^\dagger) (U_{\mathbf{x}} - U_{\mathbf{b}}) \right]^{cb} \\ &= \frac{g^2}{2N_c\pi^2} \frac{(\mathbf{x} - \mathbf{b}) \cdot (\mathbf{y} - \mathbf{b})}{|\mathbf{x} - \mathbf{b}|^2 |\mathbf{y} - \mathbf{b}|^2} \text{Tr} \left[(U_{\mathbf{x}} - U_{\mathbf{b}}) (U_{\mathbf{y}}^\dagger - U_{\mathbf{b}}^\dagger) \right] \end{aligned} \quad (3.26)$$

and plugging this into 3.25 we arrive at the known result [79]

$$\begin{aligned} \left\langle \frac{d\sigma^{pA_2}}{d^2k dy d^2b} \right\rangle &= \frac{\alpha_s C_F}{4\pi^4} \int d^2x d^2y e^{-i\mathbf{k}\cdot(\mathbf{x}-\mathbf{y})} \frac{\mathbf{x} - \mathbf{b}}{|\mathbf{x} - \mathbf{b}|^2} \cdot \frac{\mathbf{y} - \mathbf{b}}{|\mathbf{y} - \mathbf{b}|^2} \\ &\quad \times [S_G(\mathbf{x}, \mathbf{y}) - S_G(\mathbf{x}, \mathbf{b}) - S_G(\mathbf{b}, \mathbf{y}) + 1]. \end{aligned} \quad (3.27)$$

where $C_F = \frac{N_c^2 - 1}{2N_c}$ is the fundamental-representation Casimir operator and $S_G(\mathbf{x}, \mathbf{y})$ is the adjoint (gluon) dipole S -matrix

$$S_G(\mathbf{x}, \mathbf{y}) = \frac{1}{N_c^2 - 1} \langle \text{Tr}[U_{\mathbf{x}} U_{\mathbf{y}}^\dagger] \rangle. \quad (3.28)$$

It turns out, although not specified here, that one can include rapidity dependence of the emitted gluon into this expression by changing the form of S_G . In general it is written as $S_G(\mathbf{x}, \mathbf{y}, y)$ which corresponds to the classical case presented here when $y = 0$. To include rapidity dependence one uses the BK/JIMWLK evolution equations to evolve the dipole [80,81]. These effects, while important, are beyond the classical level of approximation we are dealing with here.

To get the single inclusive gluon production cross section for the heavy-light ion case, all that is left is inserting 3.27 into 2.19.

$$\begin{aligned} \frac{d\sigma}{d^2k dy} &= \frac{\alpha_s C_F}{4\pi^4} A_1 \int d^2b d^2x d^2y e^{-i\mathbf{k}\cdot(\mathbf{x}-\mathbf{y})} \frac{\mathbf{x}-\mathbf{b}}{|\mathbf{x}-\mathbf{b}|^2} \cdot \frac{\mathbf{y}-\mathbf{b}}{|\mathbf{y}-\mathbf{b}|^2} \\ &\times [S_G(\mathbf{x}, \mathbf{y}, y) - S_G(\mathbf{x}, \mathbf{b}, y) - S_G(\mathbf{b}, \mathbf{y}, y) + 1]. \end{aligned} \quad (3.29)$$

While the expression above is simple, it is meaningless unless the form of the adjoint (gluon) dipole S -matrix, $S_G(\mathbf{b}, \mathbf{y})$, is known.

3.3 Gluon dipole amplitude

Here we derive the well-known result for the gluon dipole S-Matrix, $S_G(\mathbf{x}, \mathbf{y})$, in the quasi-classical MV/Glauber–Mueller (GM) approximation. This may seem tedious and unnecessary since it has been known for years [74] but it gives valuable insight to the nature of the eikonal scatterings associated with the target and allows us to generalize to more complicated objects such as the double-dipole operator $\frac{1}{(N_c^2-1)^2} \langle Tr [U_{\mathbf{x}} U_{\mathbf{x}}] Tr [U_{\mathbf{x}} U_{\mathbf{x}}] \rangle$, which is needed for two-gluon production. More about this object is presented in Chapter 4 and Appendix A.

The exact object that is associated with the single gluon production cross section in the pA case 3.27 is

$$\frac{1}{N_c^2 - 1} \langle U_{\mathbf{x}}[z'^+, z^+] U_{\mathbf{y}}^\dagger[w'^+, w^+] \rangle, \quad (3.30)$$

where the angular brackets represent the averaging over all possible charge configurations of the target nucleus and the coordinates z'^+, z^+, w'^+, w^+ are associated with locations of the initial and final scatterings. Within the approximations used, the cross section is independent of the x^+ position of the initial and final scatterings. This includes both the Fourier transform over the k^- momentum and the Wilson

lines themselves. For these reasons we drop the x^+ dependence from the definition of $S_G(\mathbf{x}, \mathbf{y})$.

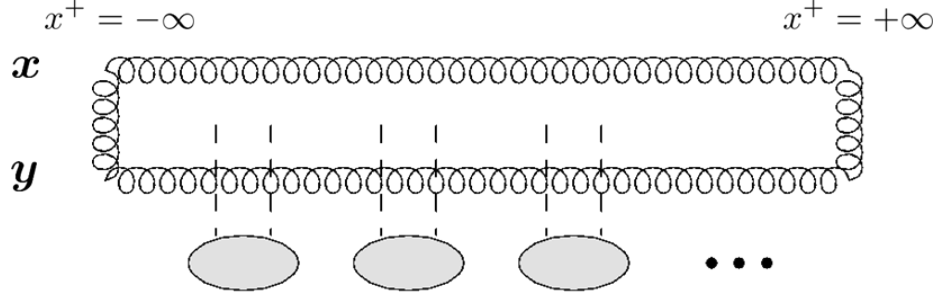


Figure 3.7: Graphical representation of the gluon dipole S-Matrix, $S_G(\mathbf{x}, \mathbf{y})$. The gray ovals represent different target nucleons and the dotted lines are the exchanged gluons. These gluons can either interact with the top or bottom Wilson line.

The way we interpret this object is presented in figure 3.7. Since the Wilson lines in S_G only contain interactions with the fields originating from the target we can consider the Wilson lines as traveling from $x^+ = -\infty$ to $x^+ = +\infty$. All of these target fields come with a vector component of η_μ , meaning they do not couple with Wilson lines traveling in the transverse direction. This allows us to insert two transverse gauge links at x^+ infinities into the object, which makes it gauge invariant. As the dipole passes through the target fields, to leading-order in saturation effects, it can only interact with at least two gluons from a target nucleon because when one averages over the colors of the nucleon source one has a trace of the fundamental generators associated with the quark line, $\text{tr}[t^a t^b]$. If only one gluon was exchanged this would give a trace of a single generator which is zero. Also, interactions with more than two gluons from a single nucleon are suppressed by α_s as each gluon interaction gives a power of α_s . We also must consider all possible charge configurations and

scatterings, meaning that we must consider the fact that only one or many nucleons may interact and that we must average over all possible transverse positions of said nucleons.

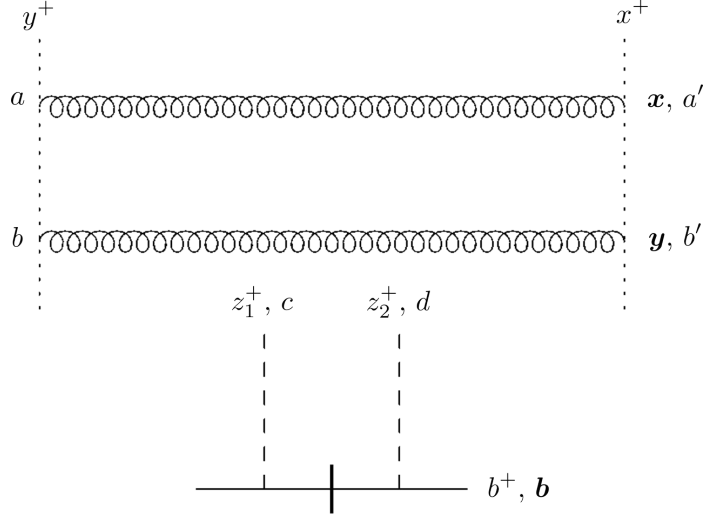


Figure 3.8: A finite section of the Wilson line object. The nucleon emits two gluon fields which interact with the two Wilson lines in all possible ways.

To see the effect the multiple rescatterings have on the gluon dipole let us consider how the interaction with a single nucleon works. We consider a finite section of the Wilson line object. There are two Wilson lines that both run from x^+ to y^+ and they lie at two different transverse positions, \mathbf{x} and \mathbf{y} . We keep track of the initial and final colors of the Wilson lines. These two Wilson lines interact with a single nucleon that lies at position b^+ such that $x^+ > b^+ > y^+$. We consider all possible gluon interactions between the target nucleon and the Wilson lines and average over the color and transverse position of said nucleon. This results in the expression

$$\begin{aligned}
& \left\langle U_{\mathbf{x}}^{a'a} [x^+, y^+] U_{\mathbf{y}}^{b'b} [x^+, y^+] \right\rangle_1 - \delta^{a'a} \delta^{b'b} \\
&= \left\langle g^2 \int_{y^+}^{x^+} dz^+ [T^c]^{a'e} A_{MV,1}^{c,-}(z^+, \mathbf{x}) \int_{y^+}^{z^+} dz'^+ [T^d]^{ea} A_{MV,1}^{d,-}(z'^+, \mathbf{x}) \delta^{b'b} \right. \\
&\quad + g^2 \delta^{a'a} \int_{y^+}^{x^+} dz^+ [T^c]^{b'e} A_{MV,1}^{c,-}(z^+, \mathbf{y}) \int_{y^+}^{z^+} dz'^+ [T^d]^{eb} A_{MV,1}^{d,-}(z'^+, \mathbf{y}) \\
&\quad \left. + g^2 \int_{y^+}^{x^+} dz^+ [T^c]^{a'a} A_{MV,1}^{c,-}(z^+, \mathbf{x}) \int_{y^+}^{x^+} dz'^+ [T^d]^{b'b} A_{MV,1}^{d,-}(z'^+, \mathbf{y}) \right\rangle_1 \quad (3.31)
\end{aligned}$$

where the angular brackets $\langle \dots \rangle_1$ represents averaging over all possible configurations of the nucleon, which we call nucleon 1. We have subtracted out the case where the dipole does not interact.

Keeping in mind that each field $A_{MV,1}^{a,-}(z^+, \mathbf{x})$, 3.9, comes with a delta function, $\delta(z^+ - b^+)$, which sets the location of the field equal to b_1^+ , we can replace $\int_{y^+}^{x^+} dz^+ \int_{y^+}^{z^+} dz'^+ \rightarrow \frac{1}{2} \int_{y^+}^{x^+} dz^+ dz'^+$ resulting in

$$\begin{aligned}
& \left\langle U_{\mathbf{x}}^{a'a} [x^+, y^+] U_{\mathbf{y}}^{b'b} [x^+, y^+] \right\rangle_1 - \delta^{a'a} \delta^{b'b} \\
&= -\frac{g^2}{2} [T^c T^d]^{a'a} \delta^{b'b} \int_{y^+}^{x^+} dz^+ dz'^+ \left\langle A_{MV,1}^{c,-}(z^+, \mathbf{x}) A_{MV,1}^{d,-}(z'^+, \mathbf{x}) \right\rangle_1 \\
&\quad - \frac{g^2}{2} \delta^{a'a} [T^c T^d]^{b'b} \int_{y^+}^{x^+} dz^+ dz'^+ \left\langle A_{MV,1}^{c,-}(z^+, \mathbf{y}) A_{MV,1}^{d,-}(z'^+, \mathbf{y}) \right\rangle_1 \\
&\quad - g^2 [T^c]^{a'a} [T^d]^{b'b} \int_{y^+}^{x^+} dz^+ dz'^+ \left\langle A_{MV,1}^{c,-}(z^+, \mathbf{x}) A_{MV,1}^{d,-}(z'^+, \mathbf{y}) \right\rangle_1. \quad (3.32)
\end{aligned}$$

At this point we need to average over the possible charge configurations of the target nucleon. This requires averaging over the color of the nucleon and convolving the fields with the nuclear profile function associated with the target nucleus, $T_2(\mathbf{b})$. Using the known equation for the classical gluon field $A_{MV,1}^{a,-}(z^+, \mathbf{x})$, 3.9, we have (doing a few simplifications in the process)

$$\begin{aligned}
& \int_{y^+}^{x^+} dz^+ dz'^+ \left\langle A_{MV,1}^{c,-}(x^+, \mathbf{x}) A_{MV,1}^{d,-}(y^+, \mathbf{y}) \right\rangle_1 \\
&= \frac{1}{N_c} \int_{y^+}^{x^+} dz^+ dz'^+ \int d^2b T_2(\mathbf{b}) \text{tr} \left[A_{MV,1}^{c,-}(x^+, \mathbf{x}) A_{MV,1}^{d,-}(y^+, \mathbf{y}) \right] \\
&= \frac{g^2}{N_c (2\pi)^2} \text{tr} [t^c t^d] \int d^2b T_2(\mathbf{b}) \ln \frac{1}{|\mathbf{x} - \mathbf{b}| \Lambda} \ln \frac{1}{|\mathbf{y} - \mathbf{b}| \Lambda}. \tag{3.33}
\end{aligned}$$

When doing the \mathbf{b} convolution it is common to use the approximation that the profile changes slowly with respect to the transverse width of the dipole, $|\mathbf{x} - \mathbf{y}|$. With this we can use the approximation that $T_2(\mathbf{b}) \approx T_2\left(\frac{\mathbf{x} + \mathbf{y}}{2}\right)$, which allows us to pull the nuclear profile function out of the integral. We also use the Fourier transform of $\ln \frac{1}{|\mathbf{x} - \mathbf{b}| \Lambda}$ to evaluate the rest of the expression

$$\begin{aligned}
& \int_{y^+}^{x^+} dz^+ dz'^+ \left\langle A_{MV,1}^{c,-}(x^+, \mathbf{x}) A_{MV,1}^{d,-}(y^+, \mathbf{y}) \right\rangle_1 \\
&= \frac{g^2}{2N_c} \delta^{cd} T_2\left(\frac{\mathbf{x} + \mathbf{y}}{2}\right) \int d^2b \int \frac{d^2k}{(2\pi)^2} \frac{d^2q}{(2\pi)^2} e^{-i\mathbf{k} \cdot (\mathbf{x} - \mathbf{b}) - i\mathbf{q} \cdot (\mathbf{y} - \mathbf{b})} \frac{1}{\mathbf{k}^2 \mathbf{q}^2} \\
&= \frac{g^2}{2N_c} \delta^{cd} T_2\left(\frac{\mathbf{x} + \mathbf{y}}{2}\right) \int \frac{d^2k}{(2\pi)^2} e^{-i\mathbf{k} \cdot (\mathbf{x} - \mathbf{y})} \frac{1}{|\mathbf{k}^2|^2} \tag{3.34}
\end{aligned}$$

Plugging this result in to 3.32 we arrive at

$$\begin{aligned}
& \left\langle U_{\mathbf{x}}^{a'a} [x^+, y^+] U_{\mathbf{y}}^{b'b} [x^+, y^+] \right\rangle_1 - \delta^{a'a} \delta^{b'b} = -\frac{g^4}{4\pi} T_2\left(\frac{\mathbf{x} + \mathbf{y}}{2}\right) \int \frac{d^2k}{2\pi} \frac{1}{|\mathbf{k}^2|^2} \\
& \times \left(\frac{1}{2N_c} \left([T^c T^c]^{a'a} \delta^{b'b} + \delta^{a'a} [T^c T^c]^{b'b} \right) + \frac{1}{N_c} [T^c]^{a'a} [T^c]^{b'b} e^{-i\mathbf{k} \cdot (\mathbf{x} - \mathbf{y})} \right) \\
& = -Q_{s,2}^2 \left(\frac{\mathbf{x} + \mathbf{y}}{2} \right) \int \frac{d^2k}{2\pi} \frac{1}{|\mathbf{k}^2|^2} \left(\delta^{a'a} \delta^{b'b} + \frac{1}{N_c} [T^c]^{a'a} [T^c]^{b'b} e^{-i\mathbf{k} \cdot (\mathbf{x} - \mathbf{y})} \right), \tag{3.35}
\end{aligned}$$

where we used $[T^c T^c]^{ab} = N_c \delta^{ab}$. We also used the definition of the saturation scale at the classical level, $Q_{s,2}^2(\mathbf{b}) = 4\pi \alpha_s^2 T_2(\mathbf{b})$, to replace the nuclear profile function with the saturation scale, since $T_2(\mathbf{b}) \sim A_2^{\frac{1}{3}}$. This allows us to directly see that for every nucleon that interacts with the target we pick up an order of $\alpha_s^2 A_2^{\frac{1}{3}}$ as promised.

The above equation tells us what we gain every time the Wilson lines interact with a single nucleon. While important, it is not the final result we need; we need

to consider what happens after many such scatterings. To do this we need to first notice that in the initial and final states, the Wilson lines, for $S_G(\mathbf{x}, \mathbf{y})$, are in a color singlet. This means that the term we pick up for each scattering is given by 3.35 when hit with δ^{ab} . Evaluating this we have

$$\begin{aligned} & \delta^{ab} \left\langle U_{\mathbf{x}}^{a'a} [x^+, y^+] U_{\mathbf{y}}^{b'b} [x^+, y^+] \right\rangle_1 - \delta^{a'b'} \\ &= -\delta^{a'b'} Q_{s,2}^2 \left(\frac{\mathbf{x} + \mathbf{y}}{2} \right) \int \frac{d^2k}{2\pi} \frac{1}{|\mathbf{k}^2|^2} (1 - e^{-i\mathbf{k}\cdot(\mathbf{x}-\mathbf{y})}). \end{aligned} \quad (3.36)$$

Using the relation

$$\int \frac{d^2k}{2\pi} \frac{1}{|\mathbf{k}^2|^2} (1 - e^{-i\mathbf{k}\cdot\mathbf{r}}) = \frac{1}{4} \mathbf{r}^2 \ln \frac{1}{|\mathbf{r}|\Lambda} \quad (3.37)$$

we can write this result as

$$\begin{aligned} \delta^{ab} \left\langle U_{\mathbf{x}}^{a'a} [x^+, y^+] U_{\mathbf{y}}^{b'b} [x^+, y^+] \right\rangle_1 - \delta^{a'b'} &= -\frac{\delta^{a'b'}}{4} |\mathbf{x} - \mathbf{y}|^2 Q_{s,2}^2 \left(\frac{\mathbf{x} + \mathbf{y}}{2} \right) \ln \frac{1}{|\mathbf{x} - \mathbf{y}|\Lambda} \\ &= -\delta^{a'b'} \Gamma_G(\mathbf{x}, \mathbf{y}) \end{aligned} \quad (3.38)$$

which defines $\Gamma_G(\mathbf{x}, \mathbf{y})$.

We can see that every time we hit a nucleon we gain a term which is a function of the transverse positions of the dipole, \mathbf{x} and \mathbf{y} , but keep the same color structure. So when we finally reach the end of the dipole (after scattering off the number of nucleons that are in the target) we end up with the color factor $\delta^{a'b'} \delta^{a'b'} = N_c^2 - 1$.

In order to find S_G we need to average over all possible charge configurations. If the dipole interacts with no charges we have a contribution of a factor of 1, while if dipole interacts with 1 charge we gain a factor of $-\Gamma_G(\mathbf{x}, \mathbf{y})$.

Now suppose the dipole interacts with two nucleons, labeled 1 and 2. The dipole could interact with nucleon 1 first then 2 or the other way around. This causes us to pick up a factor of $\Gamma_G^2(\mathbf{x}, \mathbf{y})$ since there are two interactions and a factor of $\frac{1}{2}$

to eliminate double-counting due to the fact that the nucleons are identical. For three nucleons we have $-\frac{1}{3!}\Gamma_G^3(\mathbf{x}, \mathbf{y})$ due to the three scatterings and the 6 possible orderings. This pattern continues on

$$1 - \Gamma_G(\mathbf{x}, \mathbf{y}) + \frac{1}{2}\Gamma_G^2(\mathbf{x}, \mathbf{y}) - \frac{1}{3!}\Gamma_G^3(\mathbf{x}, \mathbf{y}) + \dots = e^{-\Gamma_G(\mathbf{x}, \mathbf{y})} \quad (3.39)$$

and results, when one considers all possibilities, in an exponential function. So for the Gluon Dipole, we have [74]

$$S_G(\mathbf{x}, \mathbf{y}) = \exp \left[-\frac{1}{4}|\mathbf{x} - \mathbf{y}|^2 Q_{s,2}^2 \left(\frac{\mathbf{x} + \mathbf{y}}{2} \right) \ln \frac{1}{|\mathbf{x} - \mathbf{y}|\Lambda} \right]. \quad (3.40)$$

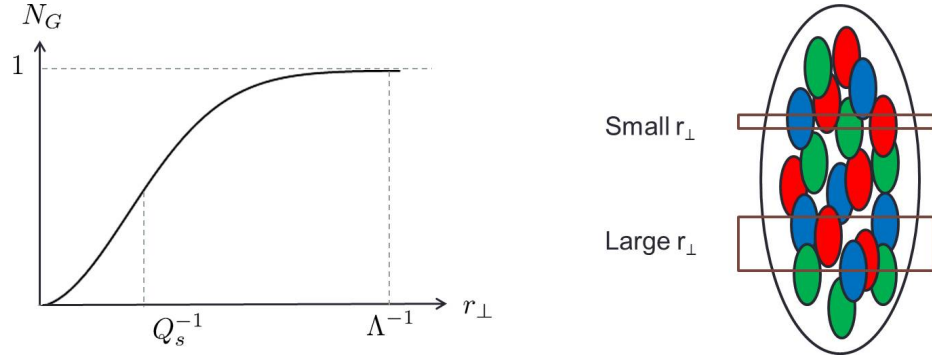


Figure 3.9: Left: Plot of the forward scattering amplitude, $N_G(\mathbf{x}, \mathbf{y})$, of the gluon dipole where $r_\perp = |\mathbf{x} - \mathbf{y}|$ is the transverse size of the dipole. To plot this we neglected dependence of the function on the nuclear profile function and the log dependence. Right: A pictorial representation of the physical picture. The smaller the dipole the less charge it sees so the nucleus is more transparent. The larger the dipole is the more charge it sees and the more opaque the target becomes. This continues until the dipole sees so much charge that the charges start to screen one another.

This result has a clear interpretation once we write this in terms of the forward scattering amplitude for the gluon dipole,

$$N_G(\mathbf{x}, \mathbf{y}) = 1 - S_G(\mathbf{x}, \mathbf{y}). \quad (3.41)$$

This tells us the probability of the gluon dipole passing through the target nucleus. The majority of the dependence comes from the size of the dipole which we write as $r_{\perp} = |\mathbf{x} - \mathbf{y}|$. When the dipole size is much less than the saturation scale, $r_{\perp} \ll Q_{s,2}^{-1}$, the dipole interacts with a small amount of color charge so the nucleus is fairly transparent. This causes the amplitude to scale as $\sim r_{\perp}^2$. However, when the dipole size is large when compared with the saturation scale, $r_{\perp} \gg Q_{s,2}^{-1}$, the dipole interacts with a large amount of color charge: the nucleus become opaque. This only extends to a certain point, because the charges end up screening each other, causing the target to saturate, reaching the black disc limit. A pictorial representation of this is seen in figure 3.9.

3.4 k_T -factorization for single-gluon production

It is a well-known result of saturation physics that the single-gluon production cross section in the proton-nucleus (pA) collisions calculated either in the quasi-classical or leading- $\ln 1/x$ evolution approximations can be cast in the form consistent with k_T -factorization [80, 82, 83].

Here we are going to derive this k_T -factorized expression for the heavy-light collision case in the quasi-classical approximation following the derivations presented in [19, 23]. Starting by using 3.27 in 2.18a we arrive at

$$\begin{aligned} \frac{d\sigma}{d^2k dy} &= \frac{\alpha_s C_F}{4 \pi^4} \int d^2B d^2b d^2x d^2y T_1(\mathbf{B}) e^{-i\mathbf{k}\cdot(\mathbf{x}-\mathbf{y})} \frac{\mathbf{x} - \mathbf{b}}{|\mathbf{x} - \mathbf{b}|^2} \cdot \frac{\mathbf{y} - \mathbf{b}}{|\mathbf{y} - \mathbf{b}|^2} \\ &\times [N_G(\mathbf{x}, \mathbf{b}, y) + N_G(\mathbf{b}, \mathbf{y}, y) - N_G(\mathbf{x}, \mathbf{y}, y)]. \end{aligned} \quad (3.42)$$

where we replaced the gluon dipole S -matrix with the gluon dipole forward scattering amplitude 3.41 and shifted the impact parameter \mathbf{B} such that the nuclear profile function no longer depends on \mathbf{B} .

Notice that each of the gluon dipole forward scattering amplitudes in 3.42 only depending on two of the transverse coordinates \mathbf{x} , \mathbf{y} , and \mathbf{b} . This leaves one coordinate that we are free to integrate out of the expression for each individual term. Doing this and renaming the remaining coordinates such that \mathbf{y} is no longer in the expression we arrive at

$$\begin{aligned}
\frac{d\sigma}{d^2k dy} &= \frac{\alpha_s C_F}{2\pi^3} \int d^2B T_1(\mathbf{B}) \left[- \int d^2x d^2y e^{-i\mathbf{k}\cdot(\mathbf{x}-\mathbf{y})} \ln \frac{1}{|\mathbf{x}-\mathbf{y}|\Lambda} N_G(\mathbf{x}, \mathbf{y}, y) \right. \\
&\quad + i \int d^2x d^2b e^{-i\mathbf{k}\cdot(\mathbf{x}-\mathbf{b})} \frac{\mathbf{k}}{k^2} \cdot \frac{\mathbf{x}-\mathbf{b}}{|\mathbf{x}-\mathbf{b}|^2} N_G(\mathbf{x}, \mathbf{b}, y) \\
&\quad \left. - i \int d^2y d^2b e^{-i\mathbf{k}\cdot(\mathbf{b}-\mathbf{y})} \frac{\mathbf{y}-\mathbf{b}}{|\mathbf{y}-\mathbf{b}|^2} \cdot \frac{\mathbf{k}}{k^2} N_G(\mathbf{b}, \mathbf{y}, y) \right] \\
&= \frac{\alpha_s C_F}{2\pi^3} \int d^2B d^2x d^2b T_1(\mathbf{B}) e^{-i\mathbf{k}\cdot(\mathbf{x}-\mathbf{b})} \left(2i \frac{\mathbf{k}}{k^2} \cdot \frac{\mathbf{x}-\mathbf{b}}{|\mathbf{x}-\mathbf{b}|^2} - \ln \frac{1}{|\mathbf{x}-\mathbf{b}|\Lambda} \right) \\
&\quad \times N_G(\mathbf{x}, \mathbf{b}, y) \\
&= \frac{\alpha_s C_F}{2\pi^3} \int d^2B d^2r d^2b T_1(\mathbf{B}) e^{-i\mathbf{k}\cdot\mathbf{r}} \left(2i \frac{\mathbf{k}}{k^2} \cdot \frac{\mathbf{r}}{r^2} - \ln \frac{1}{|\mathbf{r}|\Lambda} \right) \\
&\quad \times N_G(\mathbf{b} + \mathbf{r}, \mathbf{b}, y). \tag{3.43}
\end{aligned}$$

Next, since the whole expression is zero when $\mathbf{r} = 0$, we use

$$\nabla_{\mathbf{r}}^2 \left(e^{-i\mathbf{k}\cdot\mathbf{r}} \ln \frac{1}{|\mathbf{r}|\Lambda} \right) = e^{-i\mathbf{k}\cdot\mathbf{r}} \left(2i \frac{\mathbf{k}}{k^2} \cdot \frac{\mathbf{r}}{r^2} - \ln \frac{1}{|\mathbf{r}|\Lambda} \right) \tag{3.44}$$

to write the equation as

$$\frac{d\sigma}{d^2k dy} = \frac{\alpha_s C_F}{2\pi^3} \frac{1}{k^2} \int d^2B d^2r d^2b T_1(\mathbf{B}) N_G(\mathbf{b} + \mathbf{r}, \mathbf{b}, y) \nabla_{\mathbf{r}}^2 \left(e^{-i\mathbf{k}\cdot\mathbf{r}} \ln \frac{1}{|\mathbf{r}|\Lambda} \right).$$

Using integration by parts, we have $\nabla_{\mathbf{r}}^2$ go from acting on the term in parentheses to acting on the gluon dipole forward scattering amplitude. Then using the following substitution

$$\ln \frac{1}{|\mathbf{r}|\Lambda} = \nabla_{\mathbf{r}}^2 \left(\frac{1}{4} r^2 \ln \frac{1}{|\mathbf{r}|\Lambda} \right)$$

the equation becomes

$$\begin{aligned} \frac{d\sigma}{d^2k dy} &= \frac{\alpha_s C_F}{(2\pi)^3} \frac{1}{\mathbf{k}^2} \int d^2B d^2x d^2y e^{-i\mathbf{k}\cdot\mathbf{r}} (\nabla_{\mathbf{r}}^2 N_G(\mathbf{b} + \mathbf{r}, \mathbf{b}, y)) \\ &\quad \times \left(\nabla_{\mathbf{r}}^2 \left(\frac{1}{4} \mathbf{r}^2 \ln \frac{1}{|\mathbf{r}| \Lambda} T_1(\mathbf{B}) \right) \right). \end{aligned} \quad (3.45)$$

Now we introduce $n_G(\mathbf{b} + \mathbf{r}, \mathbf{b}, y)$, which is the gluon dipole scattering amplitude on the projectile evaluated without saturation effects (no multiple rescatterings, only linear BFKL evolution). The two gluons in the dipole are located at transverse positions $\mathbf{b} + \mathbf{r}$ and \mathbf{b} , and the rapidity interval for the scattering is y . In the quasi-classical limit one has

$$n_G(\mathbf{b} + \mathbf{r}, \mathbf{b}, y = 0) = \pi \alpha_s^2 r_{\perp}^2 \ln \left(\frac{1}{|\mathbf{r}| \Lambda} \right) T_1(\mathbf{b}). \quad (3.46)$$

The single-gluon production cross section can be written in terms of gluon dipole scattering amplitudes. Plugging this into equation 3.45 we arrive at

$$\begin{aligned} \frac{d\sigma}{d^2k dy} &= \frac{C_F}{\alpha_s \pi (2\pi)^3} \frac{1}{\mathbf{k}^2} \int d^2B d^2r d^2b e^{-i\mathbf{k}\cdot\mathbf{r}} (\nabla_{\mathbf{r}}^2 N_G(\mathbf{b} + \mathbf{r}, \mathbf{b}, y)) \\ &\quad \times (\nabla_{\mathbf{r}}^2 n_G(\mathbf{B} + \mathbf{r}, \mathbf{B}, y = 0)). \end{aligned} \quad (3.47)$$

In order to get this into the form we want we need to introduce two new dummy variables, transverse coordinate \mathbf{r}' and transverse momentum \mathbf{q} . Doing this by using the formula

$$\begin{aligned} f(\mathbf{r})g(\mathbf{r}) &= \int d^2r' \delta(\mathbf{r} - \mathbf{r}') f(\mathbf{r})g(\mathbf{r}') \\ &= \int \frac{d^2q}{(2\pi)^2} \int d^2r' e^{-i\mathbf{q}\cdot(\mathbf{r}' - \mathbf{r})} f(\mathbf{r})g(\mathbf{r}') \end{aligned}$$

we have

$$\begin{aligned} \frac{d\sigma}{d^2k dy} &= \frac{C_F}{\alpha_s \pi (2\pi)^3} \frac{1}{\mathbf{k}^2} \int \frac{d^2q}{(2\pi)^2} \int d^2B d^2r' e^{-i\mathbf{r}'\cdot\mathbf{q}} \nabla_{\mathbf{r}'}^2 n_G(\mathbf{B} + \mathbf{r}', \mathbf{B}, y = 0) \\ &\quad \times \int d^2b d^2r e^{-i\mathbf{r}\cdot(\mathbf{k} - \mathbf{q})} \nabla_{\mathbf{r}}^2 N_G(\mathbf{b} + \mathbf{r}, \mathbf{b}, y). \end{aligned} \quad (3.48)$$

It turns out that this is a convolution of two different unintegrated gluon distributions, one for the light ion and one for the heavy ion.

The unintegrated gluon distribution for the light ion is

$$\langle \phi_{A_1}(\mathbf{q}, y) \rangle_{A_1} = \frac{C_F}{\alpha_s (2\pi)^3} \int d^2b d^2r e^{-i\mathbf{q}\cdot\mathbf{r}} \nabla_{\mathbf{r}}^2 n_G(\mathbf{b} + \mathbf{r}, \mathbf{b}, y) \quad (3.49)$$

and the unintegrated gluon distribution for the heavy ion is defined as

$$\langle \phi_{A_2}(\mathbf{q}, y) \rangle_{A_2} = \frac{C_F}{\alpha_s (2\pi)^3} \int d^2b d^2r e^{-i\mathbf{q}\cdot\mathbf{r}} \nabla_{\mathbf{r}}^2 N_G(\mathbf{b} + \mathbf{r}, \mathbf{b}, y). \quad (3.50)$$

The angle brackets $\langle \dots \rangle_{A_1}$ and $\langle \dots \rangle_{A_2}$ denote averaging in the projectile and target wave functions respectively.

The cross section for the production of a single gluon in a pA collision, calculated in the quasi-classical and/or leading- $\ln 1/x$ approximations, can be written as a convolution of these two different unintegrated gluon distributions [80],

$$\frac{d\sigma_g}{d^2k dy} = \frac{2\alpha_s}{C_F} \frac{1}{\mathbf{k}^2} \int d^2q \langle \phi_{A_1}(\mathbf{q}, Y - y) \rangle_{A_1} \langle \phi_{A_2}(\mathbf{k} - \mathbf{q}, y) \rangle_{A_2} \quad (3.51)$$

where we replaced the proton by the light ion A_1 . This substitution implies that no saturation effects are included in the light ion wave function, which makes it equivalent to a proton for the purpose of the single-gluon production calculation. The angle brackets $\langle \dots \rangle_{A_1}$ and $\langle \dots \rangle_{A_2}$ denote averaging in the projectile and target wave functions respectively.

3.5 Summary

In this section we reviewed single-gluon production in the heavy-light ion regime. This served as a pedagogical overview of how the saturation formalism can be applied to gluon production in heavy-light ion collisions. The quarks and gluons originating

from the light ion were found to interact with the the target ion as if it were an instantaneous shock wave. From here we were able to derive the cross section associated with single-gluon production and then were able to write this cross section in a factorized form. With the derivations presented here in mind we can now extend the formalism used here to the more complicated case of two-gluon production.

Chapter 4: Calculation of the two-gluon correlation function

In this chapter, we derive the two-gluon correlation function to leading-order in saturation in the heavy-light ion regime. Here we derive the two-gluon production cross section (the single-gluon production cross section is given in 3.29) and use this result to analyze the azimuthal angular dependence of the correlation function. This chapter borrows heavily from the work in [6].

4.1 Two-gluon production cross section

In this section we are going to calculate the two-gluon production cross section for the heavy–light ion collisions in the saturation/CGC framework. As described in Sec. 2.2 we assume that $A_2 \gg A_1 \gg 1$, such that the saturation effects are resummed to all orders only in the target nucleus with atomic number A_2 . While the saturation effects are not very important in the projectile nucleus with the atomic number A_1 , the fact that $A_1 \gg 1$ implies that the two gluons are predominantly produced in collisions of different nucleons in the projectile nucleus with the target nucleus.

Here we follow the same procedure used for the single-gluon production case Sec. 3.2 calculation.

4.1.1 Amplitudes of the two-gluon production process

The first step in calculating the two-gluon production cross section is calculating the amplitudes involved. There are two distinct types of amplitudes involved in this process. The most obvious one is when the two gluons are emitted from different nucleons originating from the projectile,

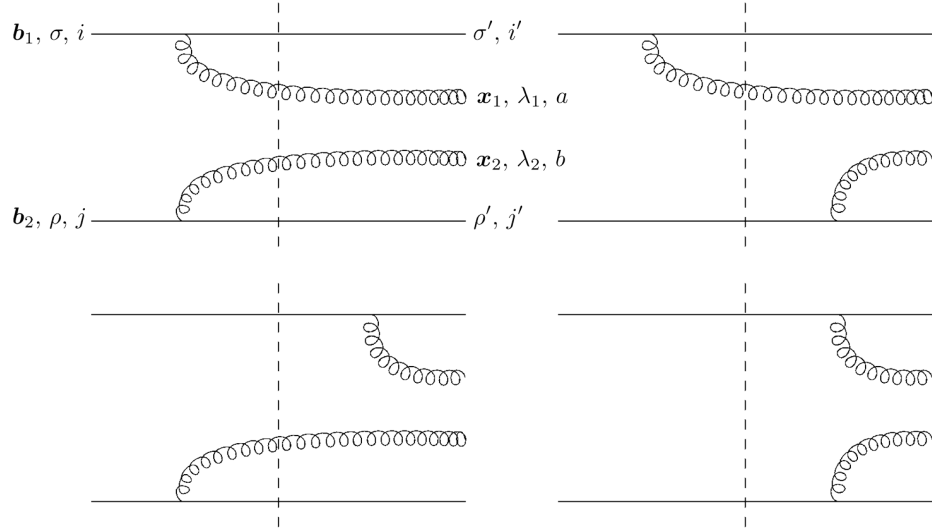


Figure 4.1: B diagrams. These are the diagrams associated with the gluon emission process where two gluons are emitted from different nucleons in the amplitude. The shock wave is represented by a dashed line.

The contributing diagrams for the case where the two observed gluons are emitted from different nucleons is shown in figure 4.1. As one might expect, these diagrams are very similar to the diagrams seen in the pA case derived in the previous section and in fact we really just have the amplitude of the pA case twice! In other words we can write this amplitude, which we call B , using the pA result, 3.24, as

$$B = A_{\sigma'\sigma,\lambda_1}^{a,i'i}(\mathbf{x}_1, \mathbf{b}_1) A_{\rho'\rho,\lambda_2}^{b,j'j}(\mathbf{x}_2, \mathbf{b}_2). \quad (4.1)$$

Where the color indices, quark spins, gluon polarizations and transverse coordinates are defined in figure 4.1.

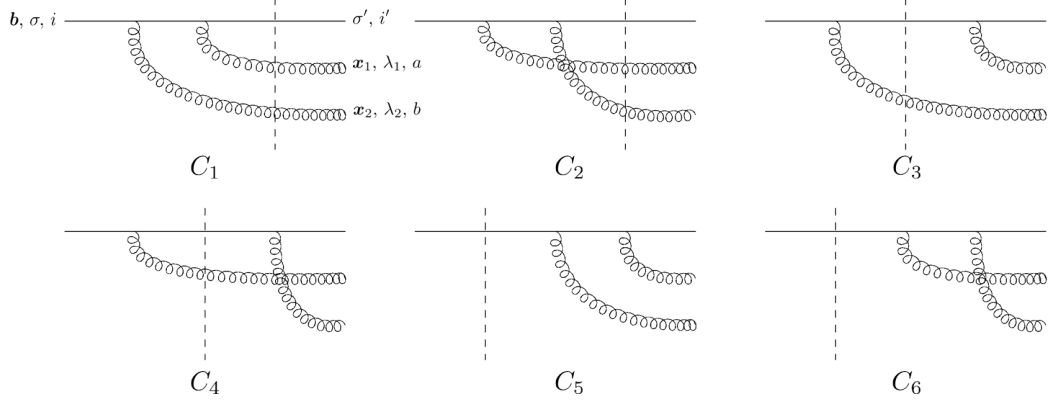


Figure 4.2: C diagrams. One of the nucleons in the projectile emits both of the observed gluons. Once again the shock wave is represented by a dashed line.

The other class of diagrams is where one nucleon emits the two observed gluons. This, at first, seems to be suppressed by an order of saturation scale, however the two gluons end up being connected to the other projectile nucleon once we square the amplitude, keeping it to leading-order. Unlike the B amplitude case we cannot simply use the pA result to derive this result, we are required to calculate these diagrams explicitly. As an example, we calculate diagrams C_1 and C_2 .

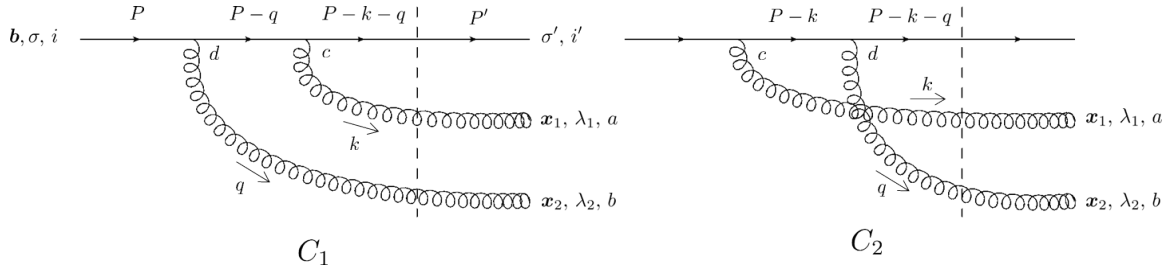


Figure 4.3: Diagrams C_1 and C_2 . The difference between the two diagrams is the ordering of gluon emissions that happen before the shock wave, represented by a dashed line. The sum of these two diagrams combine into a compact result.

The procedure to calculate diagrams C_1 and C_2 is very similar to the one used for the pA case. Using the results from last time, we know that the starting and ending points of the shock wave (in the x^+ direction) are unimportant to the order of interest. Thus this dependence is neglected which means it is not included in the Wilson lines and the integrals over the momenta k^- and q^- are no longer Fourier transforms. The main difference comes from how we treat the color factors. It is easiest at this point to remember that at the end of the day the amplitude must be squared, so there is going to be another fundamental Wilson line, $\left(V_{\mathbf{b}}^\dagger\right)^{ii'}$, from the shock wave interaction on the other side of the cut associated with the projectile quark. We include this term while summing over the colors of the projectile quark to simplify the final result. The expression that needs to be evaluated is

$$\begin{aligned}
& \left(V_{\mathbf{b}}^\dagger\right)^{ii'} (C_1 + C_2) \\
&= \int \frac{dk^-}{2\pi} \frac{d^2k}{(2\pi)^2} e^{i\mathbf{k}\cdot(\mathbf{x}_1-\mathbf{b})} \frac{-i}{k^2+i\epsilon} \left(g_{\mu\alpha} - \frac{\eta_\mu k_\alpha + \eta_\alpha k_\mu}{k^+} \right) \left(-2k^+ g_\perp^{\mu'\mu} U_{\mathbf{x}_1}^{ac} \right) \epsilon_{\lambda_1, \mu'}^* \\
&\times \int \frac{dq^-}{2\pi} \frac{d^2q}{(2\pi)^2} e^{i\mathbf{q}\cdot(\mathbf{x}_2-\mathbf{b})} \frac{-i}{q^2+i\epsilon} \left(g_{\nu\beta} - \frac{\eta_\nu q_\beta + \eta_\beta q_\nu}{q^+} \right) \left(-2q^+ g_\perp^{\nu'\nu} U_{\mathbf{x}_2}^{bd} \right) \epsilon_{\lambda_2, \nu'}^* \\
&\times \frac{1}{2P^+} \left(V_{\mathbf{b}}^\dagger\right)^{ii'} \bar{u}_{\sigma'}(P') \gamma^+ V_{\mathbf{b}}^{i'i'''} \frac{i(\not{P} - \not{k} - \not{q})}{(P-k-q)^2+i\epsilon} \left[ig \gamma^\alpha (t^c)^{i''i'''} \frac{i(\not{P} - \not{q})}{(P-q)^2+i\epsilon} ig \gamma^\beta (t^d)^{i''i} \right. \\
&\quad \left. + ig \gamma^\beta (t^d)^{i''i'''} \frac{i(\not{P} - \not{k})}{(P-k)^2+i\epsilon} ig \gamma^\alpha (t^c)^{i''i} \right] u_\sigma(P). \tag{4.2}
\end{aligned}$$

The first step is analyzing the quark line while taking into account the various Wilson lines and generators associated with it. Using the eikonal limit and evaluating the color object the expression simplifies quite nicely.

$$\begin{aligned}
& \frac{1}{2P^+} \left(V_{\mathbf{b}}^\dagger\right)^{ii'} \bar{u}_{\sigma'}(P') \cdots u_\sigma(P) \\
&\approx \frac{-g^2}{2} \delta^{cd} g^{-\alpha} g^{-\beta} \frac{1}{2P^+} \bar{u}_{\sigma'}(P') \gamma^+ \frac{-i\gamma^- P^+}{2P^+(k^-+q^-)-i\epsilon} \gamma^+ \\
&\times \left[\frac{-i\gamma^- P^+}{2P^+q^- - i\epsilon} + \frac{-i\gamma^- P^+}{2P^+k^- - i\epsilon} \right] \gamma^+ u_\sigma(P) \\
&= \frac{g^2}{2} \delta^{cd} g^{-\alpha} g^{-\beta} \frac{1}{2P^+} \bar{u}_{\sigma'}(P') \gamma^+ u_\sigma(P) \frac{1}{k^-+q^- - i\epsilon} \left[\frac{1}{q^- - i\epsilon} + \frac{1}{k^- - i\epsilon} \right] \\
&= \frac{g^2}{2} \delta_{\sigma'\sigma} \delta^{cd} g^{-\alpha} g^{-\beta} \frac{1}{k^- - i\epsilon} \frac{1}{q^- - i\epsilon}. \tag{4.3}
\end{aligned}$$

At this point it should be clear why we included the $\left(V_{\mathbf{b}}^\dagger\right)^{ii'}$ term. This allowed us to notice that, despite each fundamental generator being associated with a different observed gluon, the color factor for both diagrams ends up being the same, which allowed us to combine the denominators associated with the eikonal quarks in a convenient manner.

Plugging this term back into the main expression we arrive at

$$\begin{aligned}
\left(V_{\mathbf{b}}^\dagger\right)^{ii'} (C_1 + C_2) &= 2g^2 \delta_{\sigma'\sigma} \delta^{cd} \int \frac{dk^-}{2\pi} \frac{d^2k}{(2\pi)^2} e^{i\mathbf{k}\cdot(\mathbf{x}_1-\mathbf{b})} \frac{i}{k^- - i\epsilon} \frac{\boldsymbol{\epsilon}_{\lambda_1}^* \cdot \mathbf{k}}{2k^+k^- - \mathbf{k}^2 + i\epsilon} U_{\mathbf{x}}^{ac} \\
&\times \int \frac{dq^-}{2\pi} \frac{d^2q}{(2\pi)^2} e^{i\mathbf{q}\cdot(\mathbf{x}_2-\mathbf{b})} \frac{i}{q^- - i\epsilon} \frac{\boldsymbol{\epsilon}_{\lambda_2}^* \cdot \mathbf{q}}{2q^+q^- - \mathbf{q}^2 + i\epsilon} U_{\mathbf{y}}^{bd}
\end{aligned} \quad (4.4)$$

which is very similar to the result we got for the pA case, 3.19. Using that result we arrive at

$$\left(V_{\mathbf{b}}^\dagger\right)^{ii'} (C_1 + C_2) = -\frac{g^2}{\pi^2} \delta_{\sigma'\sigma} \frac{\boldsymbol{\epsilon}_{\lambda_1}^* \cdot (\mathbf{x}_1 - \mathbf{b})}{|\mathbf{x}_1 - \mathbf{b}|^2} \frac{\boldsymbol{\epsilon}_{\lambda_2}^* \cdot (\mathbf{x}_2 - \mathbf{b})}{|\mathbf{x}_2 - \mathbf{b}|^2} [U_{\mathbf{x}_1} U_{\mathbf{x}_2}^\dagger]^{ab}. \quad (4.5)$$

The other diagrams can be evaluated in a manner similar to this and the pA case. The final result for each of the C diagrams, now including the averaging of the quark colors and the summing and averaging over the spins, is

$$\frac{1}{2N_c} \sum_{\sigma',\sigma} \left(V_{\mathbf{b}}^\dagger\right)^{ii'} (C_1 + C_2) = -\frac{g^2}{2N_c \pi^2} \frac{\boldsymbol{\epsilon}_{\lambda_1}^* \cdot (\mathbf{x}_1 - \mathbf{b})}{|\mathbf{x}_1 - \mathbf{b}|^2} \frac{\boldsymbol{\epsilon}_{\lambda_2}^* \cdot (\mathbf{x}_2 - \mathbf{b})}{|\mathbf{x}_2 - \mathbf{b}|^2} [U_{\mathbf{x}_1} U_{\mathbf{x}_2}^\dagger]^{ab} \quad (4.6a)$$

$$\frac{1}{2N_c} \sum_{\sigma',\sigma} \left(V_{\mathbf{b}}^\dagger\right)^{ii'} C_3 = \frac{g^2}{2N_c \pi^2} \frac{\boldsymbol{\epsilon}_{\lambda_1}^* \cdot (\mathbf{x}_1 - \mathbf{b})}{|\mathbf{x}_1 - \mathbf{b}|^2} \frac{\boldsymbol{\epsilon}_{\lambda_2}^* \cdot (\mathbf{x}_2 - \mathbf{b})}{|\mathbf{x}_2 - \mathbf{b}|^2} [U_{\mathbf{b}} U_{\mathbf{x}_2}^\dagger]^{ab} \quad (4.6b)$$

$$\frac{1}{2N_c} \sum_{\sigma',\sigma} \left(V_{\mathbf{b}}^\dagger\right)^{ii'} C_4 = \frac{g^2}{2N_c \pi^2} \frac{\boldsymbol{\epsilon}_{\lambda_1}^* \cdot (\mathbf{x}_1 - \mathbf{b})}{|\mathbf{x}_1 - \mathbf{b}|^2} \frac{\boldsymbol{\epsilon}_{\lambda_2}^* \cdot (\mathbf{x}_2 - \mathbf{b})}{|\mathbf{x}_2 - \mathbf{b}|^2} [U_{\mathbf{x}_1} U_{\mathbf{b}}^\dagger]^{ab} \quad (4.6c)$$

$$\frac{1}{2N_c} \sum_{\sigma',\sigma} \left(V_{\mathbf{b}}^\dagger\right)^{ii'} (C_5 + C_6) = -\frac{g^2}{2N_c \pi^2} \frac{\boldsymbol{\epsilon}_{\lambda_1}^* \cdot (\mathbf{x}_1 - \mathbf{b})}{|\mathbf{x}_1 - \mathbf{b}|^2} \frac{\boldsymbol{\epsilon}_{\lambda_2}^* \cdot (\mathbf{x}_2 - \mathbf{b})}{|\mathbf{x}_2 - \mathbf{b}|^2} [U_{\mathbf{b}} U_{\mathbf{b}}^\dagger]^{ab} \quad (4.6d)$$

At this point we define the following function

$$C_{\lambda_1 \lambda_2}^{ab}(\mathbf{x}_1, \mathbf{x}_2, \mathbf{b}) = \frac{1}{2N_c} \sum_{\sigma',\sigma} \left(V_{\mathbf{b}}^\dagger\right)^{ii'} \sum_{j=1}^6 C_j. \quad (4.7)$$

This is not quite an amplitude, due to the fact we have already considered the other side of the cut when evaluating the diagrams, but it can be used in a similar manner when calculating the cross section. Evaluating the expression gives the final result for the C diagrams

$$C_{\lambda_1 \lambda_2}^{ab}(\mathbf{x}_1, \mathbf{x}_2, \mathbf{b}) = -\frac{g^2}{2N_c \pi^2} \frac{\boldsymbol{\epsilon}_{\lambda_1}^* \cdot (\mathbf{x}_1 - \mathbf{b})}{|\mathbf{x}_1 - \mathbf{b}|^2} \frac{\boldsymbol{\epsilon}_{\lambda_2}^* \cdot (\mathbf{x}_2 - \mathbf{b})}{|\mathbf{x}_2 - \mathbf{b}|^2} \left[(U_{\mathbf{x}_1} - U_{\mathbf{b}}) (U_{\mathbf{x}_2}^\dagger - U_{\mathbf{b}}^\dagger) \right]^{ab}. \quad (4.8)$$

At this point we have the results necessary to calculate the two-gluon production cross section for the two-nucleon process. There are numerous ways these amplitudes can combine so it is necessary to split the cross section into two parts: the “square terms”, where a gluon is emitted by the same quark on both sides of the cut; and the “crossed terms”, where a gluon is emitted by different quarks on either side of the cut.

4.1.2 Two-gluon production with long-range rapidity correlations: “square” of the single gluon production

The two-gluon production cross section in heavy–light ion collisions is easily constructed by analogy to the single-gluon production calculation of Sec. 3.2. The diagrams contributing to the square of the scattering amplitude for the double gluon production in heavy–light ion collisions are shown in Fig. 4.4, written as a direct product of the gluon production processes in the interactions of each of the nucleons from the projectile nucleus with the target. Just as in Fig. 3.6 the vertical dashed lines in Fig. 4.4 represent interactions with the target, while the vertical solid line denotes the final state cut.

The evaluation of the diagrams in Fig. 4.4 is straightforward. We follow the same process as we did in the single-gluon production case, 3.25. Multiplying the amplitude 4.1 by the corresponding complex conjugated amplitude (making sure the coordinates and spin are contracted in the way that corresponds to the kinematics laid out in Fig. 4.4), the spins and colors of both quarks are summed and averaged over. The gluon polarizations are summed over and a Fourier transform over the transverse positions of the gluon at the cut is preformed, leaving the final expression in transverse momentum space. This is then convoluted with the nuclear profile

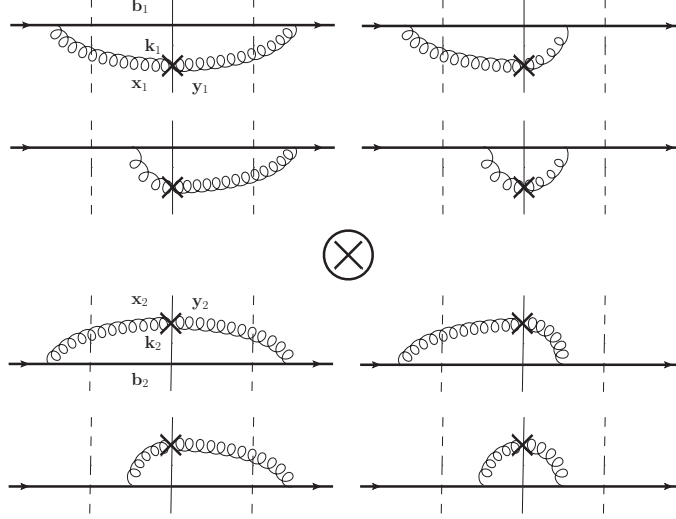


Figure 4.4: Diagrams contributing to the two-gluon production cross section in the heavy-light ion collision. For clarity the diagrams are shown as a direct product of gluon production processes in collisions of the two interacting nucleons from the projectile nucleus with the target nucleus.

functions, resulting in

$$\begin{aligned}
\frac{d\sigma_{square}}{d^2k_1 dy_1 d^2k_2 dy_2} &= \frac{1}{[2(2\pi)^3]^2} \int d^2B d^2b_1 d^2b_2 T_1(\mathbf{B} - \mathbf{b}_1) T_1(\mathbf{B} - \mathbf{b}_2) \\
&\times \int d^2x_1 d^2y_1 d^2x_2 d^2y_2 e^{-i\mathbf{k}_1 \cdot (\mathbf{x}_1 - \mathbf{y}_1) - i\mathbf{k}_2 \cdot (\mathbf{x}_2 - \mathbf{y}_2)} \frac{1}{4N_c^2} \sum_{\sigma' \sigma, \rho' \rho} \sum_{\lambda_1, \lambda_2} \\
&\times \left\langle \left(A_{\sigma' \sigma, \lambda_1}^{a, i' i}(\mathbf{y}_1, \mathbf{b}_1) A_{\rho' \rho, \lambda_2}^{b, j' j}(\mathbf{y}_2, \mathbf{b}_2) \right)^\dagger A_{\sigma' \sigma, \lambda_1}^{a, i' i}(\mathbf{x}_1, \mathbf{b}_1) A_{\rho' \rho, \lambda_2}^{b, j' j}(\mathbf{x}_2, \mathbf{b}_2) \right\rangle. \quad (4.9)
\end{aligned}$$

Using the previous result for the single-gluon case, 3.26, we can easily evaluate the amplitude squared term (where we have included all averaging and summations required),

$$\begin{aligned}
& \frac{1}{4N_c^2} \sum_{\sigma'\sigma,\rho'\rho} \sum_{\lambda_1,\lambda_2} \left\langle \left(A_{\sigma'\sigma,\lambda_1}^{a,i'i}(\mathbf{y}_1, \mathbf{b}_1) A_{\rho'\rho,\lambda_2}^{b,j'j}(\mathbf{y}_2, \mathbf{b}_2) \right)^\dagger A_{\sigma'\sigma,\lambda_1}^{a,i'i}(\mathbf{x}_1, \mathbf{b}_1) A_{\rho'\rho,\lambda_2}^{b,j'j}(\mathbf{x}_2, \mathbf{b}_2) \right\rangle \\
&= \frac{g^4}{4N_c^2 \pi^4} \frac{(\mathbf{x}_1 - \mathbf{b}_1) \cdot (\mathbf{y}_1 - \mathbf{b}_1) (\mathbf{x}_2 - \mathbf{b}_2) \cdot (\mathbf{y}_2 - \mathbf{b}_2)}{|\mathbf{x}_1 - \mathbf{b}_1|^2 |\mathbf{y}_2 - \mathbf{b}_2|^2 |\mathbf{x}_2 - \mathbf{b}_2|^2 |\mathbf{y}_2 - \mathbf{b}_2|^2} \\
&\quad \times \left\langle Tr \left[(U_{\mathbf{x}_1} - U_{\mathbf{b}_1}) \left(U_{\mathbf{y}_1}^\dagger - U_{\mathbf{b}_1}^\dagger \right) \right] Tr \left[(U_{\mathbf{x}_2} - U_{\mathbf{b}_2}) \left(U_{\mathbf{y}_2}^\dagger - U_{\mathbf{b}_2}^\dagger \right) \right] \right\rangle. \quad (4.10)
\end{aligned}$$

This is nearly identical to the amplitude due to two independently generated single-gluon emissions, 3.26 for two different gluons if you will. Due to the target averaging of the Wilson lines they are not exactly identical, meaning that any dynamically generated correlations are generated through the interaction with the target.

The full ‘‘square’’ contribution is recovered by inserting 4.10 into 4.9, resulting in (cf. [60])

$$\begin{aligned}
\frac{d\sigma_{square}}{d^2k_1 dy_1 d^2k_2 dy_2} &= \frac{\alpha_s^2 C_F^2}{16 \pi^8} \int d^2B d^2b_1 d^2b_2 T_1(\mathbf{B} - \mathbf{b}_1) T_1(\mathbf{B} - \mathbf{b}_2) d^2x_1 d^2y_1 d^2x_2 d^2y_2 \\
&\times e^{-i \mathbf{k}_1 \cdot (\mathbf{x}_1 - \mathbf{y}_1) - i \mathbf{k}_2 \cdot (\mathbf{x}_2 - \mathbf{y}_2)} \frac{\mathbf{x}_1 - \mathbf{b}_1}{|\mathbf{x}_1 - \mathbf{b}_1|^2} \cdot \frac{\mathbf{y}_1 - \mathbf{b}_1}{|\mathbf{y}_1 - \mathbf{b}_1|^2} \frac{\mathbf{x}_2 - \mathbf{b}_2}{|\mathbf{x}_2 - \mathbf{b}_2|^2} \cdot \frac{\mathbf{y}_2 - \mathbf{b}_2}{|\mathbf{y}_2 - \mathbf{b}_2|^2} \\
&\times \left\langle \left(\frac{1}{N_c^2 - 1} Tr[U_{\mathbf{x}_1} U_{\mathbf{y}_1}^\dagger] - \frac{1}{N_c^2 - 1} Tr[U_{\mathbf{x}_1} U_{\mathbf{b}_1}^\dagger] - \frac{1}{N_c^2 - 1} Tr[U_{\mathbf{b}_1} U_{\mathbf{y}_1}^\dagger] + 1 \right) \right. \\
&\times \left. \left(\frac{1}{N_c^2 - 1} Tr[U_{\mathbf{x}_2} U_{\mathbf{y}_2}^\dagger] - \frac{1}{N_c^2 - 1} Tr[U_{\mathbf{x}_2} U_{\mathbf{b}_2}^\dagger] - \frac{1}{N_c^2 - 1} Tr[U_{\mathbf{b}_2} U_{\mathbf{y}_2}^\dagger] + 1 \right) \right\rangle. \quad (4.11)
\end{aligned}$$

This is the expression for the two-gluon production cross section coming from the diagrams in Fig. 4.4. The interaction with the target can be evaluated in the quasi-classical multiple rescattering approximation, as we will show later. The rapidity evolution can be included using the JIMWLK equation. Note, however, that when the rapidity difference between the two gluons is sufficiently large, $|y_1 - y_2| \gtrsim 1/\alpha_s$, one has to include the evolution corrections in the rapidity interval between the produced gluons, such that the Wilson lines in the two parentheses in 4.11 should be taken at different rapidities. A similar effect was included in the two-gluon production cross section in DIS in [84]. In such a regime, one would also need to include

evolution corrections in the rapidity window between the projectile and (at least one of) the produced gluons. Inclusion of the evolution corrections in terms of the weight functional W of the JIMWLK evolution equation into the two-gluon production cross section in nucleus–nucleus collisions was done in [47]. In this chapter we will limit ourselves to the quasi-classical regime where no evolution corrections are required and the cross sections are rapidity-independent.

Note that for scattering on a large nuclear target, if one resums powers of $\alpha_s^2 A^{1/3}$, as is the case in the Glauber-Mueller (GM) rescatterings (and in the BK/JIMWLK evolution for which the GM rescatterings serve as the initial condition), and if one takes the large- N_c limit, the expectation values of the traces in 4.11 factorize, such that

$$\langle \text{Tr}[U_{\mathbf{x}_1} U_{\mathbf{y}_1}^\dagger] \text{Tr}[U_{\mathbf{x}_2} U_{\mathbf{y}_2}^\dagger] \rangle \Big|_{\text{large-}N_c, \text{large-}A_2} \approx \langle \text{Tr}[U_{\mathbf{x}_1} U_{\mathbf{y}_1}^\dagger] \rangle \langle \text{Tr}[U_{\mathbf{x}_2} U_{\mathbf{y}_2}^\dagger] \rangle. \quad (4.12)$$

This leads to factorization of 2.26 being valid in the large- N_c and large-target-nucleus limit. As shown above, even in this factorized regime one may obtain a non-trivial correlation function due to the geometric correlations.

4.1.3 Two-gluon production with long-range rapidity correlations: “crossed” diagrams

Before we proceed to evaluating the correlations contained in the cross section 4.11, let us point out another contribution to the two-gluon production cross section arising from squaring the sum of the diagrams in Fig. 4.1. When squaring the diagrams in Fig. 4.1 it is possible that the gluon emitted by one nucleon in the amplitude will be absorbed by another nucleon in the complex conjugate amplitude, as shown in Fig. 4.5. We also have the contribution from the diagrams in Fig. 4.2 being contracted with

diagrams where both gluons are emitted from the other nucleon, shown in Fig. 4.6. We will refer to these diagrams as the “crossed” graphs (it should be noted that in these diagrams crossing gluon lines do not form a vertex). The diagrams obtained by a mirror reflection with respect to the cut of those in Figs. 4.5 and 4.6 correspond to the $\mathbf{b}_1 \leftrightarrow \mathbf{b}_2$ interchange, and will be automatically included in the cross section to be calculated below since it will contain integrals over all \mathbf{b}_1 and \mathbf{b}_2 .

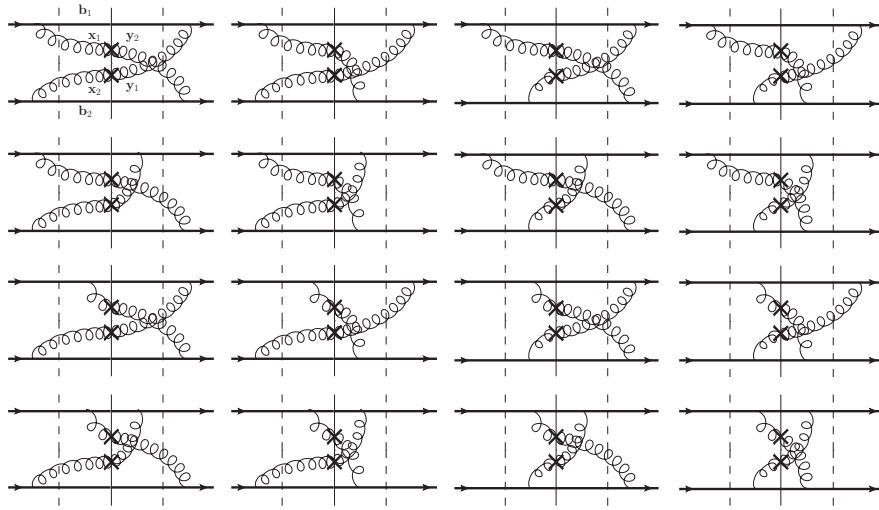


Figure 4.5: Diagrams contributing to the two-gluon production cross section, with the gluon emitted by each nucleon in the amplitude absorbed by another nucleon in the complex conjugate amplitude. The top cross denotes the gluon with momentum \mathbf{k}_1 , while the bottom one denotes the gluon with momentum \mathbf{k}_2 .

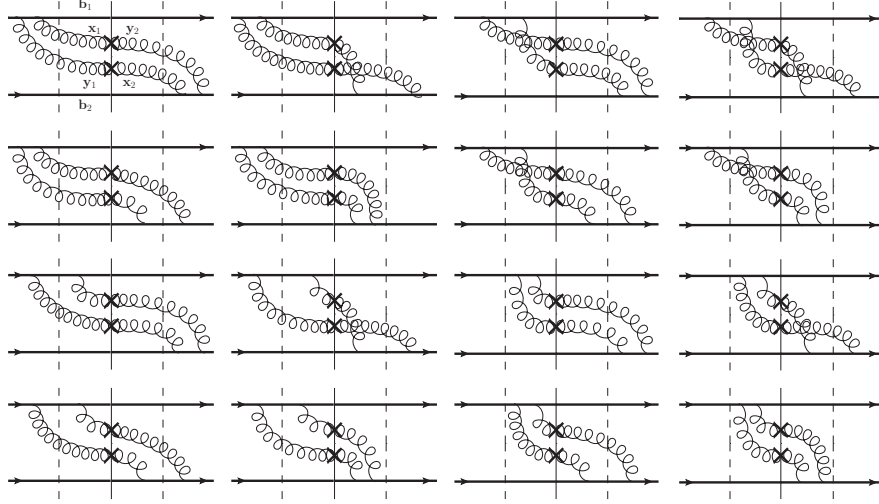


Figure 4.6: Another set of diagrams contributing to the two-gluon production cross section, with the gluon emitted by each nucleon in the amplitude absorbed by another nucleon in the complex conjugate amplitude. Again the top cross denotes the gluon with momentum \mathbf{k}_1 , while the bottom one denotes the gluon with momentum \mathbf{k}_2 .

The longitudinal momentum flow patterns in Figs. 4.5 and 4.6 are different from that in Fig. 4.4. This is illustrated in Fig. 4.7, which shows the flow of the “plus” momentum component through the first diagram in Fig. 4.5. Note that the change in the “plus” momentum component is negligible in the eikonal interactions with the target considered here. Requiring that the incoming quark lines carry the same “plus” momentum both in the amplitude and in the complex conjugate amplitude, one would obtain $k_1^+ = k_2^+$; however, such requirement is not correct. The actual scattering happens between two nuclei, and it is the momenta of the whole incoming nuclei which have to be equal both in the amplitude and in the complex conjugate amplitude. Hence for $k_1^+ \neq k_2^+$ the diagrams like that in Fig. 4.7 would only correspond to different redistributions of the projectile nucleus momentum between the nucleons in it in the amplitude and in the complex conjugate amplitude without changing the

same “plus” momentum of the whole nucleus on both sides of the cut. Hence the $k_1^+ = k_2^+$ condition is not necessary for the “crossed” diagrams.

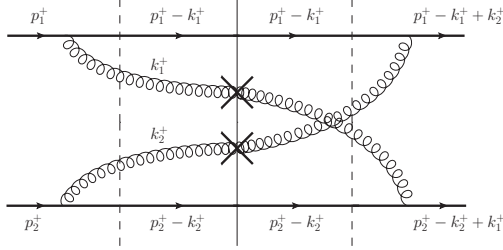


Figure 4.7: The flow of the “plus” momentum component through the first diagram in Fig. 4.5.

The process used here to calculate the cross section is similar to the “square” diagram case, with the extra complication that we have two sets of diagrams that need to be considered. To take in to account the terms shown in Fig. 4.5, we use the same process used in deriving 4.9 except the coordinates and spins of the complex conjugated amplitude are different (corresponds to the kinematics shown in Fig. 4.4). To take into account the terms in Fig. 4.6, we use 4.8, multiply it by its complex conjugate (keeping the coordinates such that it matches the kinematics shown in Fig. 4.6) and sum over the gluons’ polarizations (the quarks’ spins and colors were already taken into account when deriving 4.8). The sum of these two terms is Fourier transformed into transverse momentum space and convoluted with the nuclear profile functions, resulting in

$$\begin{aligned}
\frac{d\sigma_{crossed}}{d^2k_1 dy_1 d^2k_2 dy_2} &= \frac{1}{[2(2\pi)^3]^2} \int d^2B d^2b_1 d^2b_2 T_1(\mathbf{B} - \mathbf{b}_1) T_1(\mathbf{B} - \mathbf{b}_2) \\
&\times d^2x_1 d^2y_1 d^2x_2 d^2y_2 e^{-i\mathbf{k}_1 \cdot (\mathbf{x}_1 - \mathbf{y}_2) - i\mathbf{k}_2 \cdot (\mathbf{x}_2 - \mathbf{y}_1)} \\
&\times \left\langle \frac{1}{4N_c^2} \sum_{\sigma', \rho', \rho} \sum_{\lambda_1, \lambda_2} \left(A_{\sigma'\sigma, \lambda_2}^{a, i' i}(\mathbf{y}_2, \mathbf{b}_1) A_{\rho'\rho, \lambda_1}^{b, j' j}(\mathbf{y}_1, \mathbf{b}_2) \right)^\dagger A_{\sigma'\sigma, \lambda_1}^{a, i' i}(\mathbf{x}_1, \mathbf{b}_1) A_{\rho'\rho, \lambda_2}^{b, j' j}(\mathbf{x}_2, \mathbf{b}_2) \right. \\
&\left. + \sum_{\lambda_1, \lambda_2} \left(C_{\lambda_1 \lambda_2}^{ab}(\mathbf{y}_2, \mathbf{y}_1, \mathbf{b}_2) \right)^\dagger C_{\lambda_1 \lambda_2}^{ab}(\mathbf{x}_1, \mathbf{x}_2, \mathbf{b}_1) \right\rangle \quad (4.13)
\end{aligned}$$

Evaluating the term associated with Fig. 4.5 we find

$$\begin{aligned}
&\frac{1}{4N_c^2} \sum_{\sigma', \rho', \rho} \sum_{\lambda_1, \lambda_2} \left\langle \left(A_{\sigma'\sigma, \lambda_2}^{a, i' i}(\mathbf{y}_1, \mathbf{b}_1) A_{\rho'\rho, \lambda_1}^{b, j' j}(\mathbf{y}_2, \mathbf{b}_2) \right)^\dagger A_{\sigma'\sigma, \lambda_1}^{a, i' i}(\mathbf{x}_1, \mathbf{b}_1) A_{\rho'\rho, \lambda_2}^{b, j' j}(\mathbf{x}_2, \mathbf{b}_2) \right\rangle \\
&= \frac{g^4}{4N_c^2 \pi^4} \sum_{\sigma', \rho', \rho} \delta_{\sigma'\sigma} \delta_{\sigma'\sigma} \delta_{\rho'\rho} \delta_{\rho'\rho} \sum_{\lambda_1} \frac{\boldsymbol{\epsilon}_{\lambda_1}^* \cdot (\mathbf{x}_1 - \mathbf{b}_1)}{|\mathbf{x}_1 - \mathbf{b}_1|^2} \frac{\boldsymbol{\epsilon}_{\lambda_1} \cdot (\mathbf{y}_2 - \mathbf{b}_2)}{|\mathbf{y}_2 - \mathbf{b}_2|^2} \\
&\times \sum_{\lambda_2} \frac{\boldsymbol{\epsilon}_{\lambda_2}^* \cdot (\mathbf{x}_2 - \mathbf{b}_2)}{|\mathbf{x}_2 - \mathbf{b}_2|^2} \frac{\boldsymbol{\epsilon}_{\lambda_2} \cdot (\mathbf{y}_1 - \mathbf{b}_1)}{|\mathbf{y}_1 - \mathbf{b}_1|^2} \left\langle \text{tr}[t^e V_{b_1}^\dagger V_{b_1} t^c] \text{tr}[t^f V_{b_2}^\dagger V_{b_2} t^d] \right. \\
&\times \left[\left(U_{\mathbf{y}_2}^\dagger - U_{\mathbf{b}_2}^\dagger \right) (U_{\mathbf{x}_1} - U_{\mathbf{b}_1}) \right]^{fc} \left[\left(U_{\mathbf{y}_1}^\dagger - U_{\mathbf{b}_1}^\dagger \right) (U_{\mathbf{x}_2} - U_{\mathbf{b}_2}) \right]^{ed} \left. \right\rangle \\
&= \frac{g^4}{4N_c^2 \pi^4} \frac{(\mathbf{x}_1 - \mathbf{b}_1) \cdot (\mathbf{y}_2 - \mathbf{b}_2)}{|\mathbf{x}_1 - \mathbf{b}_1|^2 |\mathbf{y}_2 - \mathbf{b}_2|^2} \frac{(\mathbf{x}_2 - \mathbf{b}_2) \cdot (\mathbf{y}_1 - \mathbf{b}_1)}{|\mathbf{x}_2 - \mathbf{b}_2|^2 |\mathbf{y}_1 - \mathbf{b}_1|^2} \\
&\times \left\langle \text{Tr} \left[(U_{\mathbf{x}_1} - U_{\mathbf{b}_1}) \left(U_{\mathbf{y}_1}^\dagger - U_{\mathbf{b}_1}^\dagger \right) (U_{\mathbf{x}_2} - U_{\mathbf{b}_2}) \left(U_{\mathbf{y}_2}^\dagger - U_{\mathbf{b}_2}^\dagger \right) \right] \right\rangle. \quad (4.14)
\end{aligned}$$

Similarly for the term associated with the Fig. 4.6,

$$\begin{aligned}
&\sum_{\lambda_1, \lambda_2} \left(C_{\lambda_1 \lambda_2}^{ab}(\mathbf{y}_2, \mathbf{y}_1, \mathbf{b}_2) \right)^\dagger C_{\lambda_1 \lambda_2}^{ab}(\mathbf{x}_1, \mathbf{x}_2, \mathbf{b}_1) \\
&= \frac{g^4}{4N_c^2 \pi^4} \sum_{\lambda_1, \lambda_2} \frac{\boldsymbol{\epsilon}_{\lambda_1}^* \cdot (\mathbf{x}_1 - \mathbf{b}_1)}{|\mathbf{x}_1 - \mathbf{b}_1|^2} \frac{\boldsymbol{\epsilon}_{\lambda_1} \cdot (\mathbf{y}_2 - \mathbf{b}_2)}{|\mathbf{y}_2 - \mathbf{b}_2|^2} \frac{\boldsymbol{\epsilon}_{\lambda_2}^* \cdot (\mathbf{x}_2 - \mathbf{b}_1)}{|\mathbf{x}_2 - \mathbf{b}_1|^2} \frac{\boldsymbol{\epsilon}_{\lambda_2} \cdot (\mathbf{y}_1 - \mathbf{b}_2)}{|\mathbf{y}_1 - \mathbf{b}_2|^2} \\
&\times \left\langle \left[(U_{\mathbf{y}_2} - U_{\mathbf{b}_2}) \left(U_{\mathbf{y}_1}^\dagger - U_{\mathbf{b}_2}^\dagger \right) \right]^{ba} \left[(U_{\mathbf{x}_1} - U_{\mathbf{b}_1}) \left(U_{\mathbf{x}_2}^\dagger - U_{\mathbf{b}_1}^\dagger \right) \right]^{ab} \right\rangle \\
&= \frac{g^4}{4N_c^2 \pi^4} \frac{(\mathbf{x}_1 - \mathbf{b}_1) \cdot (\mathbf{y}_2 - \mathbf{b}_2)}{|\mathbf{x}_1 - \mathbf{b}_1|^2 |\mathbf{y}_2 - \mathbf{b}_2|^2} \frac{(\mathbf{x}_2 - \mathbf{b}_1) \cdot (\mathbf{y}_1 - \mathbf{b}_2)}{|\mathbf{x}_2 - \mathbf{b}_1|^2 |\mathbf{y}_1 - \mathbf{b}_2|^2} \\
&\times \left\langle \text{Tr} \left[(U_{\mathbf{x}_1} - U_{\mathbf{b}_1}) \left(U_{\mathbf{x}_2}^\dagger - U_{\mathbf{b}_1}^\dagger \right) (U_{\mathbf{y}_2} - U_{\mathbf{b}_2}) \left(U_{\mathbf{y}_1}^\dagger - U_{\mathbf{b}_2}^\dagger \right) \right] \right\rangle. \quad (4.15)
\end{aligned}$$

Notice this is the same as 4.14 under interchange of $\mathbf{x}_2 \leftrightarrow \mathbf{y}_1$. Since in the total expression 4.13 the transverse coordinates are all dummy variables, we can interchange

$\mathbf{x}_2 \leftrightarrow \mathbf{y}_1$ in 4.15 so that it now is the same as 4.14 except it has different coordinates in the exponential. This means the only difference between the contributions of the diagrams in Figs. 4.5 and 4.6 is in the exponential factors for the Fourier transform into transverse momentum space.

It is convenient to define $Int_{crossed}$ as the target averaged Wilson line object in both 4.15 and 4.15 (normalized by $\frac{1}{N_c^2}$). Defining the color-quadrupole operator [84–88]

$$Q(\mathbf{x}_1, \mathbf{x}_2, \mathbf{x}_3, \mathbf{x}_4) \equiv \frac{1}{N_c^2 - 1} \langle Tr[U_{\mathbf{x}_1} U_{\mathbf{x}_2}^\dagger U_{\mathbf{x}_3} U_{\mathbf{x}_4}^\dagger] \rangle, \quad (4.16)$$

we can express $Int_{crossed}$ as a combination of color-quadrupole operators and adjoint (gluon) dipole S -matrices, 3.28 with the rapidity dependence dropped.

$$\begin{aligned} & Int_{crossed}(\mathbf{x}_1, \mathbf{y}_1, \mathbf{b}_1, \mathbf{x}_2, \mathbf{y}_2, \mathbf{b}_2) \\ & \equiv \frac{1}{N_c^2 - 1} \left\langle Tr \left[(U_{\mathbf{x}_1} - U_{\mathbf{b}_1}) \left(U_{\mathbf{x}_2}^\dagger - U_{\mathbf{b}_1}^\dagger \right) (U_{\mathbf{y}_2} - U_{\mathbf{b}_2}) \left(U_{\mathbf{y}_1}^\dagger - U_{\mathbf{b}_2}^\dagger \right) \right] \right\rangle \\ & = Q(\mathbf{x}_1, \mathbf{y}_1, \mathbf{x}_2, \mathbf{y}_2) - Q(\mathbf{x}_1, \mathbf{y}_1, \mathbf{x}_2, \mathbf{b}_2) - Q(\mathbf{x}_1, \mathbf{y}_1, \mathbf{b}_2, \mathbf{y}_2) + S_G(\mathbf{x}_1, \mathbf{y}_1) \\ & \quad - Q(\mathbf{x}_1, \mathbf{b}_1, \mathbf{x}_2, \mathbf{y}_2) + Q(\mathbf{x}_1, \mathbf{b}_1, \mathbf{x}_2, \mathbf{b}_2) + Q(\mathbf{x}_1, \mathbf{b}_1, \mathbf{b}_2, \mathbf{y}_2) - S_G(\mathbf{x}_1, \mathbf{b}_1) \\ & \quad - Q(\mathbf{b}_1, \mathbf{y}_1, \mathbf{x}_2, \mathbf{y}_2) + Q(\mathbf{b}_1, \mathbf{y}_1, \mathbf{x}_2, \mathbf{b}_2) + Q(\mathbf{b}_1, \mathbf{y}_1, \mathbf{b}_2, \mathbf{y}_2) - S_G(\mathbf{b}_1, \mathbf{y}_1) \\ & \quad + S_G(\mathbf{x}_2, \mathbf{y}_2) - S_G(\mathbf{x}_2, \mathbf{b}_2) - S_G(\mathbf{b}_2, \mathbf{y}_2) + 1. \end{aligned} \quad (4.17)$$

Using 4.14, 4.15, 4.17 and the fact that the transverse coordinates are all dummy variables we arrive at the expression for the two-gluon production cross section contribution resulting from the “crossed” diagrams from Figs. 4.5 and 4.6

$$\begin{aligned}
\frac{d\sigma_{crossed}}{d^2k_1 dy_1 d^2k_2 dy_2} &= \frac{1}{[2(2\pi)^3]^2} \int d^2B d^2b_1 d^2b_2 T_1(\mathbf{B} - \mathbf{b}_1) T_1(\mathbf{B} - \mathbf{b}_2) \\
&\times d^2x_1 d^2y_1 d^2x_2 d^2y_2 \left[e^{-i\mathbf{k}_1 \cdot (\mathbf{x}_1 - \mathbf{y}_2) - i\mathbf{k}_2 \cdot (\mathbf{x}_2 - \mathbf{y}_1)} + e^{-i\mathbf{k}_1 \cdot (\mathbf{x}_1 - \mathbf{y}_2) + i\mathbf{k}_2 \cdot (\mathbf{x}_2 - \mathbf{y}_1)} \right] \\
&\times \frac{16\alpha_s^2 C_F}{\pi^2 2N_c} \frac{\mathbf{x}_1 - \mathbf{b}_1}{|\mathbf{x}_1 - \mathbf{b}_1|^2} \cdot \frac{\mathbf{y}_2 - \mathbf{b}_2}{|\mathbf{y}_2 - \mathbf{b}_2|^2} \frac{\mathbf{x}_2 - \mathbf{b}_2}{|\mathbf{x}_2 - \mathbf{b}_2|^2} \cdot \frac{\mathbf{y}_1 - \mathbf{b}_1}{|\mathbf{y}_1 - \mathbf{b}_1|^2} \\
&\times \left[Q(\mathbf{x}_1, \mathbf{y}_1, \mathbf{x}_2, \mathbf{y}_2) - Q(\mathbf{x}_1, \mathbf{y}_1, \mathbf{x}_2, \mathbf{b}_2) - Q(\mathbf{x}_1, \mathbf{y}_1, \mathbf{b}_2, \mathbf{y}_2) + S_G(\mathbf{x}_1, \mathbf{y}_1) \right. \\
&- Q(\mathbf{x}_1, \mathbf{b}_1, \mathbf{x}_2, \mathbf{y}_2) + Q(\mathbf{x}_1, \mathbf{b}_1, \mathbf{x}_2, \mathbf{b}_2) + Q(\mathbf{x}_1, \mathbf{b}_1, \mathbf{b}_2, \mathbf{y}_2) - S_G(\mathbf{x}_1, \mathbf{b}_1) \\
&- Q(\mathbf{b}_1, \mathbf{y}_1, \mathbf{x}_2, \mathbf{y}_2) + Q(\mathbf{b}_1, \mathbf{y}_1, \mathbf{x}_2, \mathbf{b}_2) + Q(\mathbf{b}_1, \mathbf{y}_1, \mathbf{b}_2, \mathbf{y}_2) - S_G(\mathbf{b}_1, \mathbf{y}_1) \\
&\left. + S_G(\mathbf{x}_2, \mathbf{y}_2) - S_G(\mathbf{x}_2, \mathbf{b}_2) - S_G(\mathbf{b}_2, \mathbf{y}_2) + 1 \right]. \tag{4.18}
\end{aligned}$$

Just like in 4.11, the dipole and quadrupole scattering amplitudes in 4.18 can be evaluated either in the MV model or by using BK and JIMWLK evolution equations. The quadrupole amplitude evolution equation was derived in the large- N_c limit in [84], and beyond the large- N_c limit in [86]. Again, 4.18 is valid only as long as the rapidities y_1 and y_2 of the two produced gluons are close to each other, $|y_2 - y_1| \lesssim 1/\alpha_s$, such that no small- x evolution corrections need to be included in the $[y_1, y_2]$ rapidity interval.

4.1.4 Two-gluon production with long-range rapidity correlations: the net result

Equations (4.11) and (4.18), when combined, give us the two-gluon production cross section in the heavy-light ion collisions:

$$\frac{d\sigma}{d^2k_1 dy_1 d^2k_2 dy_2} = \frac{d\sigma_{square}}{d^2k_1 dy_1 d^2k_2 dy_2} + \frac{d\sigma_{crossed}}{d^2k_1 dy_1 d^2k_2 dy_2}. \tag{4.19}$$

4.2 Long-range rapidity correlations: away-side and near-side; HBT correlations

Our goal now is to evaluate the correlations resulting from the two-gluon production cross section 4.19, that is from the cross sections in Eqs. (4.11) and (4.18). The

first step is to evaluate the interaction with the target. We will be working in the quasi-classical MV/GM limit, where the interaction and, hence, the production cross sections 4.11 and 4.18, are rapidity-independent.

We begin with the cross section in 4.11. Even in the quasi-classical limit, the evaluation of the interactions with the target is computationally intensive (though conceptually rather straightforward). To simplify the calculation we will also employ the large- N_c expansion: we assume that the nucleons in the nuclei are made out of an order- N_c^2 valence quarks (or gluons), such that the saturation scale, which in such case is proportional to $Q_{s0}^2 \sim \alpha_s^2 N_c^2$, is constant in the 't Hooft's large- N_c limit. In the saturation physics framework such approximation was used in [84] for the quadrupole operator giving a reasonably good approximation to the exact answer [87]. Similar approximations are frequently used (albeit, often implicitly) in applications of anti-de Sitter space/conformal field theory (AdS/CFT) correspondence to collisions of heavy ions modeled by shock waves [89–92].

At the leading order in $1/N_c^2$ expansion of 4.11 the interaction with the target factorizes, as discussed around 4.12. In addition, the cross section in 4.18 is $1/N_c^2$ -suppressed (as compared to the leading term in 4.11) and can be neglected at the leading order in N_c . The correlation function is then given by 2.27 with the single gluon production cross section from 3.27. In the MV/GM approximation the gluon color dipole interaction with the target is [74]

$$S_G(\mathbf{x}_1, \mathbf{x}_2, y = 0) = \exp \left[-\frac{1}{4} |\mathbf{x}_1 - \mathbf{x}_2|^2 Q_{s0}^2 \left(\frac{\mathbf{x}_1 + \mathbf{x}_2}{2} \right) \ln \left(\frac{1}{|\mathbf{x}_1 - \mathbf{x}_2| \Lambda} \right) \right] \quad (4.20)$$

with Q_{s0} the rapidity-independent gluon saturation scale in the quasi-classical limit evaluated at the dipole center-of-mass $(\mathbf{x}_1 + \mathbf{x}_2)/2$ and Λ an infrared (IR) cutoff.

We see that the quasi-classical single gluon production cross section is rapidity-independent and, for unpolarized nuclei and for perturbatively large k_T [77], is also independent of the azimuthal angle ϕ of the transverse momentum \mathbf{k} of the outgoing gluon. We conclude that at the leading order in $1/N_c^2$ in the quasi-classical approximation the geometric correlations are almost absent and the correlation function 2.27 is approximately zero.

Non-trivial correlations can be obtained from 4.11 by expanding the interaction term to the first non-trivial order in $1/N_c^2$. To this end we write a correlator of two Wilson line traces as

$$\begin{aligned} \frac{1}{(N_c^2 - 1)^2} \langle Tr[U_{\mathbf{x}_1} U_{\mathbf{x}_2}^\dagger] Tr[U_{\mathbf{x}_3} U_{\mathbf{x}_4}^\dagger] \rangle = \\ \frac{1}{(N_c^2 - 1)^2} \langle Tr[U_{\mathbf{x}_1} U_{\mathbf{x}_2}^\dagger] \rangle \langle Tr[U_{\mathbf{x}_3} U_{\mathbf{x}_4}^\dagger] \rangle + \Delta(\mathbf{x}_1, \mathbf{x}_2, \mathbf{x}_3, \mathbf{x}_4), \end{aligned} \quad (4.21)$$

where the correction to the factorized expression 4.12, denoted by Δ , is order- $1/N_c^2$. (Note that each adjoint trace in 4.21 is order- N_c^2 , such that its left-hand side, as well as the first term on its right-hand side, are order-one in N_c counting.)

The leading order- $1/N_c^2$ contribution to Δ is derived in the Appx. A, with the result being

$$\begin{aligned} \Delta(\mathbf{x}_1, \mathbf{x}_2, \mathbf{x}_3, \mathbf{x}_4) = \\ \frac{(D_3 - D_2)^2}{N_c^2} \left[\frac{e^{D_1}}{D_1 - D_2} - \frac{2e^{D_1}}{(D_1 - D_2)^2} + \frac{e^{D_1}}{D_1 - D_3} - \frac{2e^{D_1}}{(D_1 - D_3)^2} \right. \\ \left. + \frac{2e^{\frac{1}{2}(D_1+D_2)}}{(D_1 - D_2)^2} + \frac{2e^{\frac{1}{2}(D_1+D_3)}}{(D_1 - D_3)^2} \right] + O\left(\frac{1}{N_c^4}\right), \end{aligned} \quad (4.22)$$

where we have defined

$$D_1 = -\frac{Q_{s0}^2}{4} \left[|\mathbf{x}_1 - \mathbf{x}_2|^2 \ln \left(\frac{1}{|\mathbf{x}_1 - \mathbf{x}_2| \Lambda} \right) + |\mathbf{x}_3 - \mathbf{x}_4|^2 \ln \left(\frac{1}{|\mathbf{x}_3 - \mathbf{x}_4| \Lambda} \right) \right] \quad (4.23a)$$

$$D_2 = -\frac{Q_{s0}^2}{4} \left[|\mathbf{x}_1 - \mathbf{x}_3|^2 \ln \left(\frac{1}{|\mathbf{x}_1 - \mathbf{x}_3| \Lambda} \right) + |\mathbf{x}_2 - \mathbf{x}_4|^2 \ln \left(\frac{1}{|\mathbf{x}_2 - \mathbf{x}_4| \Lambda} \right) \right] \quad (4.23b)$$

$$D_3 = -\frac{Q_{s0}^2}{4} \left[|\mathbf{x}_1 - \mathbf{x}_4|^2 \ln \left(\frac{1}{|\mathbf{x}_1 - \mathbf{x}_4| \Lambda} \right) + |\mathbf{x}_2 - \mathbf{x}_3|^2 \ln \left(\frac{1}{|\mathbf{x}_2 - \mathbf{x}_3| \Lambda} \right) \right] \quad (4.23c)$$

assuming, for simplicity, that all the saturation scales are evaluated at the same impact parameter.

Using 4.21 in 4.11 we see that the correlated part of the two-gluon production cross section is

$$\begin{aligned} \frac{d\sigma_{square}^{(corr)}}{d^2k_1 dy_1 d^2k_2 dy_2} &= \frac{\alpha_s^2 C_F^2}{16 \pi^8} \int d^2B d^2b_1 d^2b_2 T_1(\mathbf{B} - \mathbf{b}_1) T_1(\mathbf{B} - \mathbf{b}_2) d^2x_1 d^2y_1 d^2x_2 d^2y_2 \\ &\times e^{-i \mathbf{k}_1 \cdot (\mathbf{x}_1 - \mathbf{y}_1) - i \mathbf{k}_2 \cdot (\mathbf{x}_2 - \mathbf{y}_2)} \frac{\mathbf{x}_1 - \mathbf{b}_1}{|\mathbf{x}_1 - \mathbf{b}_1|^2} \cdot \frac{\mathbf{y}_1 - \mathbf{b}_1}{|\mathbf{y}_1 - \mathbf{b}_1|^2} \frac{\mathbf{x}_2 - \mathbf{b}_2}{|\mathbf{x}_2 - \mathbf{b}_2|^2} \cdot \frac{\mathbf{y}_2 - \mathbf{b}_2}{|\mathbf{y}_2 - \mathbf{b}_2|^2} \\ &\times [\Delta(\mathbf{x}_1, \mathbf{y}_1, \mathbf{x}_2, \mathbf{y}_2) - \Delta(\mathbf{x}_1, \mathbf{y}_1, \mathbf{x}_2, \mathbf{b}_2) - \Delta(\mathbf{x}_1, \mathbf{y}_1, \mathbf{b}_2, \mathbf{y}_2) - \Delta(\mathbf{x}_1, \mathbf{b}_1, \mathbf{x}_2, \mathbf{y}_2) \\ &- \Delta(\mathbf{b}_1, \mathbf{y}_1, \mathbf{x}_2, \mathbf{y}_2) + \Delta(\mathbf{x}_1, \mathbf{b}_1, \mathbf{x}_2, \mathbf{b}_2) + \Delta(\mathbf{x}_1, \mathbf{b}_1, \mathbf{b}_2, \mathbf{y}_2) + \Delta(\mathbf{b}_1, \mathbf{y}_1, \mathbf{x}_2, \mathbf{b}_2) \\ &+ \Delta(\mathbf{b}_1, \mathbf{y}_1, \mathbf{b}_2, \mathbf{y}_2)]. \end{aligned} \quad (4.24)$$

4.24 along with the expression for Δ in 4.22 are our most complete results for the contribution to the two-gluon production cross section coming from 4.11 in the quasi-classical regime of the heavy–light ion collisions in the large- N_c limit. The evaluation of the full 4.24 appears to be rather involved and is left for the future work.

Instead we will expand 4.22 and use the result in 4.24 to obtain the correlated gluon production at the lowest non-trivial order. This result can be used to elucidate the structure of the long-range rapidity correlations, along with the comparison to the existing expressions in the literature.

At the lowest non-trivial order in D_i 's (that is, since each D_i represents a two-gluon exchange with the target, at the lowest order in the number of gluon exchanges

corresponding to $k_{1T}, k_{2T} \gg Q_{s0}$), 4.22 becomes

$$\Delta(\mathbf{x}_1, \mathbf{x}_2, \mathbf{x}_3, \mathbf{x}_4) \approx \frac{(D_3 - D_2)^2}{2 N_c^2}. \quad (4.25)$$

Substituting this into 4.24 we can further simplify the expression by assuming that for the connected diagrams that contribute to the Δ 's one has \mathbf{b}_1 and \mathbf{b}_2 perturbatively close to each other, with the typical separation between these two impact parameters much smaller than the nucleon radius. Since the nuclear profile functions for a large nucleus do not vary much over perturbatively short distances we can put $\mathbf{b}_1 \approx \mathbf{b}_2 \approx \mathbf{b}$ in the arguments of T_1 's and Q_{s0} , where $\mathbf{b} \equiv (\mathbf{b}_1 + \mathbf{b}_2)/2$. Defining $\Delta\mathbf{b} \equiv \mathbf{b}_1 - \mathbf{b}_2$ we can write $d^2b_1 d^2b_2 = d^2b d^2\Delta b$. The integral over $\Delta\mathbf{b}$ can be then carried out with the help of a Fourier transform

$$\frac{1}{4} |\mathbf{x}|^2 \ln \left(\frac{1}{|\mathbf{x}| \Lambda} \right) = \int \frac{d^2l}{2\pi} (1 - e^{i\mathbf{l}\cdot\mathbf{x}}) \frac{1}{(\mathbf{l}^2)^2} \quad (4.26)$$

used to replace $(D_3 - D_2)^2$ in 4.25 and, hence, all Δ 's in 4.24 as a double Fourier-integral: for instance

$$\begin{aligned} & \Delta(\mathbf{x}_1, \mathbf{y}_1, \mathbf{x}_2, \mathbf{y}_2) \\ &= \frac{Q_{s0}^4}{2 N_c^2} \int \frac{d^2l d^2l'}{(2\pi)^2} \frac{1}{(\mathbf{l}^2)^2} \frac{1}{(\mathbf{l}'^2)^2} [e^{i\mathbf{l}\cdot(\mathbf{x}_1-\mathbf{x}_2)} + e^{i\mathbf{l}\cdot(\mathbf{y}_1-\mathbf{y}_2)} - e^{i\mathbf{l}\cdot(\mathbf{x}_1-\mathbf{y}_2)} - e^{i\mathbf{l}\cdot(\mathbf{y}_1-\mathbf{x}_2)}] \\ & \quad \times [e^{-i\mathbf{l}'\cdot(\mathbf{x}_1-\mathbf{x}_2)} + e^{-i\mathbf{l}'\cdot(\mathbf{y}_1-\mathbf{y}_2)} - e^{-i\mathbf{l}'\cdot(\mathbf{x}_1-\mathbf{y}_2)} - e^{-i\mathbf{l}'\cdot(\mathbf{y}_1-\mathbf{x}_2)}] \\ &= \frac{Q_{s0}^4}{2 N_c^2} \int \frac{d^2l d^2l'}{(2\pi)^2} \frac{1}{(\mathbf{l}^2)^2} \frac{1}{(\mathbf{l}'^2)^2} [e^{i\mathbf{l}\cdot(\tilde{\mathbf{x}}_1-\tilde{\mathbf{x}}_2)} + e^{i\mathbf{l}\cdot(\tilde{\mathbf{y}}_1-\tilde{\mathbf{y}}_2)} - e^{i\mathbf{l}\cdot(\tilde{\mathbf{x}}_1-\tilde{\mathbf{y}}_2)} - e^{i\mathbf{l}\cdot(\tilde{\mathbf{y}}_1-\tilde{\mathbf{x}}_2)}] \\ & \quad \times [e^{-i\mathbf{l}'\cdot(\tilde{\mathbf{x}}_1-\tilde{\mathbf{x}}_2)} + e^{-i\mathbf{l}'\cdot(\tilde{\mathbf{y}}_1-\tilde{\mathbf{y}}_2)} - e^{-i\mathbf{l}'\cdot(\tilde{\mathbf{x}}_1-\tilde{\mathbf{y}}_2)} - e^{-i\mathbf{l}'\cdot(\tilde{\mathbf{y}}_1-\tilde{\mathbf{x}}_2)}] e^{i(\mathbf{l}-\mathbf{l}')\cdot\Delta\mathbf{b}} \quad (4.27) \end{aligned}$$

where we employed the substitution

$$\tilde{\mathbf{x}}_1 = \mathbf{x}_1 - \mathbf{b}_1, \quad \tilde{\mathbf{y}}_1 = \mathbf{y}_1 - \mathbf{b}_1, \quad \tilde{\mathbf{x}}_2 = \mathbf{x}_2 - \mathbf{b}_2, \quad \tilde{\mathbf{y}}_2 = \mathbf{y}_2 - \mathbf{b}_1. \quad (4.28)$$

Performing similar substitutions for all Δ 's in 4.24, we can integrate over $\Delta\mathbf{b}$, $\tilde{\mathbf{x}}_1$, $\tilde{\mathbf{x}}_2$, $\tilde{\mathbf{y}}_1$, $\tilde{\mathbf{y}}_2$, and \mathbf{l}' . After some algebra one arrives at (cf. [47, 48])

$$\frac{d\sigma_{square}^{(corr)}}{d^2k_1 dy_1 d^2k_2 dy_2} \Big|_{LO} = \frac{\alpha_s^2}{4\pi^4} \int d^2B d^2b [T_1(\mathbf{B} - \mathbf{b})]^2 \frac{Q_{s0}^4(\mathbf{b})}{\mathbf{k}_1^2 \mathbf{k}_2^2} \times \int_{\Lambda} \frac{d^2l}{(\mathbf{l}^2)^2} \left[\frac{1}{(\mathbf{k}_1 - \mathbf{l})^2 (\mathbf{k}_2 + \mathbf{l})^2} + \frac{1}{(\mathbf{k}_1 - \mathbf{l})^2 (\mathbf{k}_2 - \mathbf{l})^2} \right], \quad (4.29)$$

where the subscript *LO* denotes the lowest-order cross section.

Equation 4.29 is illustrated in 4.8 by regular Feynman diagrams that contribute to its right-hand-side (cf. [47, 48]): these diagrams are referred to as the “glasma” graphs in the literature. The momenta of the gluon lines are labeled in 4.8, and the triple gluon vertices, marked by the dark circles, are the effective Lipatov vertices [24, 93]. These particular graphs contribute to the first and the second terms in the square brackets of 4.29 correspondingly, and can be calculated by taking two Lipatov vertices squared.

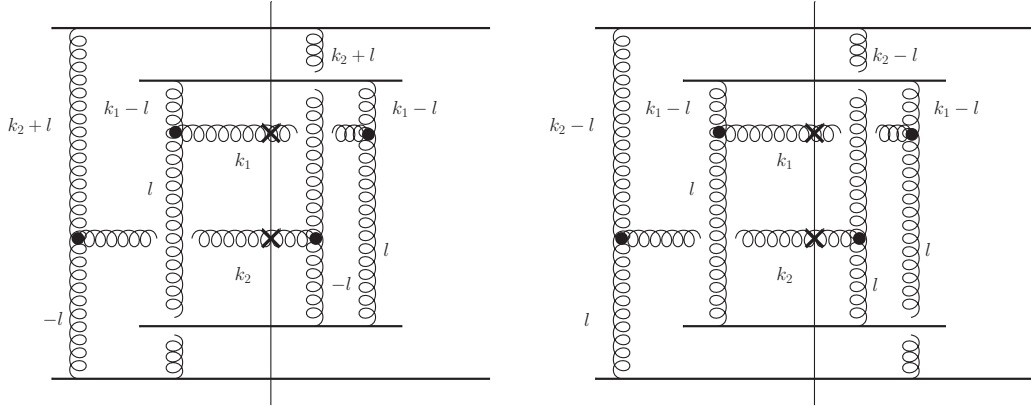


Figure 4.8: Examples of diagrams generating contributions to 4.29: the left panel represent the away-side correlations (the first term in 4.29), while the right panel contributes near-side correlations (the second term in 4.29). The *t*-channel gluon momenta flow toward the triple-gluon vertices to the left of the cut, and away from those vertices to the right of the cut.

The obtained expression 4.29 contains both the near-side and away-side azimuthal correlations [47, 48]: clearly the first term in the square brackets of 4.29 contains poles at $\mathbf{l} = \mathbf{k}_1$ and $\mathbf{l} = -\mathbf{k}_2$, which, after integration over l , lead to a contribution²

$$\sim \frac{1}{(\mathbf{k}_1 + \mathbf{k}_2)^2}, \quad (4.30)$$

characteristic of the away-side correlations.

The second term in the square brackets of 4.29 has poles at $\mathbf{l} = \mathbf{k}_1$ and $\mathbf{l} = \mathbf{k}_2$, yielding a contribution

$$\sim \frac{1}{(\mathbf{k}_1 - \mathbf{k}_2)^2}, \quad (4.31)$$

indicating near-side correlations. Note that all correlations are long-range in rapidity since the cross section 4.29 is rapidity-independent.

Now we turn our attention to 4.18. There the cross section contribution itself is $1/N_c^2$ -suppressed as compared to the leading (uncorrelated) part of 4.11: hence we need to evaluate the interaction with the target in 4.18 using the large- N_c limit. We work in the same quasi-classical MV/GM approximation, along with the large- N_c limit. The fundamental (quark) quadrupole amplitude was evaluated in this approximation in [84] (see Eq. (14) there), yielding

$$Q_{quark}(\mathbf{x}_1, \mathbf{x}_2, \mathbf{x}_3, \mathbf{x}_4) = e^{D_1/2} + \frac{D_3 - D_2}{D_1 - D_3} [e^{D_1/2} - e^{D_3/2}]. \quad (4.32)$$

Since the adjoint (gluon) quadrupole 4.16 in the large- N_c limit is simply

$$Q(\mathbf{x}_1, \mathbf{x}_2, \mathbf{x}_3, \mathbf{x}_4) = [Q_{quark}(\mathbf{x}_1, \mathbf{x}_2, \mathbf{x}_3, \mathbf{x}_4)]^2 \quad (4.33)$$

²Note that both terms in 4.29 also contain a pole at $\mathbf{l} = 0$, which leads to a correlated contribution independent of the azimuthal angle between \mathbf{k}_1 and \mathbf{k}_2 .

we get

$$Q(\mathbf{x}_1, \mathbf{x}_2, \mathbf{x}_3, \mathbf{x}_4) = \left[e^{D_1/2} + \frac{D_3 - D_2}{D_1 - D_3} (e^{D_1/2} - e^{D_3/2}) \right]^2. \quad (4.34)$$

Equations 4.34 and 4.20, when used in 4.18, give us the remaining contribution to the two-gluon production cross section in the quasi-classical approximation, which has to be added to 4.24.

Again the full expression 4.18 is hard to evaluate: instead, similar to 4.29, we will consider the limit of large $k_{1T} = |\mathbf{k}_1|$ and $k_{2T} = |\mathbf{k}_2|$: $k_1, k_2 \gg Q_{s0}$. Expanding 4.34 in the powers of D_i 's yields

$$\begin{aligned} Q(\mathbf{x}_1, \mathbf{x}_2, \mathbf{x}_3, \mathbf{x}_4) &= 1 + D_1 - D_2 + D_3 \\ &+ \frac{1}{4} [2 D_1^2 + D_2^2 + 2 D_3^2 - 3 D_1 D_2 - 3 D_2 D_3 + 3 D_1 D_3] + O(D_i^3). \end{aligned} \quad (4.35)$$

Using this result along with a similar expansion for 4.20 in 4.17, and employing again the Fourier transform 4.26 along with the substitution 4.28 one can write

$$\begin{aligned} &Int_{crossed}(\mathbf{x}_1, \mathbf{y}_1, \mathbf{b}_1, \mathbf{x}_2, \mathbf{y}_2, \mathbf{b}_2) \\ &= Q_{s0}^4 \int \frac{d^2 l d^2 l'}{(2\pi)^2} \frac{1}{(\mathbf{l}^2)^2} \frac{1}{(\mathbf{l}'^2)^2} \left\{ e^{i(\mathbf{l}-\mathbf{l}') \cdot \Delta \mathbf{b}} \left(1 - e^{i\mathbf{l}' \cdot \tilde{\mathbf{x}}_2} \right) \left(1 - e^{-i\mathbf{l} \cdot \tilde{\mathbf{y}}_2} \right) \right. \\ &\times \left[\frac{1}{2} \left(1 - e^{-i\mathbf{l}' \cdot \tilde{\mathbf{x}}_1} \right) \left(1 - e^{i\mathbf{l} \cdot \tilde{\mathbf{y}}_1} \right) + \left(1 - e^{i\mathbf{l} \cdot \tilde{\mathbf{x}}_1} \right) \left(1 - e^{-i\mathbf{l}' \cdot \tilde{\mathbf{y}}_1} \right) \right] \\ &\left. + \left(1 - e^{i\mathbf{l} \cdot \tilde{\mathbf{x}}_1} \right) \left(1 - e^{-i\mathbf{l}' \cdot \tilde{\mathbf{x}}_2} \right) \left(1 - e^{-i\mathbf{l} \cdot \tilde{\mathbf{y}}_1} \right) \left(1 - e^{i\mathbf{l}' \cdot \tilde{\mathbf{y}}_2} \right) \right\} \end{aligned} \quad (4.36)$$

where the $\mathbf{l} \leftrightarrow \mathbf{l}'$, $\mathbf{l} \leftrightarrow -\mathbf{l}$, and $\mathbf{l}' \leftrightarrow -\mathbf{l}'$ symmetries of the integrand were utilized to cast the expression in its present form. Using 4.36 to replace the interaction with the target in 4.18 and integrating over $\tilde{\mathbf{x}}_1$, $\tilde{\mathbf{x}}_2$, $\tilde{\mathbf{y}}_1$, $\tilde{\mathbf{y}}_2$, and, in some terms, over \mathbf{l}' , leads to the following result

$$\left. \frac{d\sigma_{crossed}}{d^2 k_1 dy_1 d^2 k_2 dy_2} \right|_{LO} = \left. \frac{d\sigma_{crossed}^{(corr)}}{d^2 k_1 dy_1 d^2 k_2 dy_2} \right|_{LO} + \left. \frac{d\sigma_{HBT}}{d^2 k_1 dy_1 d^2 k_2 dy_2} \right|_{LO} \quad (4.37)$$

where

$$\begin{aligned}
& \left. \frac{d\sigma_{crossed}^{(corr)}}{d^2k_1 dy_1 d^2k_2 dy_2} \right|_{LO} \\
&= \frac{\alpha_s^2}{32 \pi^4} \int d^2B d^2b [T_1(\mathbf{B} - \mathbf{b})]^2 \frac{Q_{s0}^4(\mathbf{b})}{\mathbf{k}_1^2 \mathbf{k}_2^2} \\
&\times \int \frac{d^2l}{(\mathbf{l}^2)^2 ((\mathbf{l} - \mathbf{k}_1 + \mathbf{k}_2)^2)^2 ((\mathbf{k}_1 - \mathbf{l})^2)^2 ((\mathbf{k}_2 + \mathbf{l})^2)^2} \\
&\times \left\{ [\mathbf{l}^2 (\mathbf{k}_2 + \mathbf{l})^2 + (\mathbf{k}_1 - \mathbf{l})^2 (\mathbf{l} - \mathbf{k}_1 + \mathbf{k}_2)^2 - \mathbf{k}_1^2 (\mathbf{k}_2 - \mathbf{k}_1 + 2\mathbf{l})^2] \right. \\
&\times [\mathbf{l}^2 (\mathbf{k}_1 - \mathbf{l})^2 + (\mathbf{k}_2 + \mathbf{l})^2 (\mathbf{l} - \mathbf{k}_1 + \mathbf{k}_2)^2 - \mathbf{k}_2^2 (\mathbf{k}_2 - \mathbf{k}_1 + 2\mathbf{l})^2] \\
&\left. + 4\mathbf{l}^2 (\mathbf{l} - \mathbf{k}_1 + \mathbf{k}_2)^2 [((\mathbf{k}_1 - \mathbf{l})^2)^2 + ((\mathbf{k}_2 + \mathbf{l})^2)^2] \right\} + (\mathbf{k}_2 \rightarrow -\mathbf{k}_2) \quad (4.38)
\end{aligned}$$

and

$$\begin{aligned}
& \left. \frac{d\sigma_{HBT}}{d^2k_1 dy_1 d^2k_2 dy_2} \right|_{LO} \\
&= \frac{\alpha_s^2}{16 \pi^4} \int d^2B d^2b [T_1(\mathbf{B} - \mathbf{b})]^2 \frac{Q_{s0}^4(\mathbf{b})}{\mathbf{k}_1^2 \mathbf{k}_2^2} [\delta^2(\mathbf{k}_1 - \mathbf{k}_2) + \delta^2(\mathbf{k}_1 + \mathbf{k}_2)] \\
&\times \int_{\Lambda} \frac{d^2l d^2l'}{(\mathbf{l}^2)^2 (\mathbf{l}'^2)^2 ((\mathbf{k}_1 - \mathbf{l})^2)^2 ((\mathbf{k}_1 + \mathbf{l}')^2)^2} \left[\mathbf{l}^2 (\mathbf{k}_1 + \mathbf{l}')^2 + \mathbf{l}'^2 (\mathbf{k}_1 - \mathbf{l})^2 - \mathbf{k}_1^2 (\mathbf{l} + \mathbf{l}')^2 \right]^2. \quad (4.39)
\end{aligned}$$

We will explain the origin of the ‘‘HBT’’ label on the cross section in 4.39 in a little while below: we defer the analysis of 4.39 until then.

First we concentrate on the expression 4.38. We note that by shifting the integration momentum \mathbf{l} one could reduce the second term in the curly brackets (together with the $\mathbf{k}_2 \rightarrow -\mathbf{k}_2$ term) to that in 4.29, thus doubling 4.29. That term is still described by the diagrams of the type shown in 4.8 and gives the near- and away-side correlations in Eqs. 4.30 and 4.31.

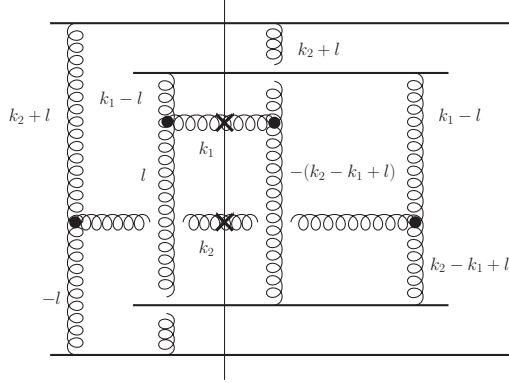


Figure 4.9: An example of a diagram giving a contribution to the first term in the curly brackets of 4.38.

The first term in the curly brackets of 4.38 corresponds to a different class of diagrams, one of which is shown in 4.9. One can see that the diagram in 4.9 contributes two non-forward “squares” of the effective Lipatov vertices. An analysis of the poles of the integral in the first term of 4.38 shows that it contains similar near- and away-side correlations to that in Eqs. 4.30 and 4.31, though with an additional enhancement due to a prefactor,

$$\sim [2(\mathbf{k}_1 \cdot \mathbf{k}_2)^2 - \mathbf{k}_1^2 \mathbf{k}_2^2] \left[\frac{1}{(\mathbf{k}_1 - \mathbf{k}_2)^2} + \frac{1}{(\mathbf{k}_1 + \mathbf{k}_2)^2} \right]. \quad (4.40)$$

The origin of this contribution to correlations is in the non-forward squares of the Lipatov vertices, which is similar to the mechanism for generating long-range rapidity correlations proposed in [59] using two BFKL ladders with non-zero momentum transfer. Note, however, that we do not obtain the correlation proportional to the first power of $\mathbf{k}_1 \cdot \mathbf{k}_2$ advocated in [59], perhaps due to the lowest-order nature of the result 4.38. It appears that the correlations 4.40 resulting from the lowest-order diagrams like the one depicted in 4.9 have not been considered in the literature yet.

Note that the away- and the near-side correlations enter Eqs. 4.29 and 4.38 on equal footing: in fact, one could be obtained from another by a simple $\mathbf{k}_2 \rightarrow -\mathbf{k}_2$ substitution in either of those expressions. While evaluating the integrals over l in Eqs. 4.29 and 4.38 analytically appears to be rather algebra-intensive, we do not need to do this to observe that, once the l -integral is carried out for one of the terms in the square brackets of 4.29, the answer for the other term is obtained by substituting $\mathbf{k}_2 \rightarrow -\mathbf{k}_2$ in the result. Equation 4.38 simply contains an additive $\mathbf{k}_2 \rightarrow -\mathbf{k}_2$ term.

Since the correlated cross sections 4.29 and 4.38 are sums of two terms related by the $\mathbf{k}_2 \rightarrow -\mathbf{k}_2$ substitution and are symmetric under the $\mathbf{k}_1 \leftrightarrow \mathbf{k}_2$ interchange, we conclude that they are functions only of even powers of \mathbf{k}_1 and \mathbf{k}_2 , that is functions of \mathbf{k}_1^2 , \mathbf{k}_2^2 , $(\mathbf{k}_1 \cdot \mathbf{k}_2)^2$, and possibly $(\mathbf{k}_1 \times \mathbf{k}_2)^2$. Clearly this implies that the Fourier series representation of Eqs. 4.29 and 4.38 would only contain even cosine harmonics of the azimuthal angle, that is

$$\begin{aligned} \left. \frac{d\sigma^{(corr)}}{d^2k_1 dy_1 d^2k_2 dy_2} \right|_{LO} &\equiv \left. \frac{d\sigma_{square}^{(corr)}}{d^2k_1 dy_1 d^2k_2 dy_2} \right|_{LO} + \left. \frac{d\sigma_{crossed}^{(corr)}}{d^2k_1 dy_1 d^2k_2 dy_2} \right|_{LO} \\ &\sim \sum_{n=0}^{\infty} c_n(k_{1T}, k_{2T}) \cos(2n \Delta\phi) \end{aligned} \quad (4.41)$$

where $\Delta\phi = \phi_1 - \phi_2$ is the angle between momenta \mathbf{k}_1 and \mathbf{k}_2 while $k_{1T} = |\mathbf{k}_1|$ and $k_{2T} = |\mathbf{k}_2|$. Here $c_n(k_1, k_2)$ are some coefficient to be determined by an exact calculation. It is quite interesting that only even harmonics contribute to the correlated cross section in 4.41. Let us stress here that we have not made any assumptions about the centrality of the collision: we do not have an almond-shaped overlap of the two nuclei. In fact we integrate over all impact parameters \mathbf{B} . (Also the impact parameter dependence factorizes from the rest of the expression.) Hence the correlation in 4.41 is not caused by the geometry of the collision.

To construct the correlation function one has to use Eqs. 4.29 and 4.38 in 2.25. In the latter, the uncorrelated two-gluon production would dominate in the denominator of the normalization factor, that is, in the denominator of the first factor on its right-hand side. The single-gluon production cross-section 3.27 at the lowest order is equal to (see [19] and references therein)

$$\left\langle \frac{d\sigma^{pA_2}}{d^2k dy d^2b} \right\rangle = \frac{\alpha_s C_F}{\pi^2} \frac{Q_{s0}^2(\mathbf{b})}{k_T^4} \ln \frac{k_T^2}{\Lambda^2}. \quad (4.42)$$

Using this along with the sum of Eqs. 4.29 and 4.38 in 2.25 and taking the large- N_c limit in 4.42 we get

$$\begin{aligned} C(\mathbf{k}_1, y_1, \mathbf{k}_2, y_2) \Big|_{LO} &= \frac{1}{N_c^2} \frac{\int d^2B d^2b [T_1(\mathbf{B} - \mathbf{b})]^2 Q_{s0}^4(\mathbf{b})}{\int d^2B d^2b_1 d^2b_2 T_1(\mathbf{B} - \mathbf{b}_1) T_1(\mathbf{B} - \mathbf{b}_2) Q_{s0}^2(\mathbf{b}_1) Q_{s0}^2(\mathbf{b}_2)} \\ &\times \frac{\mathbf{k}_1^2 \mathbf{k}_2^2}{\ln \frac{k_1^2}{\Lambda^2} \ln \frac{k_2^2}{\Lambda^2}} \left\{ 2 \int_{\Lambda} \frac{d^2l}{(l^2)^2} \left[\frac{1}{(\mathbf{k}_1 - \mathbf{l})^2 (\mathbf{k}_2 + \mathbf{l})^2} + \frac{1}{(\mathbf{k}_1 - \mathbf{l})^2 (\mathbf{k}_2 - \mathbf{l})^2} \right] \right. \\ &+ \frac{1}{8} \left[\int \frac{d^2l}{(l^2)^2 ((\mathbf{l} - \mathbf{k}_1 + \mathbf{k}_2)^2)^2 ((\mathbf{k}_1 - \mathbf{l})^2)^2 ((\mathbf{k}_2 + \mathbf{l})^2)^2} \right. \\ &\times [l^2 (\mathbf{k}_2 + \mathbf{l})^2 + (\mathbf{k}_1 - \mathbf{l})^2 (\mathbf{l} - \mathbf{k}_1 + \mathbf{k}_2)^2 - \mathbf{k}_1^2 (\mathbf{k}_2 - \mathbf{k}_1 + 2\mathbf{l})^2] \\ &\left. \left. \times [l^2 (\mathbf{k}_1 - \mathbf{l})^2 + (\mathbf{k}_2 + \mathbf{l})^2 (\mathbf{l} - \mathbf{k}_1 + \mathbf{k}_2)^2 - \mathbf{k}_2^2 (\mathbf{k}_2 - \mathbf{k}_1 + 2\mathbf{l})^2] + (\mathbf{k}_2 \rightarrow -\mathbf{k}_2) \right] \right\}. \end{aligned} \quad (4.43)$$

To evaluate this further let us assume for a moment that both colliding nuclei are simply cylinders oriented along the collision axis, such that the nuclear profile functions of the nuclei are $T_i(\mathbf{b}) = 2\rho R_i \theta(R_i - b)$ where $i = 1, 2$ labels the nuclei, ρ is the (constant) nucleon number density in the nucleus, R_1 and R_2 are the radii of the projectile and target nuclei, and the cylindrical nucleus is assumed to have length $2R_i$ along its axis. Assuming that both nuclei are large and neglecting the edge effects, we can neglect the \mathbf{b}_1 and \mathbf{b}_2 dependence in these nuclear profile functions of both nuclei. Since the gluon saturation scale in the MV model is $Q_{s0}^2 = 4\pi\alpha_s^2 T_2(\mathbf{b})$ we

obtain in the $R_1 \ll R_2$ limit

$$\begin{aligned}
C(\mathbf{k}_1, y_1, \mathbf{k}_2, y_2)|_{LO} &= \frac{1}{N_c^2 \pi R_1^2} \frac{\mathbf{k}_1^2 \mathbf{k}_2^2}{\ln \frac{k_1^2}{\Lambda^2} \ln \frac{k_2^2}{\Lambda^2}} \\
&\times \left\{ 2 \int_{\Lambda} \frac{d^2 l}{(l^2)^2} \left[\frac{1}{(\mathbf{k}_1 - \mathbf{l})^2 (\mathbf{k}_2 + \mathbf{l})^2} + \frac{1}{(\mathbf{k}_1 - \mathbf{l})^2 (\mathbf{k}_2 - \mathbf{l})^2} \right] \right. \\
&+ \frac{1}{8} \left[\int \frac{d^2 l}{(l^2)^2 ((\mathbf{l} - \mathbf{k}_1 + \mathbf{k}_2)^2)^2 ((\mathbf{k}_1 - \mathbf{l})^2)^2 ((\mathbf{k}_2 + \mathbf{l})^2)^2} \right. \\
&\times [\mathbf{l}^2 (\mathbf{k}_2 + \mathbf{l})^2 + (\mathbf{k}_1 - \mathbf{l})^2 (\mathbf{l} - \mathbf{k}_1 + \mathbf{k}_2)^2 - \mathbf{k}_1^2 (\mathbf{k}_2 - \mathbf{k}_1 + 2\mathbf{l})^2] \\
&\times [\mathbf{l}^2 (\mathbf{k}_1 - \mathbf{l})^2 + (\mathbf{k}_2 + \mathbf{l})^2 (\mathbf{l} - \mathbf{k}_1 + \mathbf{k}_2)^2 - \mathbf{k}_2^2 (\mathbf{k}_2 - \mathbf{k}_1 + 2\mathbf{l})^2] + (\mathbf{k}_2 \rightarrow -\mathbf{k}_2) \left. \right] \left. \right\}. \tag{4.44}
\end{aligned}$$

Indeed the correlator is suppressed by a power of N_c^2 and a power of the cross sectional area of the projectile nucleus πR_1^2 , as discussed in the literature [47–50, 60].

While our conclusion about the correlator 4.44 and the cross section 4.41 contributing only to even Fourier harmonics has been verified above at the lowest order only, it is true for the full two-gluon production cross section in heavy-light ion collisions 4.19. This can be seen by noticing that $\mathbf{k}_2 \rightarrow -\mathbf{k}_2$ substitution in 4.24 does not change the cross section, as it is equivalent to the $\mathbf{x}_2 \leftrightarrow \mathbf{y}_2$ interchange of the integration variables. The integrand of 4.24 (or, equivalently, of 4.11) is invariant under $\mathbf{x}_2 \leftrightarrow \mathbf{y}_2$ interchange since the gluon is its own anti-particle such that $Tr [U_{\mathbf{x}} U_{\mathbf{y}}^\dagger] = Tr [U_{\mathbf{y}} U_{\mathbf{x}}^\dagger]$. The expression in 4.38 is explicitly invariant under $\mathbf{k}_2 \rightarrow -\mathbf{k}_2$ substitution. Hence the net correlated cross section 4.19 is an even function of \mathbf{k}_2 . Note also that Eqs. 4.11 and 4.18 are $\mathbf{k}_1 \leftrightarrow \mathbf{k}_2$ -symmetric: in 4.11 and in the term arising from the first exponential in 4.18 the symmetry is a consequence of the symmetry of the integrand under the simultaneous $\mathbf{x}_1 \leftrightarrow \mathbf{x}_2$, $\mathbf{y}_1 \leftrightarrow \mathbf{y}_2$, and $\mathbf{b}_1 \leftrightarrow \mathbf{b}_2$ interchanges. The term multiplying the second exponential in 4.18 is $\mathbf{k}_1 \leftrightarrow \mathbf{k}_2$ -symmetric due to the $\mathbf{x}_1 \leftrightarrow \mathbf{y}_1$, $\mathbf{x}_2 \leftrightarrow \mathbf{y}_2$ symmetry of the integrand, which follows from the following property of the

quadrupole operator: $Tr [U_{x_1} U_{y_1}^\dagger U_{x_2} U_{y_2}^\dagger] = Tr [U_{y_2} U_{x_2}^\dagger U_{y_1} U_{x_1}^\dagger]$. We see that the net cross section 4.19 is decomposable into a Fourier series with even harmonics only. Therefore, the correlation function in the heavy-light ion collision can be also written as an even-harmonics series

$$C(\mathbf{k}_1, y_1, \mathbf{k}_2, y_2) \Big|_{A_2 \gg A_1 \gg 1} \sim \sum_{n=0}^{\infty} d_n(k_{1T}, k_{2T}) \cos(2n \Delta\phi) \quad (4.45)$$

with some coefficients d_n . This conclusion also seems to hold in the case of classical gluon fields produced in a collision of two heavy ions, as can be seen from the result of the full numerical simulation of two-gluon production in heavy ion collisions due to classical gluon field carried out in [94]. The correlators in Figs. 9 and 10 of [94] do appear to have similar-looking maxima at $\Delta\phi = 0$ and $\Delta\phi = \pi$ (within the accuracy of the numerical error bars), though a more careful analysis is needed to figure out if our conclusion is true for two colliding heavy ions.

To better visualize the correlator let us envision a toy model in which multiple rescatterings (and other saturation effects) regulate the singularities at $\mathbf{k}_1 = \pm\mathbf{k}_2$ by the saturation scale Q_{s0} in such a way that the correlator can be modeled as proportional to

$$C_{\text{toy model}}(\mathbf{k}_1, y_1, \mathbf{k}_2, y_2) \sim \frac{1}{(\mathbf{k}_1 - \mathbf{k}_2)^2 + Q_{s0}^2} + \frac{1}{(\mathbf{k}_1 + \mathbf{k}_2)^2 + Q_{s0}^2}. \quad (4.46)$$

This correlator is plotted in 4.10 using arbitrary units along the vertical axis as a function of the azimuthal angle $\Delta\phi$ between \mathbf{k}_1 and \mathbf{k}_2 for $k_1 = k_2 = Q_{s0}$. The shape illustrates what the full correlation function may look like, having identical near- and away-side correlation peaks.

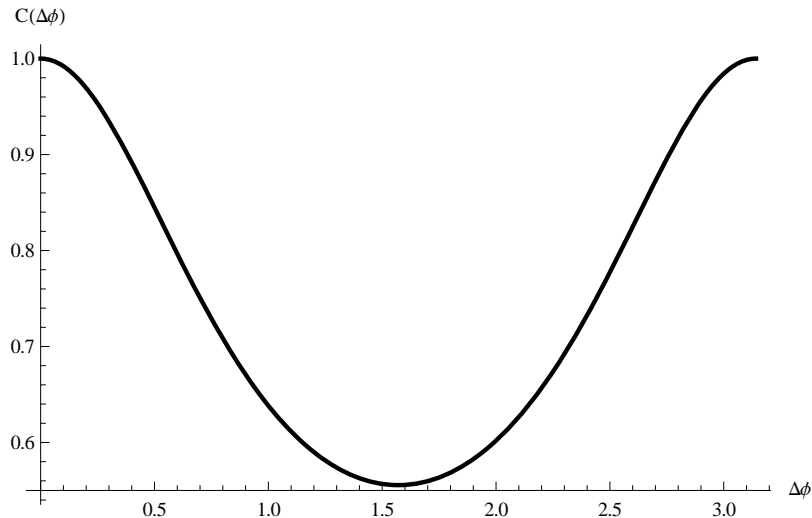


Figure 4.10: A toy azimuthal two-gluon correlation function motivated by the calculation in this section. Vertical scale is arbitrary.

Our conclusion in this section is that the saturation/CGC dynamics in nuclear collisions appears to generate the long-range rapidity correlations which have identical maxima at both $\Delta\phi = 0$ and $\Delta\phi = \pi$ in the azimuthal angle. Such correlations are non-flow in nature, since they do not arise due to almond-shaped geometry of the collisions. (In fact the correlations should persist for the most central heavy ion collisions, though they should be suppressed by an inverse power of the overlap area as discussed above and in [47–50, 60].) However, since the elliptic flow observable v_2 (even in the reaction-plane method) is determined from two-particle correlations, it is possible that the correlations discussed here may contribute to the elliptic flow (and to higher-order even-harmonics flow observables v_{2n}) measured experimentally. It is, therefore, very important to experimentally separate our initial-state correlations from the late-time QGP effects.

Naturally the cumulant analysis [95, 96] is likely to remove these two-particle non-flow correlations from the flow observables. However, the effectiveness of the cumulant method may again depend on the collision geometry. Let us illustrate this by considering the fourth order cumulant for elliptic flow, defined by [95, 96]

$$c_2\{4\} \equiv \langle e^{2i(\phi_1+\phi_2-\phi_3-\phi_4)} \rangle - \langle e^{2i(\phi_1-\phi_3)} \rangle \langle e^{2i(\phi_2-\phi_4)} \rangle - \langle e^{2i(\phi_1-\phi_4)} \rangle \langle e^{2i(\phi_2-\phi_3)} \rangle \quad (4.47)$$

where the angle brackets denote event averages along with the averaging over all angles ϕ_1, ϕ_2, ϕ_3 , and ϕ_4 of the four particles employed in the definition. Using the lowest-order correlations employed in arriving at 4.43 one can straightforwardly show that the cumulant due to these correlations only is proportional to

$$\begin{aligned} c_2\{4\}|_{LO} &\propto \left(\int d^2B d^2b_1 d^2b_2 [T_1(\mathbf{B} - \mathbf{b}_1)]^2 [T_1(\mathbf{B} - \mathbf{b}_2)]^2 Q_{s0}^4(\mathbf{b}_1) Q_{s0}^4(\mathbf{b}_2) \right) \\ &\times \left(\int d^2B d^2b_1 d^2b_2 d^2b_3 d^2b_4 T_1(\mathbf{B} - \mathbf{b}_1) T_1(\mathbf{B} - \mathbf{b}_2) T_1(\mathbf{B} - \mathbf{b}_3) T_1(\mathbf{B} - \mathbf{b}_4) \right. \\ &\quad \left. \times Q_{s0}^2(\mathbf{b}_1) Q_{s0}^2(\mathbf{b}_2) Q_{s0}^2(\mathbf{b}_3) Q_{s0}^2(\mathbf{b}_4) \right)^{-1} \\ &- \left[\frac{\int d^2B d^2b [T_1(\mathbf{B} - \mathbf{b})]^2 Q_{s0}^4(\mathbf{b})}{\int d^2B d^2b_1 d^2b_2 T_1(\mathbf{B} - \mathbf{b}_1) T_1(\mathbf{B} - \mathbf{b}_2) Q_{s0}^2(\mathbf{b}_1) Q_{s0}^2(\mathbf{b}_2)} \right]^2 \end{aligned} \quad (4.48)$$

if the 4-particle correlator in 4.47 (the correlated part of the first term on its right-hand-side) is due to the pairwise correlations of particles 1, 3 and 2, 4 or 1, 4 and 2, 3. Clearly, in the general case, $c_2\{4\}|_{LO}$ from 4.48 is non-zero.³ Moreover, the fourth order cumulant would contain the azimuthal angles dependence resulting from 4.43 but not shown explicitly in 4.48. We see that the geometric correlations from Sec. 2.3.2 may prevent complete removal of these non-flow correlations in the cumulants. Just like with the correlator of 2.30, the above non-flow correlations can be completely

³Note, however, that for the heavy-light nuclear collision case considered here, $A_1 \ll A_2$, and for cylindrical nuclei, one gets $c_2\{4\}|_{LO} = 0$.

removed from the cumulants for the fixed impact parameter \mathbf{B} : if we fix \mathbf{B} in 4.48 (that is, remove all the d^2B integrations from it), we get $c_2\{4\}|_{LO} = 0$, which is exactly what the cumulant is designed to do [95,96] — completely cancel for non-flow correlations. Note that since, in the actual experimental analyses one effectively integrates over \mathbf{B} in a given centrality bin, it is possible that some non-flow correlations 4.43 would remain in the cumulant 4.48. Even fixing $|\mathbf{B}|$ precisely and integrating over the angles of \mathbf{B} may generate a non-zero contribution of these correlations to the cumulant. The question of the interplay of the true QGP flow and the non-flow correlations discussed here has to be resolved by a more detailed numerical study.

To clarify the physical meaning of the cross section obtained in 4.39 we again consider a collisions of cylindrical nuclei. With this simplification we can consider one of the terms in the interaction with the target, say the $Q(\mathbf{x}_1, \mathbf{y}_1, \mathbf{x}_2, \mathbf{y}_2)$ in 4.17. Among many terms which contribute to the quadrupole amplitude in 4.35, there is a term

$$\begin{aligned}
& Q(\mathbf{x}_1, \mathbf{y}_1, \mathbf{x}_2, \mathbf{y}_2) \Big|_{\text{order-}Q_{s0}^4} \\
& \sim (\mathbf{x}_1 - \mathbf{y}_1)^2 Q_{s0}^2 \ln \left(\frac{1}{|\mathbf{x}_1 - \mathbf{y}_1| \Lambda} \right) (\mathbf{x}_2 - \mathbf{y}_2)^2 Q_{s0}^2 \ln \left(\frac{1}{|\mathbf{x}_2 - \mathbf{y}_2| \Lambda} \right) + \dots
\end{aligned} \tag{4.49}$$

Using 4.49 in 4.18 and changing the interaction variables to those defined in 4.28 we see that the remaining \mathbf{b}_1 and \mathbf{b}_2 integrals, after shifting those variables by \mathbf{B} , become simple Fourier transforms of the projectile nucleus profile function $T_1(\mathbf{b})$,

$$\int d^2b_1 d^2b_2 T_1(\mathbf{b}_1) T_1(\mathbf{b}_2) e^{-i(\mathbf{k}_1 - \mathbf{k}_2) \cdot (\mathbf{b}_1 - \mathbf{b}_2)} + (\mathbf{k}_2 \rightarrow -\mathbf{k}_2). \tag{4.50}$$

In the limit of a sufficiently large projectile nucleus the Fourier transforms give a delta-function, yielding

$$\frac{d\sigma_{HBT}}{d^2k_1 dy_1 d^2k_2 dy_2} \sim \delta^2(\mathbf{k}_1 - \mathbf{k}_2) + \delta^2(\mathbf{k}_1 + \mathbf{k}_2), \quad (4.51)$$

in agreement with the result in 4.39. Our present estimate shows that a more careful evaluation of 4.50 would give a smoother peak in $|\mathbf{k}_1 - \mathbf{k}_2|$ at $\mathbf{k}_1 = \mathbf{k}_2$ with the width determined by the inverse radius of the projectile nucleus R_1 .

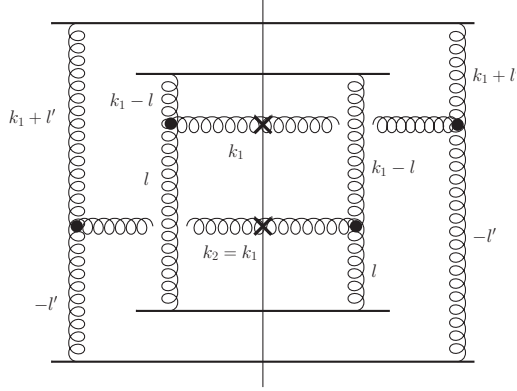


Figure 4.11: An example of a lowest-order diagram generating HBT-type correlations.

The first term on the right-hand-side of 4.51 (or 4.50) has the trademark form of the Hanbury Brown–Twiss (HBT) correlations [97], which are widely studied in heavy ion physics [98–100]. These correlations are normally local both in rapidity ($y_1 = y_2$) and in the transverse momentum $\mathbf{k}_1 = \mathbf{k}_2$: however, in 4.39 (or, in 4.51) we only have locality in transverse momenta. This can be explained by the fact that the extent of the interaction region in the longitudinal direction, commonly labeled R_{long} , is very small in our case due to the extreme Lorentz-contraction of the two colliding nuclei leading to smearing of the longitudinal HBT correlations.

We conclude that the correlations resulting from 4.18 include HBT. Diagrammatic representation of the HBT correlations was discussed earlier in [101]. An example of the diagram giving rise to the correlations in 4.39 is shown in 4.11.

Interestingly though, due to the $\mathbf{k}_2 \leftrightarrow -\mathbf{k}_2$ symmetry of the two-gluon production cross section 4.18, the HBT peak at $\mathbf{k}_1 = \mathbf{k}_2$ in 4.39 is accompanied by an identical peak at $\mathbf{k}_1 = -\mathbf{k}_2$ resulting from $\delta^2(\mathbf{k}_1 + \mathbf{k}_2)$. We thus obtain a back-to-back HBT correlation resulting from multiple rescatterings in nuclei. (The origin of our back-to-back HBT correlations is different from that of the back-to-back HBT-like correlations proposed in [102, 103].)

Note that it is possible that the process of hadronization would affect the phases of the produced gluons, possibly destroying the perturbative HBT correlations of 4.18 and replacing them with the HBT correlations of the non-perturbative origin. The same hadronization process may also destroy the back-to-back HBT correlations from 4.39.

4.3 Summary

In this chapter we calculated the two-gluon production cross section in the heavy-light ion regime. We found that there were two distinct classes of diagrams contributing to the cross section, “separated” and “crossed” diagrams. Analyzing the correlations associated with these processes we found that they only give even harmonics due to the explicit symmetries of the cross section, the $\mathbf{k}_1 \leftrightarrow \mathbf{k}_2$ and $\mathbf{k}_2 \leftrightarrow -\mathbf{k}_2$ symmetries. These correlations also have an enhancement when the two gluons have the same transverse momenta, $\mathbf{k}_1 = \mathbf{k}_2$, and when they have opposite transverse momenta, $\mathbf{k}_1 = -\mathbf{k}_2$. This means that we have equal ridges on the near and away sides

corresponding to peaks at $\Delta\phi = 0$ and $\Delta\phi = \pi$ where $\Delta\phi$ is the azimuthal angle between the two gluons. It should be noted that the theoretical results presented here, the work done by the author and collaborator in [6], predicting an away-side ridge in gluon production were posted on the arXiv before the away-side ridge was discovered by ALICE collaboration in p-Pb collisions at LHC [4].

Chapter 5: Geometric effects and k_T -factorization

After calculating the two-gluon production cross-section and using this to look at the angular dependence of the two-gluon correlation functions in Ch. 4 we now examine a few specific properties of the two-gluon correlation function. We make a prediction for the collision of asymmetric ions (specifically Uranium-Uranium collisions) and show that the saturation framework gives a different result than hydrodynamical simulations. We also derive the k_T -factorized form for the two-gluon production cross section, which allows us to isolate the “HBT” like contributions. This chapter borrows heavily from [7].

5.1 Geometry-dependent correlations

In [6] we pointed out that the geometry of the collision can have an effect on the correlation function, both through the so-called geometric correlations introduced in [6] (Sec. 2.3.2) (see also [104, 105] for a discussion of the role of geometry in di-jet production in $p+p$ collisions) and through a collision geometry-dependent prefactor of the correlator, like that in 4.43. Note also that in the approximation considered, the two-gluon production cross section contains only the even Fourier harmonics in the azimuthal opening angle $\Delta\phi$: it would be important to better understand the effect of geometry on the Fourier expansion coefficients. We know that even Fourier harmonics

in the di-hadron correlators are also generated by the event-averaged hydrodynamics, describing the flow of the quark-gluon plasma. (The odd harmonics are generated by the event-by-event hydrodynamic simulations, including geometry fluctuations [106].) It would be interesting to understand the differences and similarities of the two types of correlations.

Let us concentrate specifically on the elliptic flow observable v_2 , resulting from the 2nd Fourier harmonic of the correlation function. The value of v_2 in the event-averaged hydrodynamics is driven by the ellipticity of the overlap region of the colliding nuclei: the larger the ellipticity, the larger is v_2 . In contrast to this behavior, the non-flow correlations in Eqs. 4.11 and 4.18 do not seem to require any ellipticity at all to produce a second harmonic (and other even harmonics) in the correlator, resulting in the geometry-dependent non-flow contribution to v_2 which is not ellipticity-driven. This can be seen from the lowest-order correlator in 4.43: there the geometry-dependent factor factorizes from the momentum-dependent term which contains the azimuthal angle dependence of the correlations. The strength of the correlations in 4.43 is indeed dependent on the geometry-dependent prefactor: however, it is not *a priori* clear whether this factor depends on the ellipticity of the overlap region.

To elucidate this issue let us consider uranium-uranium ($U + U$) collisions. Data from such collisions have been collected at RHIC, in order to study the properties of hydrodynamic evolution, which predicts stronger elliptic flow (larger v_2) in the side-on-side collisions (bottom panel in 5.1) than in the tip-on-tip collisions (top panel in 5.1), since the ellipticity in the former case is much larger than that in the latter case [107–109].

To compare this with the behavior of the correlations in the CGC dynamics we will employ the lowest-order correlator 4.43. Note that the higher-order corrections to this correlator, which are contained in Eqs. 4.11 and 4.18, are likely to regulate some of the IR singularities present in 4.43, introducing new factors of the saturation scale $Q_{s2}(\mathbf{b})$, which may modify the geometry-dependence of the lowest-order correlator 4.43. However, as we will see below, the power-law IR divergences in 4.43 do not affect the azimuthal angle-dependent correlations; hence our estimate of the magnitude of the Fourier harmonics with index $n \geq 2$ should not be affected qualitatively by higher-order corrections.

To see how the geometry of the collision affects the correlation we take the ratio of two correlation functions which have different geometries associated with the $U + U$ collision illustrated in 5.1: tip-on-tip (top panel) and side-on-side (bottom panel). This requires fixing the impact parameter between the two nuclei, \mathbf{B} , which, in this case, is fixed to $\mathbf{0}$ for both correlations. In the MV model which we have used here $Q_{s2}^2 = 4\pi\alpha_s^2 T_2(\mathbf{b})$. In our case the two nuclei involved in a collision are identical and, hence, have the same nuclear profile functions, $T_1(\mathbf{b}) = T_2(\mathbf{b})$. (Note that, while the gluon production cross section in Eqs. 4.11 and 4.18 was derived in the $A_2 \gg A_1 \gg 1$ limit with $k_1, k_2 \gtrsim Q_{s1}$, the lowest-order correlator 4.43 is valid for $k_1, k_2 \gg Q_{s1}, Q_{s2}$ with the ordering condition relaxed on $A_1, A_2 \gg 1$.) The difference between the two geometries in 5.1 is governed by the nuclear profile function. The ratio between the tip-on-tip and side-on-side correlation functions 4.43 can be written as

$$\frac{C_{tip-on-tip}(\mathbf{k}_1, y_1, \mathbf{k}_2, y_2)|_{LO}}{C_{side-on-side}(\mathbf{k}_1, y_1, \mathbf{k}_2, y_2)|_{LO}} = \frac{\int d^2b [T_{tip-on-tip}(\mathbf{b})]^4}{[\int d^2b [T_{tip-on-tip}(\mathbf{b})]^2]^2} \frac{[\int d^2b [T_{side-on-side}(\mathbf{b})]^2]^2}{\int d^2b [T_{side-on-side}(\mathbf{b})]^4}. \quad (5.1)$$

Note that the momentum dependence cancels out in the ratio of two lowest-order correlators.

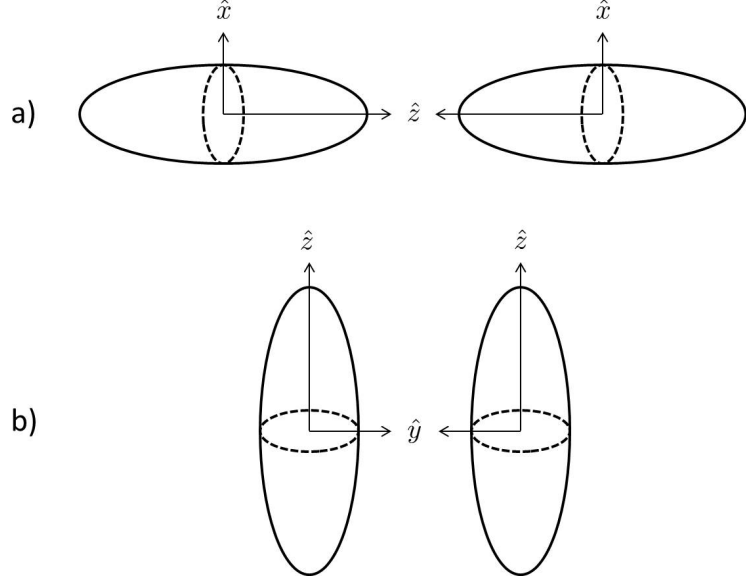


Figure 5.1: The layout of two possible geometries for the $U + U$ collisions. The top panel is the tip-on-tip collision, which has the z -axis of the two nuclei anti-parallel to each other and (anti-)parallel to the collision axis. The bottom diagram is the side-on collision, which has the z -axis of the two nuclei parallel to each other and perpendicular to the collision axis.

For the analytical estimate we are about to perform here we employ a toy model of a uranium nucleus as a prolate spheroid with the Gaussian distribution of the nucleon number density

$$\rho(\vec{r}) = \rho_0 e^{-\frac{x^2}{R^2} - \frac{y^2}{R^2} - \frac{\lambda^2}{R^2} z^2} \quad (5.2)$$

where $\lambda \approx 0.79$ is related to the ellipticity ϵ of the spheroid by $\lambda = \sqrt{1 - \epsilon^2}$. To translate this into a nuclear profile function we integrate over one of the spatial coordinates: z for the tip-on-tip collisions and y for the side-on-side collisions (see

5.1). Thus we have

$$\begin{aligned}
T_{tip-on-tip}(\mathbf{b} = (x, y)) &= \int_{-\infty}^{\infty} dz \rho(\vec{\mathbf{r}}) = \sqrt{\pi} \frac{R}{\lambda} \rho_0 e^{-\frac{b^2}{R^2}} \\
T_{side-on-side}(\mathbf{b} = (z, x)) &= \int_{-\infty}^{\infty} dy \rho(\vec{\mathbf{r}}) = \sqrt{\pi} R \rho_0 e^{-\frac{x^2}{R^2} - \frac{\lambda^2}{R^2} z^2}.
\end{aligned} \tag{5.3}$$

Plugging these results into 5.1 and integrating we arrive at

$$\frac{C_{tip-on-tip}(\mathbf{k}_1, y_1, \mathbf{k}_2, y_2)|_{LO}}{C_{side-on-side}(\mathbf{k}_1, y_1, \mathbf{k}_2, y_2)|_{LO}} = \frac{1}{\lambda} \approx 1.26 \quad (\text{for } U + U). \tag{5.4}$$

Thus a tip-on-tip collision enhances the initial-state (CGC) correlation between two gluons as compared to the side-on-side collision. We have checked this conclusion numerically by using more realistic nuclear density profiles in 5.1, invariably getting stronger correlations in the tip-on-tip versus side-on-side collisions.

We conclude that, at least at the lowest order, the two-gluon correlations behave in an exactly opposite way from hydrodynamics: while hydrodynamic contribution to v_2 is ellipticity-driven, and is hence larger in the side-on-side $U + U$ collisions, the CGC correlations considered here give stronger correlations for the tip-on-tip $U + U$ collisions. This difference in geometry dependence should allow these two effects to be experimentally distinguishable. Further work is needed to understand the geometry dependence of the full correlator resulting from the two-gluon production cross section in Eqs. 4.11 and 4.18.

5.2 k_T -factorization

As discussed in 3.4, there exists a k_T -factorized form of the single-gluon production for heavy-light ion collisions to leading order in saturation of the projectile. This single-gluon production process is slightly different from the two-gluon production

process in heavy-light ion collisions at hand: in obtaining Eqs. 4.11 and 4.18 we considered two gluons originating in the projectile wave function, which could be deemed a “saturation effect” compared to the single gluon needed for quasi-classical gluon production in pA collisions. It appears to be interesting to investigate whether the two-gluon production cross section 4.19 could also be written in a k_T -factorized form.

The distribution functions 3.49 and 3.50 defined in 3.4 are needed for the k_T factorization expression 3.51 of the single gluon production cross-section in pA (or heavy-light ion) collisions. However, when we are dealing with the two-gluon production cross-section 4.19, these distribution functions are likely not to be adequate. First we notice that the only Wilson line operator in the single-gluon production case is the gluon dipole 3.41. In the expression for the two-gluon production cross section 4.19 we have both the quadruple operator 4.16, and the double trace operator 4.21, which would lead to different distribution functions.

Secondly, the two gluon production cross-section has geometric correlations [6] (Sec. 2.3.2), which arise purely from the integration over the impact parameters B , b_1 and b_2 in Eqs. 4.11 and 4.18. This prevents the integrals over the impact parameters from being contained within the distribution functions themselves. This will end up drastically changing the nature of the distribution functions and thus the final factorized form.

The last major difference comes from the ‘crossed’ diagrams. These diagrams contain the interference of the wave functions of the incoming nucleons, which generates a significant “cross-talk” between different parts of the diagram; it is, therefore, *a priori* unlikely that factorization would take place. As we will see below, the factorized form

of the expression cannot be written purely as a convolution of distribution functions without additional factors, like in 3.51. While factorized form can be achieved, it would also contain an extra factor (a “coefficient function”) in the final result for the convolution.

With these considerations in mind we first should take a look at the nature of the distribution functions needed for the k_T -factorized expression for the two-gluon production.

5.2.1 One- and two-gluon distribution functions

As we mentioned above, the impact parameter convolutions in Eqs. 4.11 and 4.18 do not appear to be factorizable into the integral over the distances between the gluons and the projectile and a separate integral over the distances between the gluons and the target, in stark contrast to the single-gluon production case [80, 82]. Therefore, any factorization expression we could obtain for the two-gluon production has to have an explicit convolution over the impact parameters. Therefore, we first need to rewrite the single-gluon distribution functions introduced above for the fixed impact parameter. We can easily recast Eqs. 3.49 and 3.50 as

$$\left\langle \frac{d\phi_{A_1}(\mathbf{q}, y)}{d^2b} \right\rangle_{A_1} = \frac{C_F}{\alpha_s(2\pi)^3} \int d^2r e^{-i\mathbf{q}\cdot\mathbf{r}} \nabla_{\mathbf{r}}^2 n_G(\mathbf{b} + \mathbf{r}, \mathbf{b}, y) \quad (5.5)$$

and

$$\left\langle \frac{d\phi_{A_2}(\mathbf{q}, y)}{d^2b} \right\rangle_{A_2} = \frac{C_F}{\alpha_s(2\pi)^3} \int d^2r e^{-i\mathbf{q}\cdot\mathbf{r}} \nabla_{\mathbf{r}}^2 N_G(\mathbf{b} + \mathbf{r}, \mathbf{b}, y). \quad (5.6)$$

Since now these distribution functions fix both the momentum of the gluon \mathbf{q} and its (approximate) position in the transverse coordinate space \mathbf{b} , along with its rapidity y specifying the value of Bjorken- x variable, we identify the differential unintegrated

gluon distribution functions in Eqs. 5.5 and 5.6 with the Wigner distribution [110] for gluons (see [18,111] and references therein for applications of Wigner distributions in perturbative QCD).

Here we introduce two different distribution functions which are associated with the two Wilson line operators entering the two-gluon production cross-section 4.19, the gluon quadrupole and the double-trace operators. The two-gluon distribution function associated with the gluon double-trace operator is

$$\left\langle \frac{d\phi_{A_2}^D(\mathbf{q}_1, \mathbf{q}_2, y)}{d^2b_1 d^2b_2} \right\rangle_{A_2} = \left(\frac{C_F}{\alpha_s(2\pi)^3} \right)^2 \int d^2r_1 d^2r_2 e^{-i\mathbf{q}_1 \cdot \mathbf{r}_1 - i\mathbf{q}_2 \cdot \mathbf{r}_2} \quad (5.7)$$

$$\times \nabla_{\mathbf{r}_1}^2 \nabla_{\mathbf{r}_2}^2 N_D(\mathbf{b}_1 + \mathbf{r}_1, \mathbf{b}_1, \mathbf{b}_2 + \mathbf{r}_2, \mathbf{b}_2, y),$$

where

$$N_D(\mathbf{x}, \mathbf{y}, \mathbf{z}, \mathbf{w}, Y) = \frac{1}{(N_c^2 - 1)^2} \langle \text{Tr} [\mathbb{1} - U_{\mathbf{x}} U_{\mathbf{y}}^\dagger] \text{Tr} [\mathbb{1} - U_{\mathbf{z}} U_{\mathbf{w}}^\dagger] \rangle_{A_2} (Y). \quad (5.8)$$

The correlator N_D is illustrated diagrammatically in the top panel of Fig. 5.2 for the quasi-classical approximation. The distribution function 5.7 gives us the number density for pairs of gluons, with the transverse momenta $\mathbf{q}_1, \mathbf{q}_2$ and positions $\mathbf{b}_1, \mathbf{b}_2$ of the gluons fixed and with the rapidity of both gluons being close to y (up to $\ll 1/\alpha_s$ variations): we can think of this distribution function as a two-gluon Wigner distribution.

The distribution function associated with the gluon quadrupole operator is

$$\left\langle \frac{d\phi_{A_2}^Q(\mathbf{q}_1, \mathbf{q}_2, y)}{d^2b_1 d^2b_2} \right\rangle_{A_2} = \left(\frac{C_F}{\alpha_s(2\pi)^3} \right)^2 \int d^2r_1 d^2r_2 e^{-i\mathbf{q}_1 \cdot \mathbf{r}_1 - i\mathbf{q}_2 \cdot \mathbf{r}_2} \quad (5.9)$$

$$\times \nabla_{\mathbf{r}_1}^2 \nabla_{\mathbf{r}_2}^2 N_Q(\mathbf{b}_1 + \mathbf{r}_1, \mathbf{b}_1, \mathbf{b}_2 + \mathbf{r}_2, \mathbf{b}_2, y)$$

with

$$N_Q(\mathbf{x}, \mathbf{y}, \mathbf{z}, \mathbf{w}, Y) = \frac{1}{N_c^2 - 1} \langle \text{Tr} [(\mathbb{1} - U_{\mathbf{x}} U_{\mathbf{y}}^\dagger) (\mathbb{1} - U_{\mathbf{z}} U_{\mathbf{w}}^\dagger)] \rangle_{A_2} (Y). \quad (5.10)$$

The definition 5.9 is illustrated diagrammatically in the lower panel of Fig. 5.2 in the quasi-classical approximation. The object defined in 5.9 can, similar to 5.7, be thought of as a (different) two-gluon Wigner distribution.

Notice how both the two-dipole 5.7 and quadrupole 5.9 two-gluon distribution are composed of Wilson line operators. This is natural for distribution functions entering production cross section, since in high energy scattering all cross sections are expressed in terms of Wilson lines. This is in exact parallel to the single-gluon distribution 5.6, which is related to the adjoint dipole operator. Note that since the single-gluon production cross section depends only on the adjoint dipole operator, one can express it only in terms of the single-gluon distribution 3.50. For the two-gluon production 4.19, which contains both the double-trace and quadrupole operators, we end up with two different two-gluon distributions 5.7 and 5.9.

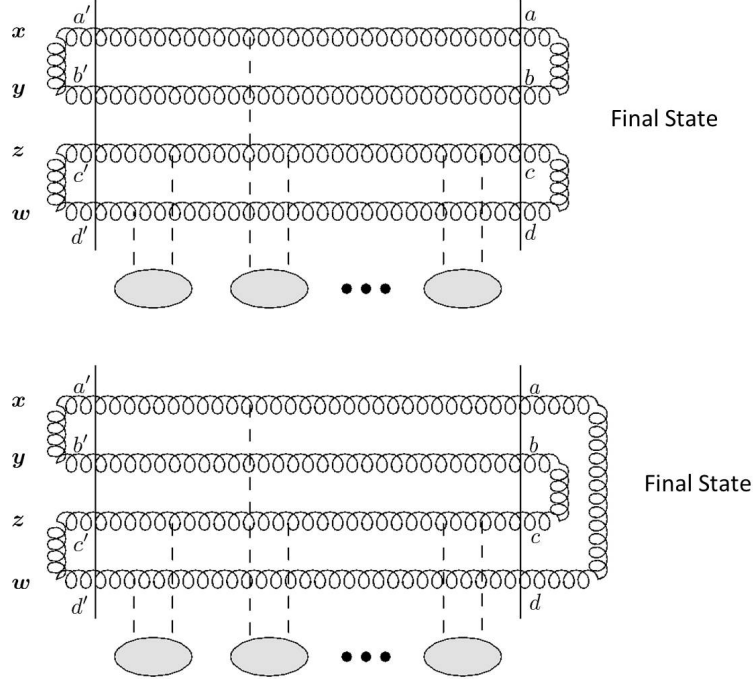


Figure 5.2: The top panel represents the forward amplitude for the scattering of two gluon dipoles on a target nucleus in the quasi-classical approximation: this is an essential contribution to the definition of the two-gluon distribution in 5.7. The bottom panel represents the quadrupole scattering on the target, as in the definition of the two-gluon distribution in 5.9. The vectors \mathbf{x} , \mathbf{y} , \mathbf{z} , and \mathbf{w} label the positions of the two-gluon distribution in 5.9. The vertical solid lines denote the initial (left) and final (right) states. The final state of the gluons is labeled to stress that the difference between the two panels is in the color configurations of the final state.

There is also an alternative single-gluon distribution, the so-called Weizsäcker-Williams (WW) distribution [79, 80, 83, 112], which was found to be related to the $q\bar{q}$ back-to-back jet production in DIS [113]. In the quasi-classical MV picture the Weizsäcker-Williams two-gluon distribution, given by the correlator of four different gluon fields, would simply factorize into a product of two single-gluon WW distributions. It is possible, however, that beyond the quasi-classical limit the two-gluon WW distribution (properly defined in terms of Wilson line operators along the lines

of the single-gluon WW distribution from [113]) would constitute an independent new object, related to some observables. Investigating this possibility further is beyond the scope of this work.

Since there exists more experience in the field with dipole distribution functions 5.6, it would be nice to be able to write the two-gluon distributions 5.7 and 5.9 as combinations of dipole distributions. Unfortunately this is not possible in general; however each distribution does contain a piece that can be written in terms of dipole distributions.

The most obvious is the double-trace two-gluon distribution function 5.7. Since in the large- N_c limit

$$N_D(\mathbf{x}, \mathbf{y}, \mathbf{z}, \mathbf{w}) \Big|_{\text{large-}N_c} = N_G(\mathbf{x}, \mathbf{y}) N_G(\mathbf{z}, \mathbf{w}) \quad (5.11)$$

with $N_G = 1 - S_G$, we can see by plugging this result into 5.7 and comparing to 5.6 that

$$\left\langle \frac{d\phi_{A_2}^D(\mathbf{q}_1, \mathbf{q}_2, y)}{d^2b_1 d^2b_2} \right\rangle_{A_2} \Big|_{\text{large-}N_c} = \left\langle \frac{d\phi_{A_2}(\mathbf{q}_1, y)}{d^2b_1} \right\rangle_{A_2} \left\langle \frac{d\phi_{A_2}(\mathbf{q}_2, y)}{d^2b_2} \right\rangle_{A_2}. \quad (5.12)$$

The double-trace two-gluon distribution function factorizes into two dipole distribution functions only in the large- N_c limit. Unfortunately, the only correlations left in the two-gluon production cross section 4.19 evaluated in the large- N_c limit are the geometric correlations [6] (Sec. 2.3.2). All of the other correlations contained in 4.19 are subleading in N_c ; for instance, the correlations 4.43 are explicitly $\mathcal{O}(1/N_c^2)$.

In order to isolate the dipole contribution to the two-gluon quadrupole distribution 5.9 we cannot just take the large- N_c limit like we did for the singlet distribution. (In addition the whole corresponding contribution to the cross section 4.18 is $\mathcal{O}(1/N_c^2)$ when compared to 4.11.) Instead we can single out the part of the two-gluon

quadrupole distribution which is expressible in terms of single-gluon dipole distributions: we will show later that this is exactly the part that gives rise to the early-time Hanbury-Brown–Twiss (HBT) correlations [97] discussed in [6] (Sec. 4.2).

First let us analyze the quadrupole operator (cf. 4.16)

$$\begin{aligned} Q(\mathbf{x}, \mathbf{y}, \mathbf{z}, \mathbf{w}, Y) &= \frac{1}{N_c^2 - 1} \langle \text{Tr} [U_{\mathbf{x}} U_{\mathbf{y}}^\dagger U_{\mathbf{z}} U_{\mathbf{w}}^\dagger] \rangle_{A_2} (Y) \\ &= \frac{1}{N_c^2 - 1} \left\langle \delta^{ad} \delta^{bc} U_{\mathbf{x}}^{aa'} U_{\mathbf{y}}^{bb'} U_{\mathbf{z}}^{cc'} U_{\mathbf{w}}^{dd'} \delta^{a'b'} \delta^{c'd'} \right\rangle_{A_2} (Y). \end{aligned} \quad (5.13)$$

Here we have written out the color structure implied by the trace notation in terms of the adjoint color indices a, b, c, d (and the corresponding primed variables) shown in the lower panel of Fig. 5.2. The four gluon lines in the final state in Fig. 5.2 carrying indices a, b, c, d are in a net color-neutral state. This allows us to classify the color states in the quadrupole operator by the color states of the two gluons with indices a and b . Choosing the color state of gluons a and b sets the color state of gluons c and d due to the color neutrality of all four gluons in the final state. The same applies to the initial state gluons with the color indices $a', b', c',$ and d' .

A pair of gluons may be found in either of the following irreducible representations of $\text{SU}(N_c)$

$$\begin{aligned} (N_c^2 - 1) \otimes (N_c^2 - 1) &= V_1 \oplus V_2 \oplus V_3 \oplus V_4 \oplus V_5 \oplus V_6 \oplus V_7 \\ &= \mathbf{1} \oplus (N_c^2 - 1) \oplus \frac{N_c^2(N_c - 3)(N_c + 1)}{4} \oplus \frac{N_c^2(N_c + 3)(N_c - 1)}{4} \\ &\oplus (N_c^2 - 1) \oplus \frac{(N_c^2 - 1)(N_c^2 - 4)}{4} \oplus \frac{(N_c^2 - 1)(N_c^2 - 4)}{4}. \end{aligned} \quad (5.14)$$

In A.2 we follow the notation for the irreducible representations introduced in [114], see page 120 there. We will, however, use a different normalization scheme from the projection operators P_i^{abcd} 's. We normalize the states such that $P_i^{abcd} P_i^{abcd} = 1$ (summation over repeated indices is implied), which implies, due to the orthonormality of

the projection operators,

$$\mathbb{1}^{abcd, a'b'c'd'} = \sum_{i=1}^7 P_i^{abcd} P_i^{a'b'c'd'}. \quad (5.15)$$

The only projection operator we need to know explicitly for the following calculation is the singlet projector,

$$P_1^{abcd} = \frac{1}{N_c^2 - 1} \delta^{ab} \delta^{cd}. \quad (5.16)$$

Using the singlet projection and the unit operator 5.15 we can rewrite 5.13 as (dropping the A_2 subscript and not showing rapidity dependence for brevity)

$$\frac{1}{N_c^2 - 1} \langle \text{Tr} [U_{\mathbf{x}} U_{\mathbf{y}}^\dagger U_{\mathbf{z}} U_{\mathbf{w}}^\dagger] \rangle = \sum_{i=1}^7 P_i^{a''b''b'a''} \left\langle P_i^{abcd} U_{\mathbf{x}}^{aa'} U_{\mathbf{y}}^{bb'} U_{\mathbf{z}}^{cc'} U_{\mathbf{w}}^{dd'} P_1^{a'b'c'd'} \right\rangle. \quad (5.17)$$

We can isolate the part that gives the factorized dipole contribution in the sum of 5.17. This contribution comes from the large- N_c part of the double-dipole operator, which, in turn, originates in the P_1 -term in the sum in 5.17. Isolating the double trace operator from the rest of the expression in 5.17 we arrive at

$$\begin{aligned} \frac{1}{N_c^2 - 1} \langle \text{Tr} [U_{\mathbf{x}} U_{\mathbf{y}}^\dagger U_{\mathbf{z}} U_{\mathbf{w}}^\dagger] \rangle &= \frac{1}{(N_c^2 - 1)^2} \langle \text{Tr} [U_{\mathbf{x}} U_{\mathbf{y}}^\dagger] \text{Tr} [U_{\mathbf{z}} U_{\mathbf{w}}^\dagger] \rangle \\ &+ \sum_{i=2}^7 P_i^{a''b''b'a''} \left\langle P_i^{abcd} U_{\mathbf{x}}^{aa'} U_{\mathbf{y}}^{bb'} U_{\mathbf{z}}^{cc'} U_{\mathbf{w}}^{dd'} P_1^{a'b'c'd'} \right\rangle. \end{aligned} \quad (5.18)$$

The double trace operator comes with a prefactor of $\frac{1}{(N_c^2 - 1)^2}$, which means that when we combine 5.18 with 5.10 we arrive at

$$N_Q(\mathbf{x}, \mathbf{y}, \mathbf{z}, \mathbf{w}) = N_G(\mathbf{x}, \mathbf{y}) N_G(\mathbf{z}, \mathbf{w}) + \dots. \quad (5.19)$$

The ellipses in 5.19 represent the remaining contributions which are not contained in the factorized gluon dipoles, the P_2 through P_7 terms and the sub-leading in N_c

terms from the double trace operator in 5.18. Plugging 5.19 into 5.9 we arrive at

$$\left\langle \frac{d\phi_{A_2}^Q(\mathbf{q}_1, \mathbf{q}_2, y)}{d^2b_1 d^2b_2} \right\rangle_{A_2} = \left\langle \frac{d\phi_{A_2}(\mathbf{q}_1, y)}{d^2b_1} \right\rangle_{A_2} \left\langle \frac{d\phi_{A_2}(\mathbf{q}_2, y)}{d^2b_2} \right\rangle_{A_2} + \dots, \quad (5.20)$$

where we have isolated the factorized dipole distributions from the rest of the expression. Let us stress that the terms represented by ellipsis in 5.20 are not suppressed by any parameter involved in the problem: these corrections are comparable to the term shown explicitly on the right of 5.20. Hence even if we took the leading- N_c limit of the two-gluon quadrupole distribution there would still be terms that would not be contained inside the two factorized gluon distributions of 5.20.

5.2.2 Derivation of the factorized forms

Now that we have defined the necessary distribution functions we can start constructing the factorized form of the two-gluon production cross-section. Each of the parts of the cross section 4.19 given by Eqs. 4.11 and 4.18 factorizes differently.

The easiest case to factorize, and thus the first one we will cover, is the 'square' diagram component 4.11. Separating the transverse vectors associated with either one of the valence quarks and emitted gluons, we can write 4.11 in the following form,

$$\begin{aligned} \frac{d\sigma_{square}}{d^2k_1 dy_1 d^2k_2 dy_2} &= \frac{\alpha_s^2 C_F^2}{16 \pi^8} \int d^2B \\ &\times \left\langle \int d^2x_1 d^2y_1 d^2b_1 T_1(\mathbf{B} - \mathbf{b}_1) e^{-i \mathbf{k}_1 \cdot (\mathbf{x}_1 - \mathbf{y}_1)} \frac{\mathbf{x}_1 - \mathbf{b}_1}{|\mathbf{x}_1 - \mathbf{b}_1|^2} \cdot \frac{\mathbf{y}_1 - \mathbf{b}_1}{|\mathbf{y}_1 - \mathbf{b}_1|^2} \right. \\ &\times \left(\frac{1}{N_c^2 - 1} \text{Tr}[U_{\mathbf{x}_1} U_{\mathbf{y}_1}^\dagger] - \frac{1}{N_c^2 - 1} \text{Tr}[U_{\mathbf{x}_1} U_{\mathbf{b}_1}^\dagger] - \frac{1}{N_c^2 - 1} \text{Tr}[U_{\mathbf{b}_1} U_{\mathbf{y}_1}^\dagger] + 1 \right) \\ &\times \int d^2x_2 d^2y_2 d^2b_2 T_1(\mathbf{B} - \mathbf{b}_2) e^{-i \mathbf{k}_2 \cdot (\mathbf{x}_2 - \mathbf{y}_2)} \frac{\mathbf{x}_2 - \mathbf{b}_2}{|\mathbf{x}_2 - \mathbf{b}_2|^2} \cdot \frac{\mathbf{y}_2 - \mathbf{b}_2}{|\mathbf{y}_2 - \mathbf{b}_2|^2} \\ &\times \left. \left(\frac{1}{N_c^2 - 1} \text{Tr}[U_{\mathbf{x}_2} U_{\mathbf{y}_2}^\dagger] - \frac{1}{N_c^2 - 1} \text{Tr}[U_{\mathbf{x}_2} U_{\mathbf{b}_2}^\dagger] - \frac{1}{N_c^2 - 1} \text{Tr}[U_{\mathbf{b}_2} U_{\mathbf{y}_2}^\dagger] + 1 \right) \right\rangle_{A_2}. \end{aligned} \quad (5.21)$$

Notice that the first two lines in 5.21 are the only two lines that contain the variables \mathbf{x}_1 , \mathbf{y}_1 , \mathbf{b}_1 , while the next two lines are the only ones that contain the variables \mathbf{x}_2 , \mathbf{y}_2 , \mathbf{b}_2 . In the limit we are dealing with \mathbf{x}_1 , \mathbf{y}_1 , \mathbf{b}_1 are perturbatively close to each other. Since $T_1(\mathbf{b})$ is slowly varying it is approximately constant over perturbatively short scales. Thus we can make the approximation

$$T_1(\mathbf{B} - \mathbf{b}_1) \approx T_1(\mathbf{B} - \mathbf{x}_1) \approx T_1(\mathbf{B} - \mathbf{y}_1). \quad (5.22)$$

This same approximation also applies to \mathbf{x}_2 , \mathbf{y}_2 , \mathbf{b}_2 . Notice that the second line of 5.21 has four different terms in the parentheses, each of which is at most a function of two of the three variables \mathbf{x}_1 , \mathbf{y}_1 , \mathbf{b}_1 . Combining this fact with the approximation 5.22 we can perform one of the \mathbf{x}_1 , \mathbf{y}_1 , \mathbf{b}_1 integrals over a different variable for each term in the second line depending on which variable is not in the trace. A similar thing is done with the \mathbf{x}_2 , \mathbf{y}_2 , \mathbf{b}_2 integral. After doing this and integrating by parts we arrive at

$$\begin{aligned} \frac{d\sigma_{square}}{d^2k_1 dy_1 d^2k_2 dy_2} &= \frac{\alpha_s^2 C_F^2}{4\pi^6} \frac{1}{\mathbf{k}_1^2 \mathbf{k}_2^2} \int d^2B d^2b_1 d^2b_2 d^2x_1 d^2x_2 T_1(\mathbf{B} - \mathbf{b}_1) T_1(\mathbf{B} - \mathbf{b}_2) \\ &\times e^{-i\mathbf{k}_1 \cdot (\mathbf{x}_1 - \mathbf{b}_1) - i\mathbf{k}_2 \cdot (\mathbf{x}_2 - \mathbf{b}_2)} \ln \left(\frac{1}{|\mathbf{x}_1 - \mathbf{b}_1| \Lambda} \right) \ln \left(\frac{1}{|\mathbf{x}_2 - \mathbf{b}_2| \Lambda} \right) \\ &\times \nabla_{\mathbf{x}_1}^2 \nabla_{\mathbf{x}_2}^2 \frac{1}{(N_c^2 - 1)^2} \left\langle \text{Tr} \left[\mathbb{1} - U_{\mathbf{x}_1} U_{\mathbf{b}_1}^\dagger \right] \text{Tr} \left[\mathbb{1} - U_{\mathbf{x}_2} U_{\mathbf{b}_2}^\dagger \right] \right\rangle_{A_2}. \end{aligned} \quad (5.23)$$

From here we can manipulate this expression into a form reminiscent of 3.51 but not quite the same. As mentioned in the discussion at the beginning of Sec. 5.2, the integrals over the impact parameters cannot be absorbed into the distribution functions. This is now manifest in 5.23: we have three integrals (over \mathbf{B} , \mathbf{b}_1 and \mathbf{b}_2) and four impact parameter-related distances ($\mathbf{B} - \mathbf{b}_1$, $\mathbf{B} - \mathbf{b}_2$, \mathbf{b}_1 and \mathbf{b}_2). We conclude that we must use the new distribution functions defined in Eqs. 5.5 and

5.7 while convoluting them over the impact parameters \mathbf{B} , \mathbf{b}_1 and \mathbf{b}_2 . Employing Eqs. 5.5 and 5.7 we can rewrite the 'square' diagrams contribution to the two-gluon production cross section 4.11 in the factorized form

$$\begin{aligned} \frac{d\sigma_{square}}{d^2k_1 dy_1 d^2k_2 dy_2} &= \left(\frac{2\alpha_s}{C_F} \right)^2 \frac{1}{k_1^2 k_2^2} \int d^2B d^2b_1 d^2b_2 \int d^2q_1 d^2q_2 \\ &\times \left\langle \frac{d\phi_{A_1}(\mathbf{q}_1, y=0)}{d^2(\mathbf{B}-\mathbf{b}_1)} \right\rangle_{A_1} \left\langle \frac{d\phi_{A_1}(\mathbf{q}_2, y=0)}{d^2(\mathbf{B}-\mathbf{b}_2)} \right\rangle_{A_1} \\ &\times \left\langle \frac{d\phi_{A_2}^D(\mathbf{q}_1-\mathbf{k}_1, \mathbf{q}_2-\mathbf{k}_2, y \approx y_1 \approx y_2)}{d^2b_1 d^2b_2} \right\rangle_{A_2}. \end{aligned} \quad (5.24)$$

The asymmetry in rapidity arguments of the distribution entering 5.24 is due to the fact that the projectile in the original 4.11 was treated in the lowest-order quasi-classical approximation, while the whole non-linear evolution [26–33] is included in the rapidity interval between the produced gluons and the target by the use of the Wilson lines. As mentioned previously, 5.24 is similar to 3.51 but has a few key differences. 3.51 employs unintegrated gluon distributions (gluon transverse momentum distributions (TMDs)), while 5.24 uses one- and two-gluon Wigner distributions. Related to that, in 3.51 the convolution happens only over transverse momentum, while 5.24 also contains integrals over impact parameters \mathbf{B} , \mathbf{b}_1 , and \mathbf{b}_2 .

One may also note that 5.24 is not target-projectile symmetric: the target is described by a single two-gluon distribution, while the projectile is represented by two single-gluon distributions. In contrast, 3.51 is completely target-projectile symmetric. In fact, 3.51 is often generalized to the case of nucleus–nucleus (AA) collisions by using 3.50 for both unintegrated gluon distributions in it. While such generalization allows for successful phenomenology (see e.g. [57]), it is theoretically not justified below the saturation scales of both nuclei. Moreover, there is numerical evidence [55] demonstrating that the k_T -factorization formula 3.51 is not valid in AA collisions.

Therefore, it appears that the apparent target-projectile symmetry of 3.51 is, in fact, somewhat misleading: the equation was derived in the limit where the projectile is dilute, while the target may or may not be dense, leading to the difference in the definitions of the unintegrated gluon distributions of the target and the projectile in Eqs. 3.49 and 3.50. It is likely that 3.51 is not valid for dense-dense scattering [55], and is thus not truly target-projectile symmetric due to the underlying assumptions.

With the 'square' diagrams contribution to the cross section cast in a factorized form we now turn our attention to the 'crossed' diagrams contribution 4.18. It is helpful to write out the crossed diagrams part of the cross section, 4.18, in the following form,

$$\begin{aligned}
\frac{d\sigma_{crossed}}{d^2k_1 dy_1 d^2k_2 dy_2} &= \frac{\alpha_s^2 C_F^2}{16 \pi^8} \int d^2B \left\langle \int d^2x_1 d^2y_1 d^2b_1 T_1(\mathbf{B} - \mathbf{b}_1) e^{-i \mathbf{k}_1 \cdot \mathbf{x}_1 + i \mathbf{k}_2 \cdot \mathbf{y}_1} \right. \\
&\times \left[\frac{\mathbf{x}_1 - \mathbf{b}_1}{|\mathbf{x}_1 - \mathbf{b}_1|^2} \right]_i \left[\frac{\mathbf{y}_1 - \mathbf{b}_1}{|\mathbf{y}_1 - \mathbf{b}_1|^2} \right]_j \frac{1}{N_c^2 - 1} \left[U_{\mathbf{x}_1} U_{\mathbf{y}_1}^\dagger - U_{\mathbf{x}_1} U_{\mathbf{b}_1}^\dagger - U_{\mathbf{b}_1} U_{\mathbf{y}_1}^\dagger + \mathbb{1} \right]^{ab} \\
&\times \int d^2x_2 d^2y_2 d^2b_2 T_1(\mathbf{B} - \mathbf{b}_2) e^{-i \mathbf{k}_2 \cdot \mathbf{x}_2 + i \mathbf{k}_1 \cdot \mathbf{y}_2} \left[\frac{\mathbf{x}_2 - \mathbf{b}_2}{|\mathbf{x}_2 - \mathbf{b}_2|^2} \right]_j \left[\frac{\mathbf{y}_2 - \mathbf{b}_2}{|\mathbf{y}_2 - \mathbf{b}_2|^2} \right]_i \\
&\times \frac{1}{N_c^2 - 1} \left[U_{\mathbf{x}_2} U_{\mathbf{y}_2}^\dagger - U_{\mathbf{x}_2} U_{\mathbf{b}_2}^\dagger - U_{\mathbf{b}_2} U_{\mathbf{y}_2}^\dagger + \mathbb{1} \right]^{ba} \Bigg\rangle_{A_2} + (\mathbf{k}_2 \rightarrow -\mathbf{k}_2), \quad (5.25)
\end{aligned}$$

where $i, j = 1, 2$ are transverse vector indices and $a, b = 1, \dots, N_c^2 - 1$ are adjoint color indices, with summation assumed over repeated indices. Here we have again separated the terms that depend on $\mathbf{x}_1, \mathbf{y}_1, \mathbf{b}_1$ from the terms that depend on $\mathbf{x}_2, \mathbf{y}_2, \mathbf{b}_2$. Using the same trick we employed when factorizing the 'square' diagrams contribution, we evaluate the $\mathbf{x}_1, \mathbf{y}_1, \mathbf{b}_1$, and $\mathbf{x}_2, \mathbf{y}_2, \mathbf{b}_2$ integrals piece by piece arriving at (after transverse vector relabeling)

$$\begin{aligned}
\frac{d\sigma_{crossed}}{d^2k_1 dy_1 d^2k_2 dy_2} &= \frac{\alpha_s^2 C_F^2}{4 \pi^6} \int d^2B d^2b_1 d^2b_2 d^2x_1 d^2x_2 T_1(\mathbf{B} - \mathbf{b}_1) T_1(\mathbf{B} - \mathbf{b}_2) \\
&\times \left\{ \frac{1}{2} \delta_{ij} \ln \left(\frac{1}{|\mathbf{x}_1 - \mathbf{b}_1| \Lambda} \right) - \frac{[\mathbf{x}_1 - \mathbf{b}_1]_i [\mathbf{x}_1 - \mathbf{b}_1]_j}{2 |\mathbf{x}_1 - \mathbf{b}_1|^2} - i \left[\frac{\mathbf{k}_1}{k_1^2} \right]_i \left[\frac{\mathbf{x}_1 - \mathbf{b}_1}{|\mathbf{x}_1 - \mathbf{b}_1|^2} \right]_j \right. \\
&- i \left. \left[\frac{\mathbf{x}_1 - \mathbf{b}_1}{|\mathbf{x}_1 - \mathbf{b}_1|^2} \right]_i \left[\frac{\mathbf{k}_2}{k_2^2} \right]_j \right\} \left\{ \frac{1}{2} \delta_{ij} \ln \left(\frac{1}{|\mathbf{x}_2 - \mathbf{b}_2| \Lambda} \right) - \frac{[\mathbf{x}_2 - \mathbf{b}_2]_i [\mathbf{x}_2 - \mathbf{b}_2]_j}{2 |\mathbf{x}_2 - \mathbf{b}_2|^2} \right. \\
&- i \left. \left[\frac{\mathbf{k}_1}{k_1^2} \right]_i \left[\frac{\mathbf{x}_2 - \mathbf{b}_2}{|\mathbf{x}_2 - \mathbf{b}_2|^2} \right]_j - i \left[\frac{\mathbf{x}_2 - \mathbf{b}_2}{|\mathbf{x}_2 - \mathbf{b}_2|^2} \right]_i \left[\frac{\mathbf{k}_2}{k_2^2} \right]_j \right\} e^{-i \mathbf{k}_1 \cdot (\mathbf{x}_1 - \mathbf{b}_2) - i \mathbf{k}_2 \cdot (\mathbf{x}_2 - \mathbf{b}_1)} \\
&\times \frac{1}{(N_c^2 - 1)^2} \left\langle \text{Tr} \left[\left(\mathbb{1} - U_{\mathbf{x}_1} U_{\mathbf{b}_1}^\dagger \right) \left(\mathbb{1} - U_{\mathbf{x}_2} U_{\mathbf{b}_2}^\dagger \right) \right] \right\rangle_{A_2} + (\mathbf{k}_2 \rightarrow -\mathbf{k}_2), \quad (5.26)
\end{aligned}$$

where we have employed

$$\int d^2b \left[\frac{\mathbf{x} - \mathbf{b}}{|\mathbf{x} - \mathbf{b}|^2} \right]_i \left[\frac{\mathbf{y} - \mathbf{b}}{|\mathbf{y} - \mathbf{b}|^2} \right]_j = \pi \left\{ \delta_{ij} \ln \left(\frac{1}{|\mathbf{x} - \mathbf{y}| \Lambda} \right) - \frac{[\mathbf{x} - \mathbf{y}]_i [\mathbf{x} - \mathbf{y}]_j}{|\mathbf{x} - \mathbf{y}|^2} \right\} \quad (5.27)$$

along with other, more common, two-dimensional integrals (see, e.g., Appendix A.2 of [23] for a list of useful integrals).

To proceed we rewrite 5.26 as

$$\begin{aligned}
\frac{d\sigma_{crossed}}{d^2k_1 dy_1 d^2k_2 dy_2} &= \frac{\alpha_s^2 C_F^2}{4^3 \pi^6} \frac{1}{k_1^4 k_2^4} \int d^2B d^2b_1 d^2b_2 d^2x_1 d^2x_2 e^{-i \mathbf{k}_1 \cdot (\mathbf{x}_1 - \mathbf{b}_2) - i \mathbf{k}_2 \cdot (\mathbf{x}_2 - \mathbf{b}_1)} \\
&\times \left\{ \left[\overleftarrow{\nabla}_{x_1}^2 \overleftarrow{\nabla}_{b_1}^2 \nabla_{x_1}^i \nabla_{x_1}^j + \overleftarrow{\nabla}_{b_1}^2 \overleftarrow{\nabla}_{x_1}^i \nabla_{x_1}^j \nabla_{x_1}^2 - \overleftarrow{\nabla}_{x_1}^2 \overleftarrow{\nabla}_{b_1}^j \nabla_{x_1}^i \nabla_{x_1}^2 \right] \right. \\
&\quad \times (\mathbf{x}_1 - \mathbf{b}_1)^2 \ln \left(\frac{1}{|\mathbf{x}_1 - \mathbf{b}_1| \Lambda} \right) T_1(\mathbf{B} - \mathbf{b}_1) \left. \right\} \\
&\times \left\{ \left[\overleftarrow{\nabla}_{x_2}^2 \overleftarrow{\nabla}_{b_2}^2 \nabla_{x_2}^i \nabla_{x_2}^j - \overleftarrow{\nabla}_{x_2}^2 \overleftarrow{\nabla}_{b_2}^i \nabla_{x_2}^j \nabla_{x_2}^2 + \overleftarrow{\nabla}_{b_2}^2 \overleftarrow{\nabla}_{x_2}^j \nabla_{x_2}^i \nabla_{x_2}^2 \right] \right. \\
&\quad \times (\mathbf{x}_2 - \mathbf{b}_2)^2 \ln \left(\frac{1}{|\mathbf{x}_2 - \mathbf{b}_2| \Lambda} \right) T_1(\mathbf{B} - \mathbf{b}_2) \left. \right\} \\
&\times \frac{1}{(N_c^2 - 1)^2} \left\langle \text{Tr} \left[\left(\mathbb{1} - U_{\mathbf{x}_1} U_{\mathbf{b}_1}^\dagger \right) \left(\mathbb{1} - U_{\mathbf{x}_2} U_{\mathbf{b}_2}^\dagger \right) \right] \right\rangle_{A_2} + (\mathbf{k}_2 \rightarrow -\mathbf{k}_2), \quad (5.28)
\end{aligned}$$

where ∇ 's denote transverse coordinate derivatives and the left arrow over ∇ indicates that the derivative is acting on the exponential to the left of the curly brackets.

Notice the non-trivial transverse index structure in 5.28: this drastically alters the factorized form of the expression, as compared to, say, 5.24. Inverting Fourier

transforms in Eqs. 5.5 and 5.9, employing 3.46, and substituting the results into 5.28 yields, after a fair bit of algebra,

$$\begin{aligned}
\frac{d\sigma_{crossed}}{d^2k_1 dy_1 d^2k_2 dy_2} &= \left(\frac{2\alpha_s}{C_F}\right)^2 \frac{1}{k_1^2 k_2^2} \int d^2B d^2b_1 d^2b_2 \int d^2q_1 d^2q_2 \\
&\times \frac{\mathcal{K}(\mathbf{b}_1, \mathbf{b}_2, \mathbf{k}_1, \mathbf{k}_2, \mathbf{q}_1, \mathbf{q}_2)}{N_c^2 - 1} \left\langle \frac{d\phi_{A_1}(\mathbf{q}_1, y=0)}{d^2(\mathbf{B} - \mathbf{b}_1)} \right\rangle_{A_1} \left\langle \frac{d\phi_{A_1}(\mathbf{q}_2, y=0)}{d^2(\mathbf{B} - \mathbf{b}_2)} \right\rangle_{A_1} \\
&\times \left\langle \frac{d\phi_{A_2}^Q(\mathbf{k}_1 - \mathbf{q}_1, \mathbf{k}_2 - \mathbf{q}_2, y \approx y_1 \approx y_2)}{d^2b_1 d^2b_2} \right\rangle_{A_2} + (\mathbf{k}_2 \rightarrow -\mathbf{k}_2), \tag{5.29}
\end{aligned}$$

where the ‘‘coefficient function’’ is defined as

$$\begin{aligned}
\mathcal{K}(\mathbf{b}_1, \mathbf{b}_2, \mathbf{k}_1, \mathbf{k}_2, \mathbf{q}_1, \mathbf{q}_2) &= \frac{1}{q_1^2 q_2^2 (\mathbf{k}_1 - \mathbf{q}_1)^2 (\mathbf{k}_2 - \mathbf{q}_2)^2} e^{-i(\mathbf{k}_1 - \mathbf{k}_2) \cdot (\mathbf{b}_1 - \mathbf{b}_2)} \{k_1^2 k_2^2 (\mathbf{q}_1 \cdot \mathbf{q}_2)^2 \\
&- k_1^2 (\mathbf{q}_1 \cdot \mathbf{q}_2) [(\mathbf{k}_2 \cdot \mathbf{q}_1) q_2^2 + (\mathbf{k}_2 \cdot \mathbf{q}_2) q_1^2 - q_1^2 q_2^2] \\
&- k_2^2 (\mathbf{q}_1 \cdot \mathbf{q}_2) [(\mathbf{k}_1 \cdot \mathbf{q}_1) q_2^2 + (\mathbf{k}_1 \cdot \mathbf{q}_2) q_1^2 - q_1^2 q_2^2] \\
&+ q_1^2 q_2^2 [(\mathbf{k}_1 \cdot \mathbf{q}_1)(\mathbf{k}_2 \cdot \mathbf{q}_2) + (\mathbf{k}_1 \cdot \mathbf{q}_2)(\mathbf{k}_2 \cdot \mathbf{q}_1)]\} \tag{5.30}
\end{aligned}$$

with $q_i = |\mathbf{q}_i|$, $k_i = |\mathbf{k}_i|$.

Inserting 5.24 and 5.29 into 4.19 we arrive at the k_T -factorized form for the two gluon production cross section in heavy-light ion collisions

$$\begin{aligned}
\frac{d\sigma}{d^2k_1 dy_1 d^2k_2 dy_2} &= \left(\frac{2\alpha_s}{C_F}\right)^2 \frac{1}{k_1^2 k_2^2} \int d^2B d^2b_1 d^2b_2 \int d^2q_1 d^2q_2 \\
&\times \left\langle \frac{d\phi_{A_1}(\mathbf{q}_1, y=0)}{d^2(\mathbf{B} - \mathbf{b}_1)} \right\rangle_{A_1} \left\langle \frac{d\phi_{A_1}(\mathbf{q}_2, y=0)}{d^2(\mathbf{B} - \mathbf{b}_2)} \right\rangle_{A_1} \left\{ \left\langle \frac{d\phi_{A_2}^D(\mathbf{q}_1 - \mathbf{k}_1, \mathbf{q}_2 - \mathbf{k}_2, y)}{d^2b_1 d^2b_2} \right\rangle_{A_2} \right. \\
&\left. + \left[\frac{\mathcal{K}(\mathbf{b}_1, \mathbf{b}_2, \mathbf{k}_1, \mathbf{k}_2, \mathbf{q}_1, \mathbf{q}_2)}{N_c^2 - 1} \left\langle \frac{d\phi_{A_2}^Q(\mathbf{q}_1 - \mathbf{k}_1, \mathbf{q}_2 - \mathbf{k}_2, y)}{d^2b_1 d^2b_2} \right\rangle_{A_2} + (\mathbf{k}_2 \rightarrow -\mathbf{k}_2) \right] \right\} \tag{5.31}
\end{aligned}$$

with $y \approx y_1 \approx y_2$ in the curly brackets. 5.31 is the main result of this section.

Notice that 5.31 has all of the properties we expected: it contains the convolution over the impact parameters \mathbf{B} , \mathbf{b}_1 , and \mathbf{b}_2 along with different two-gluon distribution functions. As advertised, 5.31 also contains a ‘‘coefficient function’’ associated with the factorized form of ‘crossed’ diagrams.

The convolution over impact parameters in 5.31 appears to imply that the 2-gluon production cross section is sensitive to the b -dependence of the one- and two-gluon distributions ϕ , ϕ^D , ϕ^Q . From Eqs. 5.6, 5.7, and 5.9 we see that the b -dependence of those gluon distributions is related to that of the dipole, double-trace and quadrupole operators. It is known that any perturbative approach, such as the CGC formalism employed here, cannot describe correctly the b -dependence of scattering amplitudes in peripheral collisions due to the importance of non-perturbative effects [115]. It, therefore, appears that the two-gluon production cross-section is also sensitive to the non-perturbative large- b physics. Note, however, that this conclusion also applies to the single-gluon production in 3.51, since the impact parameter integral in 3.49 is also sensitive to large- b physics. Recent studies [116] appear to indicate that this sensitivity to non-perturbative effects at the periphery is not very strong, and may be negligible at high energies.

Unfortunately the factorization expression 5.31 is different from that used in [61–63]. The expression in those references was motivated by extrapolation of the dilute–dilute scattering case to the dense–dense scattering by analogy with the single-gluon production 3.51. While our result is valid only for the dense-dilute scattering, we can conclude that the extrapolation suggested in [48, 49, 61–63] does not work in the dense-dilute case, and is, therefore, unlikely to be valid in the dense-dense scattering case either.

Just like 5.24, the expression 5.31 is not projectile-target symmetric. While this is natural due to the asymmetric treatment of the target and projectile in our dense-dilute scattering approximation, this asymmetry also means that a simple generalization to the case of nucleus–nucleus scattering along the lines of what was done with 3.51 in [57, 117–119] appears to be impossible for 5.31.

The factorized form of the two-gluon production cross section 5.31 contains a few interesting properties. If we look at the large- N_c limit the ‘crossed’ diagrams contribution can be neglected and, using 5.12, the two-gluon singlet distribution function factorizes into two single gluon distribution functions,

$$\begin{aligned} \frac{d\sigma}{d^2k_1 dy_1 d^2k_2 dy_2} \Big|_{\text{large-}N_c} &= \left(\frac{2\alpha_s}{C_F} \right)^2 \frac{1}{k_1^2 k_2^2} \int d^2B d^2b_1 d^2b_2 \int d^2q_1 d^2q_2 \\ &\times \left\langle \frac{d\phi_{A_1}(\mathbf{q}_1, y=0)}{d^2(\mathbf{B}-\mathbf{b}_1)} \right\rangle_{A_1} \left\langle \frac{d\phi_{A_1}(\mathbf{q}_2, y=0)}{d^2(\mathbf{B}-\mathbf{b}_2)} \right\rangle_{A_1} \\ &\times \left\langle \frac{d\phi_{A_2}(\mathbf{q}_1-\mathbf{k}_1, y)}{d^2b_1} \right\rangle_{A_2} \left\langle \frac{d\phi_{A_2}(\mathbf{q}_2-\mathbf{k}_2, y)}{d^2b_2} \right\rangle_{A_2}. \end{aligned} \quad (5.32)$$

This equation can only generate correlations between the two gluons through the convolution over the impact parameters, which are geometric correlations [6] (Sec. 2.3.2). This form does not contain the information needed to, say, calculate the correlation function 4.43, since for that one needs terms that are subleading in the large- N_c limit.

Another interesting property is that we can isolate the part of the cross-section that gives rise to HBT correlations [97]. Due to the nature of HBT correlations, the only way the correlations can be generated is through interference effects. Thus only the ‘crossed’ diagrams contribute. In addition, for the correlation to be pure HBT, the two produced gluons should have the same colors (to be identical particles): imposing same-color requirement on the ‘crossed’ diagrams is equivalent to the projection

employed in arriving at 5.20. We conclude that the only part of the quadrupole two-gluon distribution function 5.9 that contributes to HBT correlations is the portion that can be factorized into two single-gluon distributions shown in 5.20. With the help of 5.20 the HBT part of the two-gluon production cross-section can be written as

$$\begin{aligned}
\frac{d\sigma_{HBT}}{d^2k_1 dy_1 d^2k_2 dy_2} &= \left(\frac{2\alpha_s}{C_F}\right)^2 \frac{1}{k_1^2 k_2^2} \int d^2B d^2b_1 d^2b_2 \int d^2q_1 d^2q_2 \\
&\times \frac{\mathcal{K}(\mathbf{b}_1, \mathbf{b}_2, \mathbf{k}_1, \mathbf{k}_2, \mathbf{q}_1, \mathbf{q}_2)}{N_c^2 - 1} \left\langle \frac{d\phi_{A_1}(\mathbf{q}_1, y=0)}{d^2(\mathbf{B} - \mathbf{b}_1)} \right\rangle_{A_1} \left\langle \frac{d\phi_{A_1}(\mathbf{q}_2, y=0)}{d^2(\mathbf{B} - \mathbf{b}_2)} \right\rangle_{A_1} \\
&\times \left\langle \frac{d\phi_{A_2}(\mathbf{q}_1 - \mathbf{k}_1, y)}{d^2b_1} \right\rangle_{A_2} \left\langle \frac{d\phi_{A_2}(\mathbf{q}_2 - \mathbf{k}_2, y)}{d^2b_2} \right\rangle_{A_2} + (\mathbf{k}_2 \rightarrow -\mathbf{k}_2). \quad (5.33)
\end{aligned}$$

To summarize this section let us stress that we were able to find a factorized form for the two-gluon production cross section in heavy-light ion collisions, given by 5.31. It had to be written in a different form than that of the single gluon production cross-section 3.51. In particular, in 5.31 we have a convolution over the impact parameters which requires that the distribution functions have to be written as differentials with respect to impact parameters, that is as gluon Wigner distributions. There was also a ‘‘coefficient function’’ factor 5.30 that was associated with the interference effects included in the ‘crossed’ diagrams. These facts may have important implications for k_T -factorization when it comes to multi-gluon cross-sections and could possibly give insight into the nature of k_T -factorization in general.

5.3 Summary

In this chapter we looked at two different topics. The first topic was the effect different collisional geometries had on the two-gluon correlations of interest. We

found that in U+U collisions there is an enhancement of the correlations for tip-on-tip collisions as opposed to side-on-side. This effect is opposite of what one would see for correlations due to elliptic flow, which gives a possible way to distinguish the two mechanisms for generating two-particle correlations. Secondly we found the k_T -factorized form for the two-gluon production cross section. This is drastically different from the form associated with single-gluon production and shows that one has to be careful when using k_T -factorization to calculate multi-gluon production. We were also able to isolate the “HBT” correlations and showed that these correlations exist to all orders in saturation corrections of the target. This implies that the “HBT” correlations give information about the geometry of the collision immediately after the multiple rescatterings.

Chapter 6: Conclusions

Starting out with a general introduction into the physics involved we briefly covered QCD, heavy-ion collisions and saturation physics in Ch. 1. This laid the ground work for looking at the problem of interest, two-particle correlations in heavy-light ion collisions. A quantitative overview of QCD (needed for the calculation), an explanation of the heavy-light ion regime and its implication on the two-particle correlations was given in Ch. 2.

Ch. 3 consisted of a review of the known result for single-gluon production in pA collisions within the saturation framework in the Classical MV limit. This served as a pedagogical way of seeing how exactly the saturation framework is used in practical situations. Not only that but we were able to extend calculations here to a more complicated situation, the two-gluon correlations in heavy-light ion collisions of interest. The topics reviewed included how the target nucleus produces a shock wave (Sec. 3.1), how exactly the resulting shock wave can be analyzed (Sec. 3.3), the pA single-gluon production cross section (Sec. 3.2) and its k_T -factorized form (Sec. 3.4).

With Ch. 4 we covered the result of the work presented in [6]. This included the calculation of the two-gluon production cross section in the heavy-light ion regime. There were three distinct contributions which contributed to the cross section, one being the “square” terms (diagrams), Sec. 4.1.2. The other two contribution were

combined and formed a single contribution we call the “crossed” terms (diagrams), Sec. 4.1.3. In Sec. 4.2, we saw three distinct types of long-range in rapidity correlations: a correlation which is peaked in azimuthal angle on the near-side ($\Delta\phi = 0$), an equal-and-opposite correlation on the away-side ($\Delta\phi = \pi$), and a correlation that seems similar to a HBT correlation which are peaked when the transverse momenta of the particles are the same and when they are equal and opposite ($\mathbf{k}_1 = \mathbf{k}_2$ and $\mathbf{k}_1 = -\mathbf{k}_2$). All of the two-gluon correlations produced in this heavy-light ion regime end up being symmetric in azimuthal angle ($\Delta\phi$). It should be noted that the theoretical results presented here were posted on arXiv before the away-side ridge was discovered at ALICE in p-Pb collisions [4].

In Ch. 5 we covered some of the work presented in [7], two more implications of the two-gluon production cross section and the correlation function derived in Ch. 4. It was shown, Sec. 5.1 that in the collisions of asymmetric ions (examples being Uranium and Gold) the effects of saturation give rise to correlations that behave differently than those due to hydrodynamical flow. We focused on U+U collisions and showed that there is an enhancement of the two-particle correlations in tip-on-tip collisions when compared with side-on-side collisions, which is opposite of that predicted by hydrodynamics. This gives a way to distinguish correlations due to saturation effects and correlations due to hydrodynamics. In Sec. 5.2 we derived the k_T -factorized form of the two-gluon production cross section in the heavy-light ion limit. We found that, unlike the pA case the cross section cannot be written in terms of the usual unintegrated gluon distributions. Instead we had to introduce our own gluon distribution which end up being Wigner distributions, functions of

both transverse momentum and transverse position. This gives insight into how k_T -factorization works in general.

There are still a few outstanding issues with two-gluon correlations in heavy-light ion collisions that need to be address. One such issue is rapidity dependence of the correlations. This was partially addressed in [7], where we found that to lowest order in saturation effects the correlations are independent of the center-of-mass energy of the collision. However, this did not include rapidity evolution between the two gluons, which needs to be addressed to understand the full correlation function.

We would like to know the full heavy ion collision case. In order to approach this issue a basic starting point would be finding the single-gluon production cross section in heavy ion collisions. Work in this direction has been done in [120], where we calculate part of the single-gluon production cross section for the heavy-light ion case, taking into account two nucleons in the projectile and all saturation corrections in the target (beyond the leading order result presented in Ch. 3). This is not a complete calculation though and the continuation of this project is a work in progress.

The correlations presented in this work were leading-order in saturation scale in the heavy-light ion regime: however they were sub-leading in N_c . It could be possible that this suppression makes it so that the sub-leading in projectile saturation corrections two-gluon production process, where we have a single nucleon in the projectile emitting two gluons, could be comparable in magnitude in the actual experiment. The cross section for this process needs to be calculated in order to see what types of additional correlations arise, which is left for future work.

Bibliography

- [1] K. A. Olive et al. Review of Particle Physics. *Chin. Phys.*, C38:090001, 2014.
- [2] Steffen A. Bass. Cartoon of a ultra-relativistic heavy-ion collision.
- [3] H. Abramowicz et al. Combination of measurements of inclusive deep inelastic $e^\pm p$ scattering cross sections and QCD analysis of HERA data. *Eur. Phys. J.*, C75(12):580, 2015.
- [4] Betty Abelev et al. Long-range angular correlations on the near and away side in $p - Pb$ collisions at $\sqrt{s_{NN}} = 5.02$ TeV. 2012.
- [5] K. Yagi, T. Hatsuda, and Y. Miake. Quark-gluon plasma: From big bang to little bang. *Camb. Monogr. Part. Phys. Nucl. Phys. Cosmol.*, 23:1–446, 2005.
- [6] Yuri V. Kovchegov and Douglas E. Wertepny. Long-Range Rapidity Correlations in Heavy-Light Ion Collisions. *Nucl.Phys.*, A906:50–83, 2013.
- [7] Yuri V. Kovchegov and Douglas E. Wertepny. Two-Gluon Correlations in Heavy-Light Ion Collisions: Energy and Geometry Dependence, IR Divergences, and k_T -Factorization. *Nucl.Phys.*, A925:254–295, 2014.
- [8] Chen-Ning Yang and R. L. Mills. Isotopic spin conservation and a generalized gauge invariance. 1954.
- [9] Murray Gell-Mann. A Schematic Model of Baryons and Mesons. *Phys. Lett.*, 8:214–215, 1964.
- [10] H. Fritzsch, Murray Gell-Mann, and H. Leutwyler. Advantages of the Color Octet Gluon Picture. *Phys. Lett.*, B47:365–368, 1973.
- [11] D. J. Gross and Frank Wilczek. Ultraviolet Behavior of Non-Abelian Gauge Theories. *Phys. Rev. Lett.*, 30:1343–1346, 1973.
- [12] H. David Politzer. Reliable Perturbative Results for Strong Interactions? *Phys. Rev. Lett.*, 30:1346–1349, 1973.

- [13] Steven Weinberg. Nonabelian Gauge Theories of the Strong Interactions. *Phys. Rev. Lett.*, 31:494–497, 1973.
- [14] John David Jackson. *Classical electrodynamics*. Wiley, New York, NY, 3rd ed. edition, 1999.
- [15] Steven Weinberg. *The quantum theory of fields. Vol. 2: Modern applications*. Cambridge University Press, 2013.
- [16] N. Brambilla et al. QCD and Strongly Coupled Gauge Theories: Challenges and Perspectives. *Eur. Phys. J.*, C74(10):2981, 2014.
- [17] Charles Gale, Sangyong Jeon, and Bjoern Schenke. Hydrodynamic Modeling of Heavy-Ion Collisions. *Int. J. Mod. Phys.*, A28:1340011, 2013.
- [18] A. Accardi, J.L. Albacete, M. Anselmino, N. Armesto, E.C. Aschenauer, et al. Electron Ion Collider: The Next QCD Frontier - Understanding the glue that binds us all. 2012.
- [19] Jamal Jalilian-Marian and Yuri V. Kovchegov. Saturation physics and deuteron gold collisions at RHIC. *Prog. Part. Nucl. Phys.*, 56:104–231, 2006.
- [20] Heribert Weigert. Evolution at small x_{bj} : The Color Glass Condensate. *Prog. Part. Nucl. Phys.*, 55:461–565, 2005.
- [21] Edmond Iancu and Raju Venugopalan. The color glass condensate and high energy scattering in QCD. 2003.
- [22] Francois Gelis, Edmond Iancu, Jamal Jalilian-Marian, and Raju Venugopalan. The Color Glass Condensate. *Ann.Rev.Nucl.Part.Sci.*, 60:463–489, 2010.
- [23] Yuri V. Kovchegov and E. Levin. *Quantum Chromodynamics at High Energy*. Cambridge University Press, 2012.
- [24] E. A. Kuraev, L. N. Lipatov, and Victor S. Fadin. The Pomeranchuk singularity in non-Abelian gauge theories. *Sov. Phys. JETP*, 45:199–204, 1977.
- [25] I.I. Balitsky and L.N. Lipatov. The Pomeranchuk Singularity in Quantum Chromodynamics. *Sov.J.Nucl.Phys.*, 28:822–829, 1978.
- [26] I. Balitsky. Operator expansion for high-energy scattering. *Nucl. Phys.*, B463:99–160, 1996.
- [27] Ian Balitsky. Factorization and high-energy effective action. *Phys. Rev.*, D60:014020, 1999.

- [28] Yuri V. Kovchegov. Small- x F_2 structure function of a nucleus including multiple pomeron exchanges. *Phys. Rev.*, D60:034008, 1999.
- [29] Yuri V. Kovchegov. Unitarization of the BFKL pomeron on a nucleus. *Phys. Rev.*, D61:074018, 2000.
- [30] Jamal Jalilian-Marian, Alex Kovner, and Heribert Weigert. The Wilson renormalization group for low x physics: Gluon evolution at finite parton density. *Phys. Rev.*, D59:014015, 1998.
- [31] Jamal Jalilian-Marian, Alex Kovner, Andrei Leonidov, and Heribert Weigert. The Wilson renormalization group for low x physics: Towards the high density regime. *Phys. Rev.*, D59:014014, 1998.
- [32] Edmond Iancu, Andrei Leonidov, and Larry D. McLerran. The renormalization group equation for the color glass condensate. *Phys. Lett.*, B510:133–144, 2001.
- [33] Edmond Iancu, Andrei Leonidov, and Larry D. McLerran. Nonlinear gluon evolution in the color glass condensate. I. *Nucl. Phys.*, A692:583–645, 2001.
- [34] Larry D. McLerran and Raju Venugopalan. Green’s functions in the color field of a large nucleus. *Phys. Rev.*, D50:2225–2233, 1994.
- [35] Larry D. McLerran and Raju Venugopalan. Gluon distribution functions for very large nuclei at small transverse momentum. *Phys. Rev.*, D49:3352–3355, 1994.
- [36] Larry D. McLerran and Raju Venugopalan. Computing quark and gluon distribution functions for very large nuclei. *Phys. Rev.*, D49:2233–2241, 1994.
- [37] J. Adams et al. Distributions of charged hadrons associated with high transverse momentum particles in $p + p$ and $Au + Au$ collisions at $s_{NN}^{1/2} = 200$ GeV. *Phys. Rev. Lett.*, 95:152301, 2005.
- [38] A. Adare et al. Dihadron azimuthal correlations in Au+Au collisions at $\sqrt{s_{NN}}=200$ GeV. *Phys. Rev.*, C78:014901, 2008.
- [39] B. Alver et al. High transverse momentum triggered correlations over a large pseudorapidity acceptance in Au+Au collisions at $\sqrt{s_{NN}}=200$ GeV. *Phys. Rev. Lett.*, 104:062301, 2010.
- [40] B.I. Abelev et al. Long range rapidity correlations and jet production in high energy nuclear collisions. *Phys.Rev.*, C80:064912, 2009.
- [41] Vardan Khachatryan et al. Observation of Long-Range Near-Side Angular Correlations in Proton-Proton Collisions at the LHC. *JHEP*, 09:091, 2010.

- [42] Serguei Chatrchyan et al. Observation of long-range near-side angular correlations in proton-lead collisions at the LHC. 2012.
- [43] Adrian Dumitru, Francois Gelis, Larry McLerran, and Raju Venugopalan. Glasma flux tubes and the near side ridge phenomenon at RHIC. *Nucl. Phys.*, A810:91–108, 2008.
- [44] Sean Gavin, Larry McLerran, and George Moschelli. Long Range Correlations and the Soft Ridge in Relativistic Nuclear Collisions. *Phys. Rev.*, C79:051902, 2009.
- [45] Nestor Armesto, Larry McLerran, and Carlos Pajares. Long Range Forward-Backward Correlations and the Color Glass Condensate. *Nucl.Phys.*, A781:201–208, 2007.
- [46] N. Armesto, M.A. Braun, and C. Pajares. On the long-range correlations in hadron-nucleus collisions. *Phys.Rev.*, C75:054902, 2007.
- [47] Kevin Dusling, Francois Gelis, Tuomas Lappi, and Raju Venugopalan. Long range two-particle rapidity correlations in A+A collisions from high energy QCD evolution. *Nucl. Phys.*, A836:159–182, 2010.
- [48] Adrian Dumitru, Kevin Dusling, Francois Gelis, Jamal Jalilian-Marian, Tuomas Lappi, et al. The Ridge in proton-proton collisions at the LHC. *Phys.Lett.*, B697:21–25, 2011.
- [49] Adrian Dumitru and Jamal Jalilian-Marian. Two-particle correlations in high energy collisions and the gluon four-point function. *Phys. Rev.*, D81:094015, 2010.
- [50] Alex Kovner and Michael Lublinsky. Angular Correlations in Gluon Production at High Energy. *Phys.Rev.*, D83:034017, 2011.
- [51] Francois Gelis, Tuomas Lappi, and Raju Venugopalan. High energy factorization in nucleus-nucleus collisions. 3. Long range rapidity correlations. *Phys.Rev.*, D79:094017, 2009.
- [52] Alex Kovner, Larry D. McLerran, and Heribert Weigert. Gluon production from nonAbelian Weizsacker-Williams fields in nucleus-nucleus collisions. *Phys. Rev.*, D52:6231–6237, 1995.
- [53] Yuri V. Kovchegov and Dirk H. Rischke. Classical gluon radiation in ultrarelativistic nucleus nucleus collisions. *Phys. Rev.*, C56:1084–1094, 1997.

- [54] Alex Krasnitz, Yasushi Nara, and Raju Venugopalan. Classical gluodynamics of high energy nuclear collisions: An erratum and an update. *Nucl. Phys.*, A727:427–436, 2003.
- [55] J. P. Blaizot, T. Lappi, and Y. Mehtar-Tani. On the gluon spectrum in the glasma. *Nucl. Phys.*, A846:63–82, 2010.
- [56] Yuri V. Kovchegov, Eugene Levin, and Larry D. McLerran. Large scale rapidity correlations in heavy ion collisions. *Phys.Rev.*, C63:024903, 2001.
- [57] Javier L. Albacete and Adrian Dumitru. A model for gluon production in heavy-ion collisions at the LHC with rcBK unintegrated gluon densities. 2010.
- [58] Alex Kovner and Michael Lublinsky. On Angular Correlations and High Energy Evolution. *Phys.Rev.*, D84:094011, 2011.
- [59] Eugene Levin and Amir H. Rezaeian. The Ridge from the BFKL evolution and beyond. *Phys.Rev.*, D84:034031, 2011.
- [60] Alex Kovner and Michael Lublinsky. Angular and long range rapidity correlations in particle production at high energy. *Int.J.Mod.Phys.*, E22:1330001, 2013.
- [61] Kevin Dusling and Raju Venugopalan. Azimuthal collimation of long range rapidity correlations by strong color fields in high multiplicity hadron-hadron collisions. *Phys.Rev.Lett.*, 108:262001, 2012.
- [62] Kevin Dusling and Raju Venugopalan. Explanation of systematics of CMS p+Pb high multiplicity di-hadron data at $\sqrt{s_{\text{NN}}} = 5.02$ TeV. 2012.
- [63] Kevin Dusling and Raju Venugopalan. Evidence for BFKL and saturation dynamics from di-hadron spectra at the LHC. 2012.
- [64] E. Gardi, J. Kuokkanen, K. Rummukainen, and H. Weigert. Running coupling and power corrections in nonlinear evolution at the high-energy limit. *Nucl. Phys.*, A784:282–340, 2007.
- [65] Y. Kovchegov and H. Weigert. Triumvirate of Running Couplings in Small- x Evolution. *Nucl. Phys. A*, 784:188–226, 2007.
- [66] I. I. Balitsky. Quark Contribution to the Small- x Evolution of Color Dipole. *Phys. Rev. D*, 75:014001, 2007.
- [67] Alex Krasnitz and Raju Venugopalan. The initial energy density of gluons produced in very high energy nuclear collisions. *Phys. Rev. Lett.*, 84:4309–4312, 2000.

- [68] T. Lappi. Production of gluons in the classical field model for heavy ion collisions. *Phys. Rev.*, C67:054903, 2003.
- [69] L. D. Faddeev and V. N. Popov. Feynman Diagrams for the Yang-Mills Field. *Phys. Lett.*, B25:29–30, 1967.
- [70] Giovanni A. Chirilli, Yuri V. Kovchegov, and Douglas E. Wertheim. Regularization of the Light-Cone Gauge Gluon Propagator Singularities Using Sub-Gauge Conditions. *JHEP*, 12:138, 2015.
- [71] G. Sterman. *An Introduction to quantum field theory*. Cambridge University Press, Cambridge, UK, 1993.
- [72] Michael E. Peskin and D. V. Schroeder. *An Introduction to quantum field theory*. Addison-Wesley, Reading, USA, 1995.
- [73] Yuri V. Kovchegov. Non-abelian Weizsäcker-Williams field and a two-dimensional effective color charge density for a very large nucleus. *Phys. Rev.*, D54:5463–5469, 1996.
- [74] Alfred H. Mueller. Small x Behavior and Parton Saturation: A QCD Model. *Nucl. Phys.*, B335:115, 1990.
- [75] Yuri V. Kovchegov. Quantum structure of the non-Abelian Weizsäcker-Williams field for a very large nucleus. *Phys. Rev.*, D55:5445–5455, 1997.
- [76] K. Eggert, H. Frenzel, W. Thome, B. Betev, P. Darriulat, et al. Angular Correlations Between the Charged Particles Produced in pp Collisions at ISR Energies. *Nucl.Phys.*, B86:201, 1975.
- [77] Derek Teaney and Raju Venugopalan. Classical computation of elliptic flow at large transverse momentum. *Phys.Lett.*, B539:53–58, 2002.
- [78] G. Peter Lepage and Stanley J. Brodsky. Exclusive processes in perturbative quantum chromodynamics. *Phys. Rev.*, D22:2157, 1980.
- [79] Yuri V. Kovchegov and Alfred H. Mueller. Gluon production in current nucleus and nucleon nucleus collisions in a quasi-classical approximation. *Nucl. Phys.*, B529:451–479, 1998.
- [80] Yuri V. Kovchegov and Kirill Tuchin. Inclusive gluon production in dis at high parton density. *Phys. Rev.*, D65:074026, 2002.
- [81] Jean Paul Blaizot, Francois Gelis, and Raju Venugopalan. High energy p A collisions in the color glass condensate approach. I: Gluon production and the Cronin effect. *Nucl. Phys.*, A743:13–56, 2004.

- [82] M. A. Braun. Inclusive jet production on the nucleus in the perturbative QCD with $N_c \rightarrow \infty$. *Phys. Lett.*, B483:105–114, 2000.
- [83] Dmitri Kharzeev, Yuri V. Kovchegov, and Kirill Tuchin. Cronin effect and high-p(t) suppression in p a collisions. *Phys. Rev.*, D68:094013, 2003.
- [84] Jamal Jalilian-Marian and Yuri V. Kovchegov. Inclusive two-gluon and valence quark-gluon production in DIS and p A. *Phys. Rev.*, D70:114017, 2004.
- [85] Zhang Chen and Alfred H. Mueller. The dipole picture of high-energy scattering, the BFKL equation and many gluon compound states. *Nucl. Phys.*, B451:579–604, 1995.
- [86] Fabio Dominguez, A.H. Mueller, Stephane Munier, and Bo-Wen Xiao. On the small-x evolution of the color quadrupole and the Weizsäcker-Williams gluon distribution. *Phys.Lett.*, B705:106–111, 2011.
- [87] Adrian Dumitru, Jamal Jalilian-Marian, Tuomas Lappi, Bjoern Schenke, and Raju Venugopalan. Renormalization group evolution of multi-gluon correlators in high energy QCD. *Phys.Lett.*, B706:219–224, 2011.
- [88] E. Iancu and D.N. Triantafyllopoulos. Higher-point correlations from the JIMWLK evolution. *JHEP*, 1111:105, 2011.
- [89] Daniel Grumiller and Paul Romatschke. On the collision of two shock waves in AdS(5). *JHEP*, 0808:027, 2008.
- [90] Javier L. Albacete, Yuri V. Kovchegov, and Anastasios Taliotis. Modeling Heavy Ion Collisions in AdS/CFT. *JHEP*, 0807:100, 2008.
- [91] Javier L. Albacete, Yuri V. Kovchegov, and Anastasios Taliotis. Asymmetric Collision of Two Shock Waves in AdS₅. *JHEP*, 0905:060, 2009.
- [92] Paul M. Chesler and Laurence G. Yaffe. Holography and colliding gravitational shock waves in asymptotically AdS₅ spacetime. *Phys.Rev.Lett.*, 106:021601, 2011.
- [93] Victor S. Fadin, E.A. Kuraev, and L.N. Lipatov. On the Pomeranchuk Singularity in Asymptotically Free Theories. *Phys.Lett.*, B60:50–52, 1975.
- [94] T. Lappi, S. Srednyak, and R. Venugopalan. Non-perturbative computation of double inclusive gluon production in the Glasma. *JHEP*, 1001:066, 2010.
- [95] Nicolas Borghini, Phuong Mai Dinh, and Jean-Yves Ollitrault. A New method for measuring azimuthal distributions in nucleus-nucleus collisions. *Phys.Rev.*, C63:054906, 2001.

- [96] Nicolas Borghini, Phuong Mai Dinh, and Jean-Yves Ollitrault. Flow analysis from multiparticle azimuthal correlations. *Phys.Rev.*, C64:054901, 2001.
- [97] R. Hanbury Brown and R.Q. Twiss. A Test of a new type of stellar interferometer on Sirius. *Nature*, 178:1046–1048, 1956.
- [98] Ulrich W. Heinz and Barbara V. Jacak. Two particle correlations in relativistic heavy ion collisions. *Ann.Rev.Nucl.Part.Sci.*, 49:529–579, 1999.
- [99] J. Adams et al. Azimuthally sensitive HBT in Au + Au collisions at $\sqrt{s(NN)} = 200$ -GeV. *Phys.Rev.Lett.*, 93:012301, 2004.
- [100] G.I. Kopylov and M.I. Podgoretsky. Correlations of identical particles emitted by highly excited nuclei. *Sov.J.Nucl.Phys.*, 15:219–223, 1972.
- [101] A. Capella, A. Krzywicki, and E.M. Levin. Pion interferometry and intermittency in heavy ion collisions. *Phys.Rev.*, D44:704–716, 1991.
- [102] M. Asakawa, T. Csorgo, and M. Gyulassy. Squeezed correlations and spectra for mass shifted bosons. *Phys.Rev.Lett.*, 83:4013–4016, 1999.
- [103] Tamas Csorgo and Sandra S. Padula. Disappearance of Squeezed Back-to-Back Correlations: A New signal of hadron freeze-out from a supercooled Quark Gluon Plasma. *Braz.J.Phys.*, 37:949–962, 2007.
- [104] L. Frankfurt, M. Strikman, and C. Weiss. Dijet production as a centrality trigger for pp collisions at CERN LHC. *Phys.Rev.*, D69:114010, 2004.
- [105] L. Frankfurt, M. Strikman, and C. Weiss. Transverse nucleon structure and diagnostics of hard parton-parton processes at LHC. *Phys.Rev.*, D83:054012, 2011.
- [106] B. Alver and G. Roland. Collision geometry fluctuations and triangular flow in heavy-ion collisions. *Phys.Rev.*, C81:054905, 2010.
- [107] Ulrich W. Heinz and Anthony Kuhlman. Anisotropic flow and jet quenching in ultrarelativistic U + U collisions. *Phys.Rev.Lett.*, 94:132301, 2005.
- [108] Anthony J. Kuhlman and Ulrich W. Heinz. Multiplicity distribution and source deformation in full-overlap U+U collisions. *Phys.Rev.*, C72:037901, 2005.
- [109] Anthony Kuhlman, Ulrich W. Heinz, and Yuri V. Kovchegov. Gluon saturation effects in relativistic U + U collisions. *Phys. Lett.*, B638:171–177, 2006.
- [110] Eugene P. Wigner. On the quantum correction for thermodynamic equilibrium. *Phys.Rev.*, 40:749–760, 1932.

- [111] Andrei V. Belitsky, X. Ji, and F. Yuan. Final state interactions and gauge invariant parton distributions. *Nucl.Phys.*, B656:165–198, 2003.
- [112] Jamal Jalilian-Marian, Alex Kovner, Larry D. McLerran, and Heribert Weigert. The intrinsic glue distribution at very small x . *Phys. Rev.*, D55:5414–5428, 1997.
- [113] Fabio Dominguez, Cyrille Marquet, Bo-Wen Xiao, and Feng Yuan. Universality of Unintegrated Gluon Distributions at small x . *Phys.Rev.*, D83:105005, 2011.
- [114] Predrag Cvitanovic. *Group theory: Birdtracks, Lie’s and exceptional groups*. Princeton University Press, 2008. Available online at <http://birdtracks.eu/>.
- [115] Alexander Kovner and Urs Achim Wiedemann. Nonlinear qcd evolution: Saturation without unitarization. *Phys. Rev.*, D66:051502, 2002.
- [116] Eugene Levin, Lev Lipatov, and Marat Siddikov. BFKL Pomeron with massive gluons. 2014.
- [117] Dmitri Kharzeev and Eugene Levin. Manifestations of high density QCD in the first RHIC data. *Phys. Lett.*, B523:79–87, 2001.
- [118] Dmitri Kharzeev, Eugene Levin, and Marzia Nardi. The onset of classical QCD dynamics in relativistic heavy ion collisions. *Phys. Rev.*, C71:054903, 2005.
- [119] Javier L. Albacete. Particle multiplicities in Lead-Lead collisions at the LHC from non-linear evolution with running coupling. *Phys. Rev. Lett.*, 99:262301, 2007.
- [120] Giovanni A. Chirilli, Yuri V. Kovchegov, and Douglas E. Wertheim. Classical Gluon Production Amplitude for Nucleus-Nucleus Collisions: First Saturation Correction in the Projectile. *JHEP*, 03:015, 2015.
- [121] Yuri V. Kovchegov. Diffractive gluon production in proton nucleus collisions and in DIS. *Phys. Rev.*, D64:114016, 2001.
- [122] Cyrille Marquet and Heribert Weigert. New observables to test the Color Glass Condensate beyond the large- N_c limit. *Nucl. Phys.*, A843:68–97, 2010.
- [123] N.N. Nikolaev, W. Schafer, and B.G. Zakharov. Nonlinear $k(\text{perpendicular})$ -factorization for gluon-gluon dijets produced off nuclear targets. *Phys.Rev.*, D72:114018, 2005.

Appendix A: Double-trace operator

Our goal here is to calculate the following object

$$\frac{1}{(N_c^2 - 1)^2} \langle \text{Tr}[U_{\mathbf{x}_1} U_{\mathbf{x}_2}^\dagger] \text{Tr}[U_{\mathbf{x}_3} U_{\mathbf{x}_4}^\dagger] \rangle \quad (\text{A.1})$$

in the quasi-classical MV/GM approximation at the lowest non-trivial order in $1/N_c^2$ expansion in the 't Hooft's large- N_c limit. We assume that the saturation scale is N_c -independent, that is $Q_{s0}^2 \sim (N_c)^0$, due to an order- N_c^2 number of “valence” partons in each nucleon in the target nucleus.

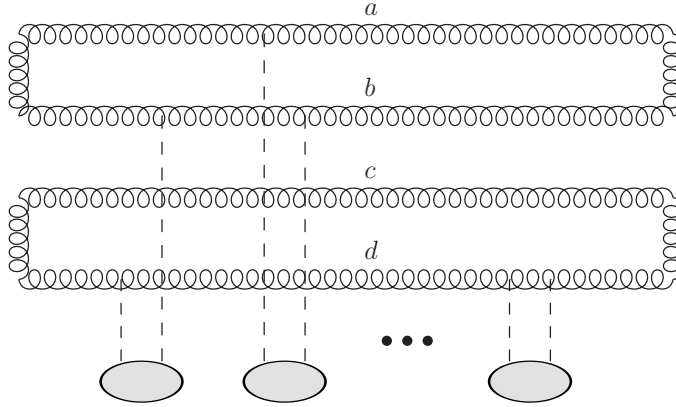


Figure A.1: Diagrams contributing to the correlator in A.1 in the quasi-classical approximation. Vertical dashed lines denote t -channel gluons, while the shaded ovals represent the nucleons in the target nucleus.

A sample of the diagrams contributing to A.1 is shown in A.1, where the t -channel gluons are denoted by dashed lines to simplify the picture. The calculation is straightforward [121]: one simply has to exponentiate the two-gluon exchange interaction with a single nucleon (the nucleons are denoted by shaded ovals in A.1). The only complication is that, unlike the dipole amplitude calculated in [74], the interaction now, for the double-trace operator A.1, is a matrix in the color space. A double trace operator like A.1 with the Wilson lines in the fundamental representation was calculated earlier in [122] (for similar calculations see also [86, 88, 123]).

To exponentiate the matrix we have to choose a basis in the color space of four s -channel gluons in A.1: clearly the net color of the four gluons is always zero. The color states of the four gluons can be classified according to the color states of the top two s -channel gluons, since the color of the bottom pair of s -channel gluons is determined by requiring net color-neutrality of the four s -channel gluon system. The colors of a gluon pair can be decomposed in the following irreducible representations

$$\begin{aligned}
(N_c^2 - 1) \otimes (N_c^2 - 1) &= V_1 \oplus V_2 \oplus V_3 \oplus V_4 \oplus V_5 \oplus V_6 \oplus V_7 \\
&= \mathbf{1} \oplus (N_c^2 - 1) \oplus \frac{N_c^2(N_c - 3)(N_c + 1)}{4} \oplus \frac{N_c^2(N_c + 3)(N_c - 1)}{4} \oplus (N_c^2 - 1) \\
&\oplus \frac{(N_c^2 - 1)(N_c^2 - 4)}{4} \oplus \frac{(N_c^2 - 1)(N_c^2 - 4)}{4}.
\end{aligned} \tag{A.2}$$

Here we are following the notations introduced in [114], see page 120. Labeling the colors of the four s -channel gluons in an arbitrary color state by $a, b, c,$ and d as shown in A.1 we define the color states corresponding to representations $V_1, V_2,$ and V_5 by

$$\begin{aligned}
|P_1\rangle &= \frac{1}{N_c^2 - 1} \delta^{ab} \delta^{cd}, \quad |P_2\rangle = \frac{1}{\sqrt{N_c^2 - 1}} \frac{N_c}{N_c^2 - 4} d^{abe} d^{cde}, \\
|P_5\rangle &= \frac{1}{\sqrt{N_c^2 - 1}} \frac{1}{N_c} f^{abe} f^{cde},
\end{aligned} \tag{A.3}$$

where we differ from P_i 's in [114] by prefactors, since here we demanded that our color states are normalized to one, $\langle P_i | P_j \rangle = \delta^{ij}$. Other color states can be constructed as well [114], but we will only need the states in A.3 for the calculation below.

We denote the interaction with a single nucleon by a two-gluon exchange as $\hat{M}^{a'a,b'b,c'c,d'd}(\mathbf{x}_1, \mathbf{x}_2, \mathbf{x}_3, \mathbf{x}_4)$: it is a matrix in the color space of the s -channel gluons. Often we suppress the color indices and transverse coordinates and notate this as \hat{M} . It is defined by taking averaging over the transverse positions of a single nucleon source with 4 wilson line operators this time

$$\hat{M}^{a'a,b'b,c'c,d'd}(\mathbf{x}_1, \mathbf{x}_2, \mathbf{x}_3, \mathbf{x}_4) = \left\langle U_{\mathbf{x}_1}^{a'a}[z'^+, z^+] U_{\mathbf{x}_2}^{b'b}[z'^+, z^+] U_{\mathbf{x}_3}^{c'c}[z'^+, z^+] U_{\mathbf{x}_4}^{d'd}[z'^+, z^+] \right\rangle_1. \quad (\text{A.4})$$

The corresponding diagram is shown in Fig. A.2.

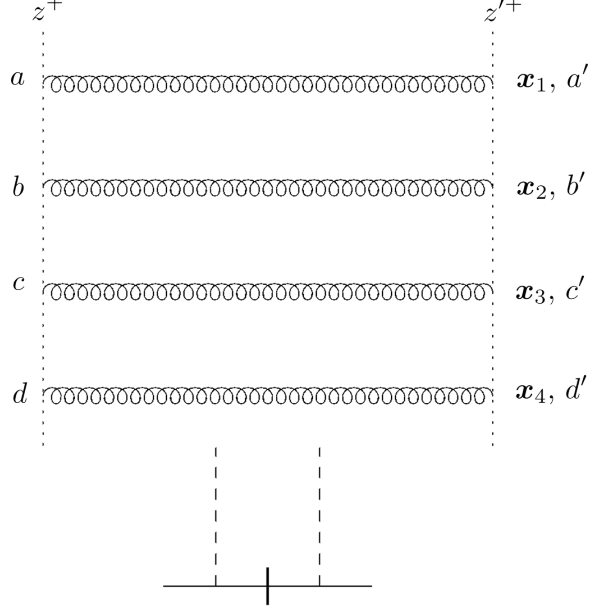


Figure A.2: The diagrammatic representation of the matrix element associated with a nucleon interacting with 4 adjoint Wilson lines, $\hat{M}^{a'a,b'b,c'c,d'd}(\mathbf{x}_1, \mathbf{x}_2, \mathbf{x}_3, \mathbf{x}_4)$. The dotted line represents the gluon fields and it interacts in all possible ways with the Wilson lines.

The procedure to calculate this follows the same lines as the dipole calculation did, the only difference being the number of possible interactions have increased. It should be no surprise that it bares a striking resemblance to 3.35

$$\begin{aligned}
& \hat{M}^{a'a,b'b,c'c,d'd}(\mathbf{x}_1, \mathbf{x}_2, \mathbf{x}_3, \mathbf{x}_4) \\
&= - Q_{s,2}^2 \int \frac{d^2k}{2\pi} \frac{1}{|\mathbf{k}^2|^2} \left[2 \delta^{a'a} \delta^{b'b} \delta^{c'c} \delta^{d'd} + \frac{1}{N_c} [T^e]^{a'a} [T^e]^{b'b} \delta^{c'c} \delta^{d'd} e^{-i\mathbf{k}\cdot(\mathbf{x}_1-\mathbf{x}_2)} \right. \\
&+ \frac{1}{N_c} [T^e]^{a'a} \delta^{b'b} [T^e]^{c'c} \delta^{d'd} e^{-i\mathbf{k}\cdot(\mathbf{x}_1-\mathbf{x}_3)} + \frac{1}{N_c} [T^e]^{a'a} \delta^{b'b} \delta^{c'c} [T^e]^{d'd} e^{-i\mathbf{k}\cdot(\mathbf{x}_1-\mathbf{x}_4)} \\
&+ \frac{1}{N_c} \delta^{a'a} [T^e]^{b'b} [T^e]^{c'c} \delta^{d'd} e^{-i\mathbf{k}\cdot(\mathbf{x}_2-\mathbf{x}_3)} + \frac{1}{N_c} \delta^{a'a} [T^e]^{b'b} \delta^{c'c} [T^e]^{d'd} e^{-i\mathbf{k}\cdot(\mathbf{x}_2-\mathbf{x}_4)} \\
&\left. + \frac{1}{N_c} \delta^{a'a} \delta^{b'b} [T^e]^{c'c} [T^e]^{d'd} e^{-i\mathbf{k}\cdot(\mathbf{x}_3-\mathbf{x}_4)} \right] \quad (\text{A.5})
\end{aligned}$$

Since in the correlator [A.1](#) the top (bottom) two s -channel gluons are in the color-singlet state both before and after the interaction, we write

$$\frac{1}{(N_c^2 - 1)^2} \langle \text{Tr}[U_{\mathbf{x}_1} U_{\mathbf{x}_2}^\dagger] \text{Tr}[U_{\mathbf{x}_3} U_{\mathbf{x}_4}^\dagger] \rangle = \langle P_1 | e^{\hat{M}} | P_1 \rangle. \quad (\text{A.6})$$

Expanding the exponential in a power series and inserting unit operators $\mathbf{1} = \sum_i |P_i\rangle \langle P_i|$ between all the \hat{M} 's yields

$$\frac{1}{(N_c^2 - 1)^2} \langle \text{Tr}[U_{\mathbf{x}_1} U_{\mathbf{x}_2}^\dagger] \text{Tr}[U_{\mathbf{x}_3} U_{\mathbf{x}_4}^\dagger] \rangle = (e^M)_{11} \quad (\text{A.7})$$

where the 7×7 matrix M is defined by its elements,

$$M_{ij} = \langle P_i | \hat{M} | P_j \rangle. \quad (\text{A.8})$$

As an example we calculate M_{11} ,

$$\begin{aligned} M_{11} &= \frac{1}{N_c^2 - 1} \delta^{a'b'} \delta^{c'd'} \hat{M}^{a'a, b'b, c'c, d'd}(\mathbf{x}_1, \mathbf{x}_2, \mathbf{x}_3, \mathbf{x}_4) \frac{1}{N_c^2 - 1} \delta^{ab} \delta^{cd} \\ &= \frac{-1}{(N_c^2 - 1)^2} \delta^{a'b'} \delta^{c'd'} Q_{s,2}^2 \int \frac{d^2 k}{2\pi} \frac{1}{|\mathbf{k}^2|^2} \\ &\quad \times \left[2 \delta^{a'b'} \delta^{c'd'} - \frac{1}{N_c} [T^e T^e]^{a'b'} \delta^{c'd'} e^{-i\mathbf{k} \cdot (\mathbf{x}_1 - \mathbf{x}_2)} + \frac{1}{N_c} [T^e]^{a'b'} [T^e]^{c'd'} e^{-i\mathbf{k} \cdot (\mathbf{x}_1 - \mathbf{x}_3)} \right. \\ &\quad - \frac{1}{N_c} [T^e]^{a'b'} [T^e]^{c'd'} e^{-i\mathbf{k} \cdot (\mathbf{x}_1 - \mathbf{x}_4)} - \frac{1}{N_c} [T^e]^{a'b'} [T^e]^{c'd'} e^{-i\mathbf{k} \cdot (\mathbf{x}_2 - \mathbf{x}_3)} \\ &\quad \left. + \frac{1}{N_c} [T^e]^{a'b'} [T^e]^{c'd'} e^{-i\mathbf{k} \cdot (\mathbf{x}_2 - \mathbf{x}_4)} - \frac{1}{N_c} \delta^{a'b'} [T^e T^e]^{c'd'} e^{-i\mathbf{k} \cdot (\mathbf{x}_3 - \mathbf{x}_4)} \right] \\ &= -Q_{s,2}^2 \int \frac{d^2 k}{2\pi} \frac{1}{|\mathbf{k}^2|^2} [2 - e^{-i\mathbf{k} \cdot (\mathbf{x}_1 - \mathbf{x}_2)} - e^{-i\mathbf{k} \cdot (\mathbf{x}_3 - \mathbf{x}_4)}] \\ &= -\frac{Q_{s,2}^2}{4} \left[|\mathbf{x}_1 - \mathbf{x}_2|^2 \ln \left(\frac{1}{|\mathbf{x}_1 - \mathbf{x}_2| \Lambda} \right) + |\mathbf{x}_3 - \mathbf{x}_4|^2 \ln \left(\frac{1}{|\mathbf{x}_3 - \mathbf{x}_4| \Lambda} \right) \right] \quad (\text{A.9}) \end{aligned}$$

and see that it ends up just being equal to $-D_1$, one of the D_i 's defined in [Eqs. \(4.23\)](#).

All one has to do now is to find the remaining elements of matrix M from [A.8](#), exponentiate it, picking up the “11” matrix element of the exponential. Such a

calculation, while straightforward, is rather involved: here we will utilize the large- N_c limit to construct an approximate result.

Calculating some of the elements of the matrix M and evaluating the N_c -order of the remaining matrix elements yields

$$M = \begin{pmatrix} D_1 & 0 & 0 & 0 & \frac{D_3-D_2}{\sqrt{N_c^2-1}} & 0 & 0 \\ 0 & M_{22} & \mathcal{O}(\frac{1}{N_c}) & \mathcal{O}(\frac{1}{N_c}) & M_{25} & \mathcal{O}(\frac{1}{N_c}) & \mathcal{O}(\frac{1}{N_c}) \\ 0 & \mathcal{O}(\frac{1}{N_c}) & \dots & \dots & \mathcal{O}(\frac{1}{N_c}) & \dots & \dots \\ 0 & \mathcal{O}(\frac{1}{N_c}) & \dots & \dots & \mathcal{O}(\frac{1}{N_c}) & \dots & \dots \\ \frac{D_3-D_2}{\sqrt{N_c^2-1}} & M_{25} & \mathcal{O}(\frac{1}{N_c}) & \mathcal{O}(\frac{1}{N_c}) & M_{22} & \mathcal{O}(\frac{1}{N_c}) & \mathcal{O}(\frac{1}{N_c}) \\ 0 & \mathcal{O}(\frac{1}{N_c}) & \dots & \dots & \mathcal{O}(\frac{1}{N_c}) & \dots & \dots \\ 0 & \mathcal{O}(\frac{1}{N_c}) & \dots & \dots & \mathcal{O}(\frac{1}{N_c}) & \dots & \dots \end{pmatrix} \quad (\text{A.10})$$

$$M_{22} = \frac{1}{2}D_1 + \frac{1}{4}(D_2 + D_3), \quad M_{25} = \frac{1}{4}(D_3 - D_2)$$

with D_i defined in Eqs. (4.23) and ellipsis denoting the matrix elements we do not need to calculate, as they are at most order-1 in N_c counting. From A.10 we see that if we start in the color-singlet state $|P_1\rangle$ for the top (bottom) gluon pair, a single interaction can either leave the two gluons in the color-singlet state, or can flip them into a color-octet state $|P_5\rangle$. The latter transition comes in with an order- $1/N_c$ suppression factor. In order to evaluate A.1 we have to start and finish with a color-singlet state: to order- $1/N_c^2$ we may have at most two such transitions: $|P_1\rangle \rightarrow |P_5\rangle$ and the inverse, $|P_5\rangle \rightarrow |P_1\rangle$. Once the system is in the color-octet $|P_5\rangle$ state, it can continue its random walk through color space: however, if we want to keep the calculation at the order- $1/N_c^2$, the interactions between the two transitions should be leading-order in N_c . This is why only the leading- N_c -order matrix elements M_{22} , $M_{25} = M_{52}$, and M_{55} contribute in the 6×6 matrix M_{ij} with $i, j = 2, \dots, 7$: we do not need to calculate the $1/N_c$ -suppressed elements in A.10 or the elements denoted by ellipsis which can not contribute.

Exponentiating the matrix M from [A.10](#), picking up the “11” element of the obtained matrix and expanding the result to order- $1/N_c^2$ yields

$$\begin{aligned} \frac{1}{(N_c^2 - 1)^2} \langle Tr[U_{\mathbf{x}_1} U_{\mathbf{x}_2}^\dagger] Tr[U_{\mathbf{x}_3} U_{\mathbf{x}_4}^\dagger] \rangle &= e^{D_1} + \frac{(D_3 - D_2)^2}{N_c^2} \left[\frac{e^{D_1}}{D_1 - D_2} - \frac{2e^{D_1}}{(D_1 - D_2)^2} \right. \\ &\quad \left. + \frac{e^{D_1}}{D_1 - D_3} - \frac{2e^{D_1}}{(D_1 - D_3)^2} + \frac{2e^{\frac{1}{2}(D_1+D_2)}}{(D_1 - D_2)^2} + \frac{2e^{\frac{1}{2}(D_1+D_3)}}{(D_1 - D_3)^2} \right] + \mathcal{O}\left(\frac{1}{N_c^4}\right). \end{aligned} \quad (\text{A.11})$$

Finally, noting that (see [4.20](#))

$$\frac{1}{(N_c^2 - 1)^2} \langle Tr[U_{\mathbf{x}_1} U_{\mathbf{x}_2}^\dagger] \rangle \langle Tr[U_{\mathbf{x}_3} U_{\mathbf{x}_4}^\dagger] \rangle = e^{D_1} \quad (\text{A.12})$$

and using [4.21](#) we obtain [4.22](#).